Dissertation
submitted to the
Combined Faculties of the Natural Sciences and for Mathematics
of the Ruperto-Carola University of Heidelberg, Germany
for the degree of
Doctor of Natural Sciences

Put forward by
Dipl.-Phys. Simone Andrea Götz
Born in Sindelfingen
Oral examination: May 9th, 2012

A high density target of ultracold atoms and momentum resolved measurements of ion-atom collisions

Referees: **Prof. Dr. Matthias Weidemüller**
Priv.-Doz. Dr. Alexander Dorn

The author has contributed to the following publications:

- T. Mullins, W. Salzmann, S. Götz, M. Albert, J. Eng, R. Wester, M. Weidemüller, F. Weise, A .Merli, S. M. Weber, F. Sauer, L. Wöste, and A. Lindinger
  Photoassociation and coherent transient dynamics in the interaction of ultracold rubidium atoms with shaped femtosecond pulses. I. Experiment
  Phys. Rev. A **80**, 063416 (2009)

- A. Merli, F. Eimer, F. Weise, A. Lindinger, W. Salzmann, T. Mullins, S. Götz, R. Wester, M. Weidemüller, R. Aganoglu, and C. P. Koch
  Photoassociation and coherent transient dynamics in the interaction of ultracold rubidium atoms with shaped femtosecond pulses. II. Theory
  Phys. Rev. A **80**, 063417 (2009)

- F. Eimer, F. Weise, A. Merli, S. Birkner, F. Sauer, L. Wöste, A. Lindinger, R. Aganoglu, C.P. Koch, W. Salzmann, T. Mullins, S. Götz, R. Wester, and M. Weidemüller
  Spectrally resolved coherent transient signal for ultracold rubidium molecules
  Eur. J. Phys. D **54**, 711-714 (2009)

- M. Albert, T. Mullins, S. Götz, W. Salzmann, R. Wester, and M. Weidemüller
  The interaction of a spectrally cut laser-pulse with a two-level atom
  J. Mod. Opt. **55**, 3359 (2008)

- M. Fattori, T. Koch, S. Goetz, A. Griesmaier, S. Hensler, J. Stuhler, and T. Pfau
  Demagnetization cooling of a gas
  Nature Physics **2**, 765 (2006)

Abstract. In this thesis an ultracold high density target with high loading flux in combination with a recoil ion momentum spectrometer (RIMS) is presented. Trapped rubidium atoms serve as a high density target (up to 10^{11} atoms/cm^3) at a temperature of only 200 μK. The target is loaded from a two-dimensional magneto-optical trap (2D MOT), which delivers an atom beam with a brilliance of 8×10^{12} atoms/(s $\cdot$ rad) and a longitudinal momentum spread of 0.25 a.u.. The great advantage of this source is that the cold atom beam can be used as a target itself. The experimental setup, including the RIMS and the targets, are characterized using one-color two-photon ionization experiments. After the successful commissioning presented in this thesis the experiment is ready to be connected to the HITRAP beamline at the GSI Helmholtzzentrum für Schwerionenforschung, where multiple charge transfer between ultracold atoms and highly charged ions up to bare uranium can be investigated. In a different experimental setup, in collaboration with the KVI in Groningen, the Netherlands, first experiments on the energy dependence of double charge transfer in alkali-ion collisions are preformed. Using RIMS, two distinct double capture mechanisms, sequential transfer and correlated transfer, are identified and the respective differential cross sections are determined. The effective interaction time of the collision is varied by changing the projectile's velocity. At short interaction times the sequential transfer is dominant, while at longer interaction times the correlated transfer becomes more important.

Zusammenfassung. Diese Arbeit präsentiert ein ultrakaltes Target hoher Dichte mit schnellen Ladezeiten kombiniert mit einem Ionenrückstoßspektrometer (RIMS). Magneto-optisch gefangene Rubidiumatome mit einer Dichte von 10^{11} Atomen/cm^3 dienen als Target und werden auf 200 μK abgekühlt. Das Target wird aus einer zweidimensionalen magneto-optischen Falle (2D MOT) geladen, welche einen Atomstrahl hoher Brillianz (8×10^{12} Atome/(s $\cdot$ rad)) und geringer longitudinaler Impulsverbreiterung von 0.25 a.u. liefert. Insbesondere eignet sich der Atomstrahl mit diesen Eigenschaften selbst als Target. Die Targets und das Rückstoßionenspektrometer werden mittels gepulster Photoionisationsexperimente charakterisiert. Nach der erfolgreichen Kommissionierung steht das Experiment nun bereit, um an der HITRAP Strahllinie am GSI Helmholtzzentrum für Schwerionenforschung integriert zu werden, um Mehrfachladungstransfer zwischen ultrakalten Atomen und hochgeladenen Ionen bis hin zu nacktem Uran zu untersuchen. In einem anderen experimentellen Aufbau, in Kollaboration mit dem KVI in Groningen, Niederlande, wurden erste Ergebnisse zur Energieabhängigkeit von Doppelladungstransfer in Stößen zwischen ultrakalten Alkaliatomen und hochgeladenen Ionen erzielt. Mittels Rückstoßionenspektroskopie werden zwei verschiedene Doppelladungstransfermechanismen, sequentieller Transfer und korrelierter Transfer, identifiziert und deren differenziellen Wirkungsquerschnitte gemessen. Die effektive Wechselwirkungszeit des Stoßes wird durch Variieren der Projektilenergie geändert. Bei kurzen Wechselwirkungszeiten dominiert der sequentielle Transfer, während bei langen Wechselwirkungszeiten der korrelierte Transfer zunimmt.

Contents

Chapter 1

Introduction

The dynamics in many-body atomic systems is not only a fundamental problem in itself but is of high importance for the understanding of our everyday world being at the basis of chemical reactions and biological systems. One example of a many-body quantum dynamical problem is the breakup of a system of charged particles. The easiest scenario for such a system involving three charged particles is the electron impact ionization of hydrogen. A theoretical description of this process giving complete details about the energy and angular distributions of the two outgoing electrons has, however, been only achieved in 1999 [1]. In contrast to bound systems, the major challenge in describing collision problems theoretically is that the wave functions are non-stationary and not localized but extended over all space including continuum states.

A more complex situation is given when collisions with targets having more than one electron are investigated where correlations in the electronic structure of the target atom are revealed. The correlations hamper the theoretical treatment since the wave functions are not separable any more.

Experimentally, a particularly well suited system for these investigations is the interaction between highly charged ions and neutral atoms. Using highly charged ions as a projectile has the advantage that their electronic structure does not need to be considered since their electrons are bound very tightly. Therefore their probability of undergoing transitions can be neglected in comparison to the outer electrons of the target atoms. Depending on the collision energy, different processes can take place in these collisions. These processes are impact ionization, excitation and charge transfer. Impact ionization is dominant for velocities of the projectile higher than the orbital velocity of the target's active electrons. For projectile velocities close to the orbital velocity of the active electron, excitation occurs. For projectile velocities lower than the velocity of the active electrons, impact ionization can be neglected and electron transfer, also called charge transfer or electron capture, is the dominant process.

In charge transfer the collision of a q-fold charged ion A^{q+} with a target atom B

can result in the projectile ion capturing r of the atom's electrons:

$$A^{q+} + (n_0, l_0, m_0) \rightarrow A^{(q-r)+}B(n', l', m') + B^{(r)+}, \tag{1.1}$$

where (n_0, l_0, m_0) and (n', l', m') are the respective sets of quantum numbers before and after the collision, with the principle quantum number n, the angular momentum l and the magnetic quantum number m. Electrons are captured into highly excited projectile states (n', l', m') and decay subsequently into lower energy states by emission of electromagnetic radiation in the UV- or X-ray range or by Auger processes.

These many-particle reactions are characterized by fully differential cross sections, i.e. cross sections differential in all observables of the final state. A remarkable imaging technique to investigate fragmentation processes in atomic collisions with high resolution and 4π detection angle efficiency is the technique of recoil ion momentum spectroscopy (RIMS) [2, 3, 4, 5, 6], which has been developed in the past 20 years. The technique of RIMS relies on measuring the vector momentum of the particles involved in the collision, originating from a well localized reaction zone. Electromagnetic fields guide the fragments onto position and time sensitive detectors. From the charge state of the ion the multiplicity of the process can be deduced, whereas from the momentum components of the recoil ion the dynamics of the collision is known.

Basic requirement for this method is a well-defined initial state of the target which was first achieved by cooling the target atoms or molecules in a supersonic gas jet, where temperatures in the sub-K regime can be reached. The field was therefore called COLTRIMS (COLd Target Recoil Ion Momentum Spectroscopy). However, due to experimental constraints, the available species are restricted to light noble gases, i.e. helium, neon and argon.

Another way to provide a cold and localized target is trapping of neutral atoms in magneto-optical traps (MOT) [7, 8, 9, 10], which is nowadays a standard tool in atomic physics. By combining near resonant laser light with a magnetic trapping field, atoms can be trapped in a well localized volume and cooled down to the μK regime, making it a perfect candidate for a RIMS target. In analogy to COLTRIMS, this field has been named MOTRIMS (Magneto-Optical Trap Recoil Ion Momentum Spectroscopy)[11]. Since many different elements can be laser cooled, the available species used for targets in RIMS are not restricted to light noble gases any more. For investigation of ionization processes the technique has been extended to the coincidence detection of the ejected electrons and is called reaction microscope [12, 13, 14, 15].

Providing a laser cooled target thus allows the investigation of projectiles with target atoms where the participating electrons have different principle quantum

numbers. Alkalis are of particular interest for investigation of multiple charge transfer between neutral alkali atoms and highly charged ions. Their two outer electrons have different principle quantum numbers allowing to gain insight in the electronic structure of many-electron atoms. This is in contrast to noble gas targets where the initial electrons have nearly the same electronic configuration.

In first experiments, in collaboration with the group of R. Hoekstra at the sodium MOTRIMS setup at the Kernfysisch Versneller Instituut (KVI) in Groningen, the Netherlands, performed at an existing setup, we investigated the energy dependence in double charge transfer in collisions between highly charged ions and ultracold alkali atoms, namely in the system O^{6+} + Na(3s). Double electron transfer leads to the creation of doubly excited $O^{4+}(nln'l')$ projectile states:

$$O^{6+} + Na([Ne]s^1) \rightarrow O^{4+}(nln'l') + Na^{2+}([Ne^+]). \tag{1.2}$$

The results will be presented in chapter 3.

A new high density target for investigation of ion-atom collisions at the HITRAP beamline at the GSI Helmholtzzentrum für Schwerionenforschung has been developed in this thesis. This novel source of heavy highly charged ions at low temperatures, where ions up to bare uranium will be made available, is currently being built up. Investigation of charge transfer in collision between these heavy ions and neutral atoms are planned. Classical over the barrier model calculations show that the cross sections for multiple electron capture are on the order of $10^{-15}\,\mathrm{cm}^2$, being two orders of magnitude smaller than for single charge transfer [16, 17]. In order to optimize the signal to noise ratio in these measurements, a target with high density, high loading flux leading to high repetition rates and low background is thus indispensable. Therefore, a high density magneto-optical trap in dark SPOT (SPontaneous Optical Trap) configuration allowing for densities up to $10^{11}\ \mathrm{cm}^{-3}$ has been developed in this thesis [18]. It is positioned at the center of a recoil ion momentum spectrometer and can serve as a target for photons as well as highly charged ions due to a compact design. In order to ensure a high loading flux while keeping a very low pressure and thus no background ions in the interaction volume, a two-dimensional magneto-optical trap (2D MOT) has been implemented in a double-chamber system [19, 20]. The atoms are precooled in two dimensions in a separate chamber, leading to a well collimated cold atom beam in the third dimension. At the same time the atom beam generated by the 2D MOT might be used as a target itself with reduced density in comparison to targets obtained in supersonic gas jets.

This thesis consists of two parts: On one hand a first generation experiment is upgraded, meeting all the requirements needed for the study of multiple charge

transfer, and on the other hand the energy dependence in double charge transfer in collisions between highly charged ions and ultracold sodium atoms is investigated.

An introduction to the working principle of MOTRIMS will be given in chapter 2. The results on double charge transfer in O^{6+} + Na(3s) are presented in chapter 3. Since the charge exchange experiments will be done at GSI, the whole setup is modular, compact and transportable. This novel design of the upgraded setup will be described in detail in chapter 4. The new setup is characterized by non-resonant two-photon ionization of the rubidium atoms which is presented in chapter 5.

Chapter 2

MOTRIMS

Recoil ion momentum spectroscopy (RIMS) is a momentum space imaging technique for investigation of the dynamics of any collisional system where one of the reactants is ionized. The gimmick of this technique is that the ionizing partner has negligible initial momentum such that detection of its recoil momentum components, which are usually very small, gives full information on the three dimensional momentum vector. It has been the working horse in atomic physics for the past 20 years, allowing the investigation of a broad range of projectile beams such as photon-, ion- and electron- beams with any neutral sample [3, 4, 5, 6]. A very detailed description on the recent developments, results and details of the working principle in RIMS can be found in [6]. Furthermore, the emergence of the field of laser cooled atoms has increased the available species which can be used as targets and the combination of a magneto-optical trap (MOT) with recoil ion momentum spectrometer is called MOTRIMS [7, 8, 9, 10]. An overview of this field can be found in [11].

In the following (subsection 2.1.1) a short introduction into the field of RIMS is given, followed by a description of the kinematics (subsection 2.1.2) and its modes of operation (subsection 2.1.5). A small discussion on the limitations of this technique follows in subsection 2.1.6. As will be discussed, a negligible initial momentum spread of the target atoms is the key element for RIMS. The targets can be either cooled using supersonic gas expansion which is the basis of COLTRIMS [3, 4, 6, 5, 12, 14, 15], or using laser cooling, leading to temperatures in the μK regime [11]. Different state of the art techniques of realizing magneto-optical traps are presented in subsection 2.2.1. The different regimes in a MOT are summarized in subsection 2.2.2.

2.1 Recoil ion momentum spectroscopy

2.1.1 Introduction to RIMS

Recoil ion momentum spectroscopy is used to get insights into the dynamics of many-body quantum systems which occur during fragmentation induced by collisions of ions, electrons or photons with atoms or molecules. Atomic and molecular many-body systems are characterized by the fully-differential cross section (FDCS), i.e. the cross section differential of all observables in the final state. This typically corresponds to vector momenta, spin and internal excitation of all reaction products. The goal of RIMS is to provide kinematically complete studies of momenta, which then contain information on the angles and energies of the collision of all involved particles during the collision, whereas spin is completely neglected.

Traditionally, charge exchange in atomic collisions has been investigated using traditional electron spectroscopy, i.e. translational energy spectroscopy (TES), Auger electron spectroscopy (AES) and Photon emission spectroscopy (PES). These methods rely on determining the inelasticity of the process, the so-called Q-value, which is the difference in binding energy of all electrons before and after the collision. In TES, the Q-value is obtained by measuring the kinetic energy gain or loss of the projectile which is, in the case of small energy transfers and small scattering angels, directly equal to the negative Q-value, revealing the final state distribution. The main limits of this technique are that the final resolution depends on the initial kinetic energy spread of the projectiles and that the finite angular resolution limits the energy resolution. TES has been used to determine scattering angle-dependent cross sections and has been applied to atomic as well as molecular gas targets. For more details refer to the review [21, 22] and references therein. Photon-emission spectroscopy relies on measuring the spectrum of photon emission which follows the collision, from which the electronic final state distribution directly after the collision can be determined [23, 24]. Since the wavelength of photons can be measured with very high precision, this technique allows for very high energy resolution. However, the solid angle is rather small. Furthermore, the detection of photons implies that this technique is limited to final electronic states which decay via photon emission, i.e. population of ground state or long-lived Rydberg states. Also configurations which decay via electron emission cannot be detected and no information on the scattering angle is obtained. AES also relies on the recoil ion to further decay by the Auger process [25].

RIMS, however, relies on measuring the recoil's momentum vector and is such not limited in resolution by the initial projectile beam or the population of certain electronic states. It is based on the coincidence detection of reaction products resulting

from an atomic collision using large-area position sensitive detectors together with time of flight measurements. From this coincidence detection the charge state as well as the three-dimensional momentum vector of the recoil ions can be determined with a 4π solid angle efficiency. First generation experiments used extended targets at room temperature, where the thermal motion of the atoms limited the resolution (ΔE $\approx$ 40 meV) [26, 27]. The detection of the Q-value was implemented in [2, 28]. In the following ten years the resolution was improved to resolutions as good as ΔE $\approx \pm$ 30μeV using a precooled gas for supersonic expansion which was called COLTRIMS [29, 3]. Further including an electrostatic field and focusing the recoil ions onto the position sensitive detector further improved the resolution down to $\Delta E \approx 1.2\mu$eV for a He target [30, 14, 4]. In 1993, R. Moshammer and J. Ullrich have further developed a so-called reaction microscope, where also the ejected electrons in ionization experiments are detected in coincidence with the recoil ion and the projectile [12]. It is of great interest in combination with the rapidly growing field of ultrashort high power lasers, which go down to the attosecond regime, and lately even free-electron lasers. Multi-photon ionization experiments reveal information on the initial electron wavefunctions and correlations [31, 32, 33].

The target's initial temperature influences the final resolution and is reduced in COLTRIMS using supersonic gas expansion. However with this technique, targets are limited to noble gases of low mass (T $\propto \sqrt{m}$, m being the mass of the target atom) and molecular beams. Laser cooling and trapping developed in the past 20 years provide very localized and cold targets down to the μK regime, extending the available target elements not only to alkalis[1] [10]. Apart from the thus obtained increased momentum resolution ($\delta p = 0.03$ a.u. have been reported in [34]), now also targets with nonequivalent initial electron configuration become accessible.

Up to date there are several MOTRIMS setups and two reaction microscopes available: two lithium targets combined with a reaction microscope at the MPI-K in Heidelberg [35], one sodium target at the KVI in Groningen [36, 37], one cesium target in Campinas, Brasil [38], one lithium target in Illinois [39, 40] and three rubidium targets; one in the group of B. DePaola at the Kansas state university [41], one in the group of X. Flechard [34] and one in the group of M. Weidemüller at the university of Heidelberg, which will be described in this work. The reaction microscope in the group of D. Fischer has successfully been implemented in the TSR storage ring where charge exchange is studied. The one in the group of A. Dorn is used as a target for coherent radiation in the VUV from the free electron laser FLASH in Hamburg, where two-electron threshold dynamics in double photoionization has been studied [33]. The rubidium targets are used to study electron transfer

[1] Alkalis are in particular suited for laser cooling due to the presence of a closed cooling cycle.

in ion-atom collisions [34, 42].

2.1.2 Kinematics of recoil ion production

The kinematics of a collision between two particles is fully determined by the momentum and energy conservation laws. For two colliding particles, the momentum conservation can be written as:

$$\mathbf{P}_P^i + \mathbf{P}_R^i = \mathbf{P}_P^f + \mathbf{P}_R^f + \sum_j^N \mathbf{P}_{el,j}^f + \sum_l^{N'} \mathbf{P}_{\gamma,l}^f, \tag{2.1}$$

where the superscript i indicates before and f after the collision. The subscripts P stands for the projectile and R for the recoil ion originating from the target atom, el and γ for the additional electrons and photons emitted into the continuum during the collision. The important quantity of the reaction is the momentum transfer given by:

$$\mathbf{q} = \mathbf{P}_P^i - \mathbf{P}_P^f = (q_{\text{long}}, q_{\text{trans}}), \tag{2.2}$$

which can be decomposed in the longitudinal and the transversal components, where the incident projectile beam defines the longitudinal direction (see figures 2.1 and 2.2). Due to the symmetry, y and z-directions contain the same information and the momentum vector can be separated in a longitudinal and a transverse component.

$$\mathbf{P} = \mathbf{P}_{\text{long}} + \mathbf{P}_{\text{trans}} \tag{2.3}$$

Considering the very low initial momentum spread of the target atoms of only 0.017 a.u., $\mathbf{P}_R^i$ can be neglected in the laboratory frame . It follows

$$\mathbf{P}_{\text{P,long}}^i = \mathbf{P}_{\text{P,long}}^f + \mathbf{P}_{\text{R,long}}^f + \sum_j^N \mathbf{P}_{e,long}^f \tag{2.4}$$

$$0 = \mathbf{P}_{P,trans}^f + \mathbf{P}_{R,trans}^f + \sum_j^N \mathbf{P}_{e,trans}^f. \tag{2.5}$$

Thus the momentum transfer can be rewritten:

$$\mathbf{q} = (q_{\text{long}}, q_{\text{trans}}) = (\delta E_P / v_P, q_{\text{trans}}), \tag{2.6}$$

where v_P is the projectile velocity in case of an ion-atom collision. Introducing the very important quantity called the inelasticity of the process, the Q-value which is

the change in internal energies of the projectile and the target, defined as

$$Q = E^f_{\text{bind}} - E^i_{\text{bind}}, \tag{2.7}$$

the energy conservation for the same colliding system can be written as:

$$E^i_P + E^i_R = E^f_P + E^f_R + Q + \sum_j E^N_{el,j}. \tag{2.8}$$

E^f_{bind} denotes the final binding energy of all electrons directly after the collision, before any deexcitation might occur. The Q-value defines whether the collision is endo- or exothermic. Depending on the projectile particle, several assumptions can be made, leading to easy expressions for the measured quantities. First, the details of the kinematics arising from pure electron capture in ion-atom collisions is discussed, followed by a discussion of the kinematics in photon-atom collisions. We follow the convention using atomic units throughout the whole chapter, which is based on

$$\hbar = m_e = e = 4\pi\epsilon_0 = 1, \tag{2.9}$$

$\hbar$ being Plancks constant devided by 2π, m_e and e are the electron mass and the electron charge and ϵ_0 is the permitting of free space.

2.1.3 Photoionization

In case of ionization of the target through photoabsorption, depicted in figure 2.1,

$$n \cdot h\nu + B \rightarrow B^+ + e^-, \tag{2.10}$$

with n photons of frequency ν, each of them carrying energy $h\nu$, the energy and momentum conservation laws can be rewritten (see 2.1 and 2.8)

$$\mathbf{P}_\gamma + \mathbf{P}^i_R = \mathbf{P}^f_R + \sum_j^N \mathbf{P}^f_{el,j}, \tag{2.11}$$

$$E_\gamma + E^i_{\text{bind}} = E_R + E^f_{\text{bind}} + \sum_j^N E_{el,j}, \tag{2.12}$$

where $E_{\text{bind}} < 0$ is the sum of all binding energies of the electrons before and after the collision and $E_\gamma = P_\gamma c$ is the photon energy. Again, the initial momentum of the target can be neglected, and q_{long} in equation 2.6 needs to be replaced with the

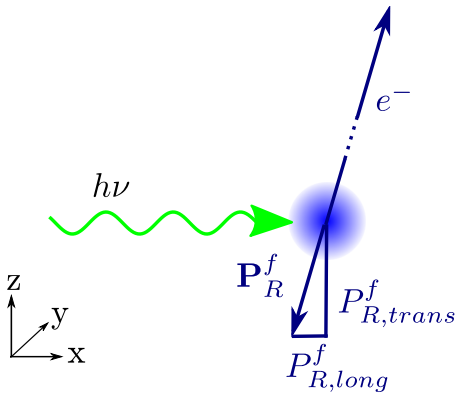

Figure 2.1: Kinematics in photoionization. The incoming photon with energy $h\nu$ ionizes the target atom. The momentum of the photon is small and is neglected after the collision. Due to momentum and energy conservation the ejected electron e^- and the recoil ion have opposite directions. The energy transferred to the recoil ion is m_e/m_R times smaller than the energy transferred to the ejected electron. The momentum of the recoil ion (P_R^f) can be separated into a longitudinal $P_{R,\text{long}}^f$ and a transverse $P_{R,\text{trans}}^f$ component.

photon momentum. The momentum vectors can therefore be written as:

$$\mathbf{P}_\gamma = (E_\gamma/c, 0, 0), \quad \mathbf{P}_R^i = (0, 0, 0). \tag{2.13}$$

From the momentum conservation we see that the momentum vectors from the ejected electron and the recoil ion compensate each other. Taking into account that the photon momentum is small compared to the particle momenta in the final state ($E_\gamma/c \ll P_R^f$), one can write:

$$|\mathbf{P}_R^f|^2 = |\mathbf{P}_e^f|^2 = 2\frac{m_e m_R}{m_e + m_R}\,(E_\gamma + E_{\text{bind}}^i - E_{\text{bind}}^f) \tag{2.14}$$

and one obtains for the energies of the fragments after collision:

$$E_R = 2\frac{m_e}{m_e + m_R}\,(E_\gamma + E_{\text{bind}}^i - E_{\text{bind}}^f) \tag{2.15}$$

$$E_e = 2\frac{m_R}{m_e + m_R}\,(E_\gamma + E_{\text{bind}}^i - E_{\text{bind}}^f). \tag{2.16}$$

Thus the energy transfer to the recoil ion is m_e/m_R times smaller than to the ejected electron.

2.1.4 Pure electron capture in ion-atom collisions

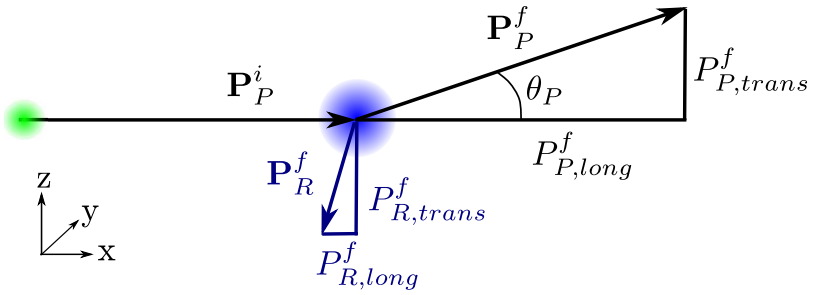

Figure 2.2: Kinematics of pure electron capture in ion-atom collision. The projectile beam propagates along the x-axis with initial momentum $\mathbf{P}_P^i$, the target is initially at rest. After the collision and electron capture from the target atoms, the projectile now has a momentum of $\mathbf{P}_P^f$ with a scattering angle θ_P with respect to the initial propagation axis x. The momentum transferred to the recoil ion can be decomposed in a transverse $P_{\mathrm{R,trans}}$ and a longitudinal $P_{\mathrm{R,long}}$ component, which are completely decoupled from each other (see text).

One application of RIMS is the investigation of the dynamics during charge transfer in ion-atom collision. This process competes with ion impact ionization. For projectile velocities smaller than the velocity of the electrons orbiting the target atom, the process of impact ionization is negligible.

In this section the case of pure electron transfer will be discussed. Therefore the last term in equation 2.8 can be neglected. Typical momenta of the projectile beams are on the order of a 10^3 a.u., whereas transferred momenta are on the order of a few a.u. [2]. We can assume that the change of the target's energy compared to the initial and final projectiles energies can be neglected:

$$E_R^f \ll E_P^i = \frac{(P_P^i)^2}{2m_P^i} \approx E_P^f = \frac{(P_P^f)^2}{2m_p^f}, \tag{2.17}$$

where m_P^i and m_P^f denote the initial and final projectile mass. The change in mass and total energy of the projectile before and after the collision is only given by the number of transferred electrons n_C and is thus very small such that $\delta m_P/m_P^i \ll 1$ and $\delta E_P/E_P^i \ll 1$.

For small momentum transfer, resulting in small scattering angles, we can further

[2] In the experiments reported on in chapter 3, the transferred momenta are three orders of magnitudes smaller than the momentum of the initial ion beam.

approximate

$$P^f_{\mathrm{P,trans}}/P^f_{\mathrm{P,long}} \approx \theta_P \;\text{ and }\; P^f_{\mathrm{P,long}} = \sqrt{2m^f_P E^f_P}. \tag{2.18}$$

With these assumptions one finds the important expression for the longitudinal momentum of the recoil ion (using 2.5):

$$-\delta P_{\mathrm{P,long}} = -P_{\mathrm{R,long}} = \frac{Q}{v_P} - \frac{1}{2}\cdot n_C \cdot v_P. \tag{2.19}$$

For derivation for the transverse components of the recoil-ion momentum, one starts from the momentum conservation law (cf. equation 2.1) and makes use of the fact that the recoil ion has no initial momentum component along the transverse direction, $\mathbf{P}^i_R = 0$. Thus $\mathbf{P}^f_{R,trans} = -\mathbf{P}^f_{P,trans}$. Further taking into account that the projectile's polar scattering angle θ_P for this reaction is very small, typically on the order of $mrad$, it follows (see figure 2.2):

$$\mathbf{P}^f_{R,trans} = |\mathbf{P}^f_{R,trans}| = -P^f_{\mathrm{P,trans}} \approx -m_P \cdot v_P \cdot \theta_P. \tag{2.20}$$

In case of a pure electron capture the longitudinal and transverse momentum components of the recoil ion are thus completely decoupled. From the longitudinal momentum component, one can deduce the inelasticity of the reaction and the final bound states, whereas from the transverse momentum component, the projectile scattering angle and for a known scattering potential, the impact parameter can be deduced.

2.1.5 Reconstruction of the initial recoil ion momentum

Principle

In RIMS, information on the three dimensional momentum distribution is extracted from a two-dimensional detector image from the recoil ion's time of flight [43]. A spectrometer consists of two different electric field regions (see figure 2.3): A weak electric field, the so-called extraction field, extracts the ions from the collision region and accelerates them towards a position-sensitive detector. Before the ions hit the detector, they cross a field-free drift region where they expand freely. Two different extraction geometries are possible: longitudinal extraction, of the recoil ion, where the extraction field is parallel to the projectile beam and the longitudinal momentum component of the recoil ion is deduced from the time of flight. This geometry requires the use of special ion detectors, including a hole in its center, such that the detection of the recoil ions is not masked by the projectiles. Another geometry, which is also used in the current work, is the transverse extraction geometry, where

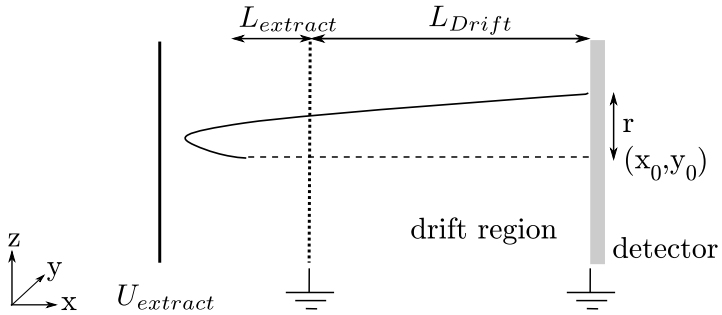

Figure 2.3: Principle of a recoil ion momentum spectrometer. The recoil ion is extracted from the collision region by applying a weak extraction field. For transverse extraction, the projectile beam enters the spectrometer transverse to the extraction field, whereas for longitudinal extraction, the projectile beam is parallel to the extraction field.

the recoil ions are extracted transverse to the projectile beam. Here, the longitudinal momentum component, which gives information on the inelasticity of the collision Q, is proportional to the position $X = x - x_0$, [3] where x_0 is the center of the detector and x is the position where the recoil ion hits the detector. The transverse momentum component in the y-direction is proportional to $Y = y - y_0$ and the transverse momentum component in z-direction is proportional to the time of flight.

Since the momentum in X-direction is perpendicular to the extraction field, and thus no force is acting on this component:

$$p_{\text{long}} = m\frac{X}{t}, \tag{2.21}$$

with m being the mass of the recoil ion and t the time of flight. Due to the focusing characteristics of the spectrometer the spread in time is much smaller than the time of flight. Thus, using eq. 2.19, it follows:

$$p_{\text{long}} \approx a_{\parallel} X = -\frac{Q}{v_p} - n_C \frac{v_p}{2}, \tag{2.22}$$

where $a_{\parallel}$ converts the longitudinal momentum to the X-position on the detector. Due to symmetry arguments, the same holds for the Y-position: $p_{\text{trans,y}} \approx a_{\perp} Y$. Note that the parameter $a_{\parallel} = a_{\perp}$ due to the symmetry of the spectrometer.

The electric field in z-direction leads to an acceleration of the recoil ion in this

[3] For the laser experiments (see chapter 5), only the transverse momenta are of interest.

direction ($a = qE_z/m$). Thus the situation is more complicated:

$$t = \frac{-v_{\mathrm{trans,z}} + \sqrt{v_{\mathrm{trans,z}}^2 + 2L_{\mathrm{extrac}}a}}{a} + \frac{L_d}{\sqrt{v_{\mathrm{trans,z}}^2 + 2L_{\mathrm{extrac}}a}}. \tag{2.23}$$

$v_{\mathrm{trans,z}} = p_{\mathrm{trans,z}}/m$, L_d is the length of the drift region and L_{extrac} is the distance from the collision region to the end of the spectrometer head. Solving this problem is not evident since E_z is not constant in the spectrometer head. For an inhomogenuos field an effective field $E_{\mathrm{z,eff}}$ has to be assumed. Considering again that the spread in time of flight is much smaller than the total time of flight $t_0 = t(v_{\mathrm{trans,z}}) = 0$ for ions without initial momentum in z-direction, equation 2.23 can be expanded around t and reads

$$\Delta t \approx -\frac{v_{\mathrm{trans,z}}}{a} \Rightarrow p_{\mathrm{trans,z}} \approx -b\Delta t, \tag{2.24}$$

where b is a constant only depending on the extraction voltage and geometry ($b \approx ma$ for a homogeneous field).

Example

To give an idea on how the momentum is reconstructed in the experiment at the KVI, Groningen, in which we participated, an example is given. We use single charge transfer in the system O^{6+} + Na(5s). The dataset has been taken by I. Blank at the MOTRIMS setup at KVI, Groningen, the Netherlands, and will be further used in chapter 3. Figure 2.4 shows the two-dimensional detector image for charge transfer with transverse extraction geometry. The recoil ions are detected on the detector after passing a field free drift region. For every recoil ion the position on the detector as well as its time of flight is measured. As explained above we can deduce the momentum components from this information. Since the projectile beam is parallel to the x-axis, the X-component of the recoil ion is proportional to the longitudinal momentum and thus the Q-value. From the detector image we can see three different channels which correspond to the electrons being captured into different shells in the projectile. Since the Q-values of these channels are well known this data set can be used for calibration of the detector's x-axis. The other two momentum components, namely the Y- and TOF component, are proportional to the transverse momentum of the recoil ion. Assuming that the spectrometer has cylindrical symmetry the calibration factor in x-direction is the same as in y-direction. Due to the cylindrical symmetry of the collision the transverse momentum in time of flight direction is the same as the transverse momentum distribution in y-direction. In an ad-hoc assumption the calibration in time of flight direction is

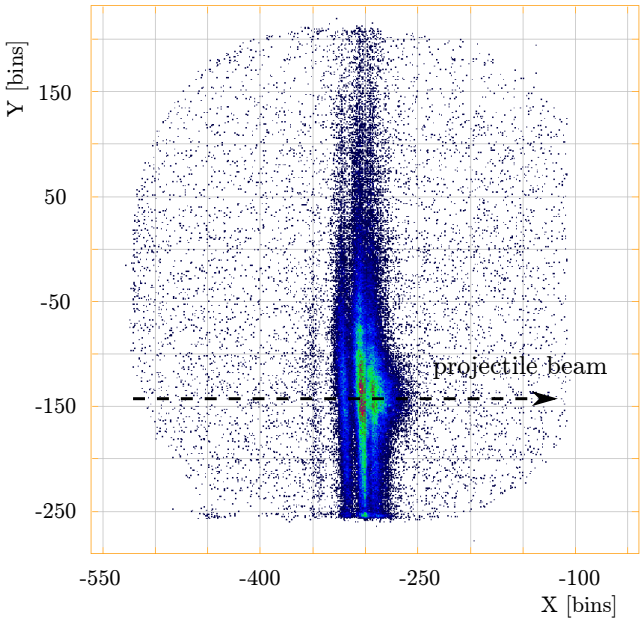

Figure 2.4: Example for calibration of a recoil ion momentum spectrometer. The data shows the detector image taken for single charge transfer in the system O^{6+} + Na(5s), taken by I. Blank at the MOTRIMS setup at KVI, Groningen. Capture into final states with different n result in lines along the x-axis which is parallel to the projectile beam. From the projection of the spectrum onto the x-axis, the longitudinal momentum is deduced since the energies of the channels are well known.

chosen such that the transverse momentum distribution is circular.

2.1.6 Limitations in RIMS

In order to get a feeling for RIMS, some limitations on the resolution of the system will be identified.

Limitations on the inelasticity of the collision

From equation 2.19 the following expression can be deduced for the Q-value:

$$Q = -v_P P^f_{\mathrm{R,long}} - \frac{1}{2} n_C v_P^2, \tag{2.25}$$

such that the resolution of the inelasticity of the collision is given by:

$$\Delta Q = \sqrt{\left(\left(P^f_{\mathrm{R,long}} + n_C v_P\right)\Delta v_P\right)^2 + \left(v_P \Delta P^f_{\mathrm{R,long}}\right)^2}. \tag{2.26}$$

Rewriting leads to [34]

$$\Delta Q = \sqrt{\left(\left(\frac{P^f_{\mathrm{R,long}}}{m_P v_P} + \frac{n_C}{m_P}\right)\Delta E^i_P\right)^2 + \left(v_P \Delta P^f_{\mathrm{R,long}}\right)^2}. \tag{2.27}$$

Since $m_P v_P^2 \ll Q$, the following approximation is valid $Q \approx -v_P P^f_{\mathrm{R,long}}$ such that:

$$\Delta Q = \sqrt{\left(\left(\frac{-Q}{2E^i_P} + \frac{n_C}{m_P}\right)\Delta E^i_P\right)^2 + \left(Q\frac{\Delta P^f_{\mathrm{R,long}}}{P^f_{\mathrm{R,long}}}\right)^2}. \tag{2.28}$$

In the experiments considered in this work $n_C/m_P < 10^{-4}$ and $Q/(2E^i_P) < 10^{-3}$, whereas $\Delta P^f_{\mathrm{R,long}}/P^f_{\mathrm{R,long}} < 10^{-2}$. Hence, the resolution on the Q-value is only limited by the resolution on the longitudinal momentum component of the recoil ion:

$$\Delta Q = \left| Q\frac{\Delta P^f_{\mathrm{R,long}}}{P^f_{\mathrm{R,long}}} \right|. \tag{2.29}$$

Limitations on the determination of the scattering angle

Using equation 2.20, the projectile scattering angel can be rewritten as:

$$\theta_P = -\frac{P^f_{R,trans}}{m_P v_P}. \tag{2.30}$$

The resolution of the projectile scattering angle is thus given by:

$$\delta\theta = \sqrt{\left|\frac{\delta\theta_p}{P^f_{R,trans}}\right|^2 (\Delta P^f_{R,trans})^2 + \left|\frac{\delta\theta_p}{v_P}\right|^2 (\Delta v_P)^2} \tag{2.31}$$

and, using $E_P^i = 1/2 m_P v_P^2$, can be rewritten as:

$$\Delta\theta_P = |\theta_P| \sqrt{\left(\frac{\Delta P_{R,trans}^f}{P_{R,trans}^f}\right)^2 + \left(\frac{\Delta E_P^i}{E_P^i}\right)^2}. \tag{2.32}$$

Since $\Delta E_P^i / E_P^i$ is typically on the order of 10^{-3} [6], whereas $\Delta P_{R,trans}^f / P_{R,trans}^f$ is at best 10^{-2}, the resolution on the scattering angle is only limited by the resolution of the transverse momentum component of the recoil ion:

$$\Delta\theta_P = \left|\frac{\Delta P_{R,trans}^f}{P_{R,trans}^f}\right|. \tag{2.33}$$

2.2 Magneto-optical traps

In magneto-optical traps atoms are cooled and trapped in three orthogonal pairs of counterpropagating laser beams with circular polarization which intersect at the zero point of a magnetic quadrupole field [7, 8, 9, 10].

2.2.1 State of the art techniques

While the magnetic quadrupole field is produced by two magnetic field coils in anti-Helmholtz configuration, different techniques for producing the three counterpropagating laser beams are standard. The most common geometry is six laser beams arranged such that they form three mutually perpendicular standing waves which intersect at the zero point of the magnetic field. Each beam passes a quater waveplate prior to the trapping volume such that the necessary polarization is obtained. An alternative to the six beam MOT, which is more convenient when the available laser power is limited, is a three beam MOT in retro-reflected configuration. In this case a single beam is provided for the three dimensions, passing a quater waveplate prior to the trapping volume. Instead of shining in counterpropagating beams they are now provided by retroreflecting the beams in all three directions. After the trapping volume the beams pass a second quater waveplate, such that the light is again linearly polarized before being reflected on mirrors. They pass the quater waveplate again, such that the light has circular polarization again. One drawback of the three beam MOT as compared to the six beam MOT is that some of the incoming light is absorbed by the atom cloud and lost at the additional optical elements such that the retroreflected beam has reduced intensity.

A phase-stable MOT can be obtained using only one single laser beam being reflected such that all necessary beams for a MOT are present. This principle is used in a pyramidal MOT [44]. A single wide laser beam is incident on a hollow mirror having the shape of a pyramid, such that three pairs of counterpropagating beams are automatically produced. When the incident laser beam has σ polarization, each reflection from the two sides of the mirror generates two counterpropagating transverse beams with opposite polarizations (see figure 2.5). After two reflections of the incident beam a beam with opposite polarization as the incoming beam is produced, such that in every point of the pyramidal hollow region there always exist three pairs of counterpropagating beams with the needed polarization configuration for a MOT. One important application of the pyramidal MOT is found in the field of micro chips, where the pyramids can be directly etched into the silicon waver such that only a magnetic quadrupole field but no further optics is needed for the MOT. Recently, it has been proposed to use a pyramidal configuration for realizing a compact cold atom gravimeter [45].

Another type of MOT, in particular of interest for implementing MOTs on atom chips, is the mirror MOT [46] which is used to prepare ultracold atoms near the surface of the chips. Instead of the usual six laser beams only four beams, two of which are reflected on the mirror surface of the close-by substrate, are used. The corresponding magnetic trapping fields are produced by wires on the chip.

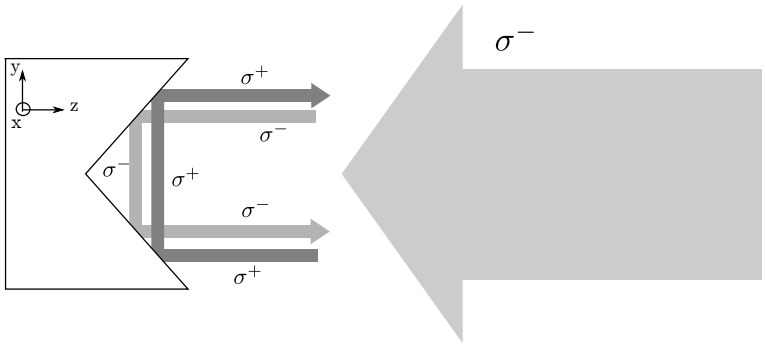

Figure 2.5: Working principle of a pyramidal MOT. The incoming laser has a σ polarization, each reflection from the two sides of the mirror generates two counterpropagating transverse beams with opposite polarizations.

2.2.2 Different regimes in a MOT and density increase in a dark SPOT

As discussed in [47] a MOT in steady-state, i.e. in a dynamical equilibrium between capture and loss processes leading to a constant number of atoms, can be divided broadly into four regimes. For a small number of atoms, the density is low and multiple scattering between the captured atoms can be neglected. This regime is called 'temperature limited regime'. At higher numbers of atoms rescattering among the trapped atoms is non-negligible, this is called the multiple scattering regime. In this regime the reabsorption of the trap light by trapped atoms results in an outward directed force on the atoms which counteracts the compressive magneto-optical force [47, 48, 49]. When the nonlinearity of the spatial dependence of the trapping force becomes important, the trap enters the 'two-component' regime. Finally, when there are too many atoms in the trap it becomes optically thick. This regime is discussed in [50]. In the following we look at the temperature limited regime and the multiple scattering regime in more detail, closely following the discussion in [51]. More details can be found in [47]. In particular we will discuss how a magneto-optical trap in dark spontaneous optical trap (dark SPOT) configuration, where the repumper is blocked at the center of the trap such that the atoms fall in a dark state for the cooling light, leads to an increase in density [18].

In the temperature limited regime, the interaction between atoms via re-scattering is insignificant and the trap volume density is defined by the temperature and an effective spring constant κ. κ is defined as the negative of the gradient of the force at the origin. The atomic spatial and momentum distributions are close to Gaussian and can be characterized by the temperature and the trap radius $r_{x,y,z}$ along each spatial direction, given by the equipartition theorem:

$$\frac{1}{2}\kappa_{ii} r_i = \frac{1}{2} k_B T. \tag{2.34}$$

κ_{ii} is the effective spring constant tensor. As the total number of atoms N in this regime is independent of the radius, the trap density is given by:

$$n_T = \frac{N}{2(\sqrt{2\pi}\, r)^3} \tag{2.35}$$

In this regime, the ultracold gas is compressible as n can be increased by higher spring constants κ_{ii}, e.g. due to a stronger magnetic field gradient. In a dark SPOT, atoms spend only fractions of their time in the upper state which decreases the spring constant κ by p, effectively leading to a decrease in atom density as more

atoms are transferred to the lower state. The density is then given by:

$$n_T^{DS} = \frac{N}{(\sqrt{2\pi})^3} \left(\frac{\kappa}{k_B T} \right)^{3/2} p^{3/2} \ . \tag{2.36}$$

In larger, standard MOTs the interaction between atoms by reabsorption of scattered trap light plays an important role and limits the density to typically 10^{10} atoms/cm^3. Townsend *et al.* [47] give a scaling law for the density dependence in this density limited (DL) regime on various trapping parameters.

$$n_{DL} = C_{DL} \frac{\kappa_0}{\lambda \hbar \Gamma} \frac{b}{b_0} \frac{\delta \Gamma}{\Omega^2}^{\frac{1}{2}}, \delta < 2\Gamma \tag{2.37}$$

where C_{DL} (~ 50) is a dimensionless constant, κ_0 is an experimentally measured proportionality factor for the spring constant, b/b_0 is the magnetic field gradient in units of G/cm, Γ is the natural line width and Ω the trap light Rabi frequency. The density here is proportional to the effective spring constant, which is reduced in a dark SPOT as p drops. The density limitation by re-scattering, however, is a two-body effect which scales with the square of p resulting in an effective inverse proportional relation of n_{DL} and p,

$$n_{DL}^{DS} = \frac{n_{DL}}{p} \tag{2.38}$$

which causes the density increase in the dark SPOT.

Chapter 3

Double charge transfer in ion-atom collisions

This chapter reports on experiments on double charge transfer in the system O^{6+} + Na(3s), performed in collaboration with the group of R. Hoekstra at the KVI (Kernfysisch Versneller Instituut) in Groningen, the Netherlands, where for the first time the energy-dependence of double electron transfer in alkali-ion collisions is investigated [52]. The results can be compared to double charge transfer in helium-ion collisions which has been subject to intense investigation by several groups in the past 20 years [53, 25, 54, 55, 56, 57, 58, 59, 60]. In helium, the electrons are bound in the same shell, as compared to alkalis, where the two outer electrons are in different shells leading to an asymmetric electron configuration in the target atom.

In the first section an introduction to the field of double charge transfer is given. The KVI-MOTRIMS setup will shortly be summarized in section 3.2, only including the most important features. A more detailed description can be found in [37]. The experimental results and their discussion follows in section 3.3.

3.1 Double Electron Transfer

Interactions between highly charged ions and neutral atoms are of interest for the fundamental understanding of plasmas and stellar formation. Moreover, it is an interesting system in itself, since it allows for studies of dynamics in quantum-mechanical many-body systems. Depending on the interaction energy of the ion-atom system three different processes occur: for projectile velocities higher than the orbital velocity of the active electrons, impact ionization is dominant, for projectile velocities close to the orbital velocity of the active electron, excitation or resonance phenomena might occur, whereas for projectile velocities lower than the velocity of the active electrons impact ionization can be neglected and electron transfer is the dominant mechanism. However, also the projectile charge state needs to be taken

into account. In a classical picture, electron transfer can occur when the potential barrier between the projectile and the target is lower than the first ionization energy I_1 of the target atom, i.e. when the total energy of the active electron is negative with respect to the projectile, which occurs at a critical internuclear distance. This distance depends on the charge state q of the projectile and is the case for $v_\mathrm{P} < q^{1/4}\sqrt{I_1}$ [61, 62]. The electronic structure of atoms with multiple electrons still lacks a full theoretical description from first principles since the total wavefunction is not separable. In order to understand these interactions, electron transfer of more than one electron is of particular interest, since correlation effects can be studied.

The transfer of two electrons in collisions of highly charged ions and atoms results in the creation of doubly excited $nln'l'$ projectile states:

$$\mathrm{A}^{r+} + \mathrm{B}(n_0 l_0 n_0' l_0') \rightarrow \mathrm{A}^{(r-2)+}(nln'l') + \mathrm{B}^{2+}. \tag{3.1}$$

$n_0 l_0 n_0' l_0'$ are the quantum numbers of the transferred electrons bound in the target atom prior to the collision. Depending on the final n states, the projectile can then stabilize in different ways, either through photon emission, leading to true double capture (TDC) or it can be ionized through an Auger decay, where one electron is ejected to the continuum leaving a doubly-charged target while the projectile only retains one captured electron (known as transfer ionization TI or autoionizing double capture). In the past two decades double-charge transfer between highly charged ions and noble gas targets, mostly helium targets, has been studied extensively [63, 25, 64, 62, 65, 56, 58, 57, 60]. One general finding was that after the collision the projectiles with electrons in a symmetric or close to symmetric state ($n \approx n'$) tend to autoionize rapidly, while projectiles which captured electrons in a very asymmetric state ($n \ll n'$) are more likely to stabilize radiatively.

Understanding these different population mechanisms led to a large debate in the literature [64, 65, 58, 60]. In particular for ions colliding with noble gases the population of doubly excited states with quite different n values seems to occur through a correlated transfer excitation, involving electron-electron interaction, as opposed to transfer in symmetric states, which happens in a two-step monoelectronic transfer, where one electron is transferred at a time, at a crossing of the initial channel and a single-capture curve or at a crossing between a single- and a double capture curve.

All these experiments used supersonic gas jet targets, limiting the available atomic targets to noble gases, such that the study is limited to electron capture involving two equivalent electrons. The advent of cold atom targets renders the study of electron capture for non-equivalent electrons possible [11]. Here, magneto-optical trapped atoms are used as targets. Due to the electronic structure of alkalis, having

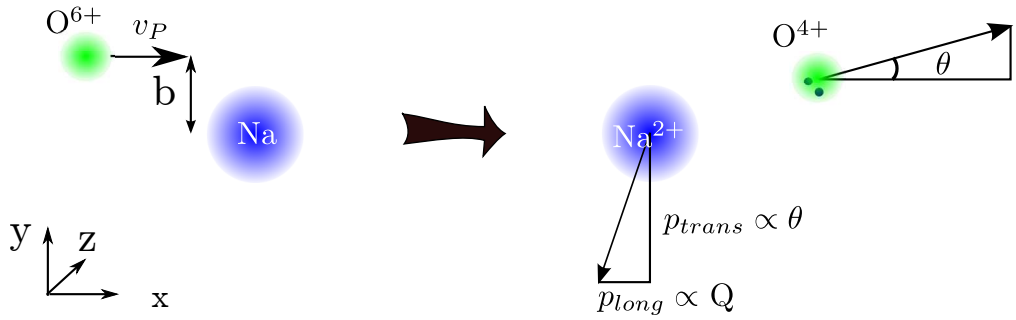

Figure 3.1: Sketch of ion-atom collision leading to double charge transfer in the system O^{6+} + Na(3s) with projectile energy v_P and impact parameter b. The x-component, p_{long}, is proportional to the Q-value, also called inelasticity of the collision, while the y- and z-components are proportional to the scattering angle θ and thus the transverse momentum p_{trans} of the recoil ion.

	Na^+	Na^{2+}	Na^{3+}
Q-value [eV]	-4.3	-21.1	-28
R_{in} [a.u.]	31.2	5.1	4.3
σ [10^{-16}cm^2]	400	3.1	2.0

Table 3.1: Q-value, capture radius and total cross sections for up to three electron transfer estimated using the classical over the barrier model for the investigated system O^{6+}+ Na(3s) for a projectile energy of 6.75 keV/amu.

a closed cooling cycle, alkalis can be cooled and trapped easily in MOTs. Nowadays a whole zoo of different elements, not limited to alkalis, has been successfully trapped.

The first experiment on transfer of two nonequivalent electrons has been performed by S. Knoop with the system O^{6+} + Na($3s$) at a collision energy of 7.5 keV/amu [52]:

$$O^{6+} + \text{Na}(1s^2 2s^2 2p^6 3s^1) \rightarrow O^{4+}(nln'l') + \text{Na}^{2+}(1s^2 2s^2 2p^5). \tag{3.2}$$

A sketch of the collision is shown in figure 3.1.

Using the classical over the barrier model (see appendix A) estimates on the expected cross-sections, Q-values and capture radii are made for up to transfer of 3 electrons and summarized in table 3.1. Due to the large difference in binding energy of the two outer electrons, the difference in the presented values is large. The cross sections for double charge transfer are expected to be two order of magnitude smaller than for single charge transfer. Also, the capture radius is reduced from 31 a.u. to only 5 a.u., leading to much larger transverse momenta.

In order to gain more insight into the dynamics of the double electron transfer of two nonequivalent electrons, we have extended this measurement to a larger projectile energy range. By changing the projectile's velocity, the effective interaction time can be varied and dynamics during the charge transfer can be investigated.

3.2 Sodium target MOTRIMS setup

This section presents the MOTRIMS setup at the KVI in Groningen where the experiments have been performed. A detailed description of the setup can be found in [37], in this work only the most important features of the experiment will be summarized, following the diploma thesis of I. Blank [17].

3.2.1 Laser system and magneto-optical trap for sodium atoms

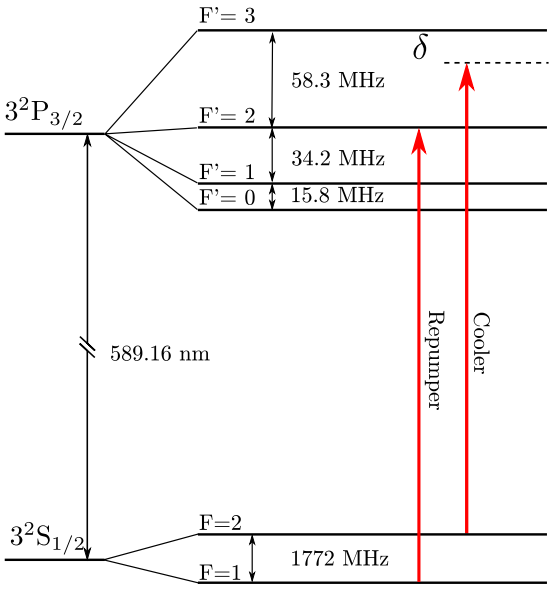

Figure 3.2: Hyperfine level splitting of the D2 line of Na. The cooling laser is 20 MHz red-detuned to the $F = 2 \rightarrow F' = 3$ transition. The repumper pumps atoms from the $F = 1$ ground state, which cannot be addressed by the cooler, to the $F' = 2$ excited state and thus back to the cooling cycle.

Sodium can be trapped in a magneto-optical trap rather easily since it has a closed transition on the D2 line, which is used for cooling. Due to the nuclear spin of ^{23}Na,

I=3/2, the $3^2S_{1/2}$ ground state splits into two hyperfine sub-levels $F = 1$ and $F = 2$ and the excited state $3^2P_{3/2}$ splits into four substates $F' = 0, 1, 2$ and 3. The energy level scheme is shown in figure 3.2. The cooling beam is 20 MHz red-detuned from the $F = 2 \rightarrow F' = 3$ transition. Since the energy level splitting of the excited state is of the same order of magnitude the atoms can also be excited non-resonantly to the $F' = 2$ state. From this state the atoms decay to the $F = 1$ ground state, which is a dark state for the cooling light. These atoms are pumped back into the cooling cycle by the repumper, which is resonant to the $F = 1 \rightarrow F' = 2$ transition. Furthermore, due to the degeneracy of the substates of $(2F + 1)$ statistically 3/8 of the atoms are initially in the $F = 1$ state. The repumper also pumps these atoms into the cooling cycle.

In the setup at the KVI all necessary beams are provided by a single single-frequency ring dye laser (Model 380D, Spectra-Physics, Rhodamine 6G dye) [66] which is pumped by a solid state cw laser (Millennia Vs, Spectra-Physics). A beam splitter is used to split off 1% of the beam intensity which is fed into the Stabilok locking system (Spectra Physics model 388 and controller) and the saturated spectroscopy to lock and monitor the frequency. The Stabilok uses interference fringes from a Fabry-Perot etalon for the frequency stabilization. An external frequency stabilization using saturated absorption spectroscopy is used to lock the laser frequency more steadily about 80 MHz red-detuned from the $F = 2 \rightarrow F' = 3$ transition.

The pump laser is operated at an intensity of 4.0 W which leads to an output power of the ring dye laser of 300 to 400 mW at 589.6 nm, i.e. the D2 line of Na. The main part of the beam passes an 1720 MHz electro-optical modulator (EOM) to modulate sidebands on the laser. The first order, shifted 1720 MHz to the blue, is used as the repump beam, while the zeroth order is used as the cooling beam. Both beams are transported to the chamber using a polarization maintaining fiber where they are coupled out and split up into the necessary beams.

The sodium atoms are provided by an oven usually operated at 150°C. In order to increase the number of slow atoms from the oven, a far red-detuned laser beam counterpropagates the atom beam. These atoms are trapped in a retroreflected MOT which typically consists of 10^6 atoms in a volume of 1-5 mm^3 [37]. However, no measurements of the atom number, density or temperature are available for the data presented in this work. In order to create the cooling beam for the oven and the trapping beam for the 3D MOT the beam passes two AOMs after outcoupling of the fiber. The first-order diffracted beam of AOM1 is used for trapping after being split up into three beams by polarizing beam splitters. The zeroth-order passes a second AOM, which is only used for switching (see figure 3.3). Due to the locking scheme the zeroth order is still red-detuned by 80 MHz to the cooling transition and counterpropagates the atom beam from the oven to provide cooling.

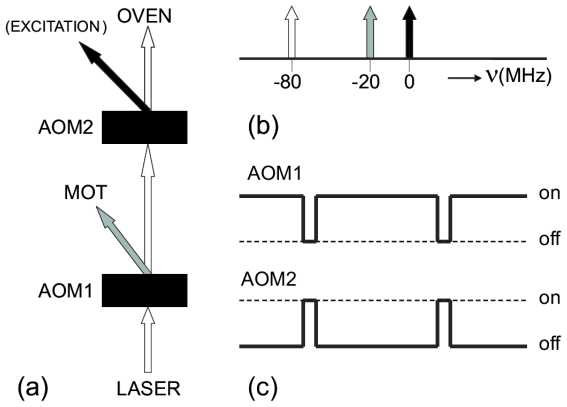

Figure 3.3: Schematics of AOM arrangement at KVI. Part a) shows the splitting of the beam into cooling and trapping beam (MOT) and longitudinal cooling beam (Oven). The beam for excitation is not used in the experiment. Part b) shows the detunings of the beams and c) shows the switching of the light. Taken from [37].

The magnetic quadrupole field for the MOT is created by water cooled coils in anti-Helmholtz configuration with 20 windings each. Applying a current of 80 A leads to a magnetic field gradient of 30 G/cm. In addition, two pairs of Helmholtz coils are used as steering coils (30 windings, 2 A) to move the MOT cloud 2 mm in y- (horizontal, perpendicular to the ion beam axis) and z-(vertical) direction to optimize the overlap with the projectile beam. The pressure in the vacuum chamber is of the order of 10^{-9} mbar at an oven temperature of 150°C.

3.2.2 Electron cyclotron resonance ion source

The projectile ion beam is provided by a homebuilt 14 GHz CAPRICE-type Electron Cyclotron Resonance Ion Source (ECRIS), where multiply charged ions are created by sequential electron impact ionization. For more details refer to [67].

The source can be floated up to 26 kV. This voltage defines the velocity of the projectile ions. However, during the run of this experiment the source produced sparks already at a voltage of 23 kV, and therefore 8.25 keV/amu is the highest projectile velocity obtained[1]. The ions are extracted by a movable puller lens. After the extraction a 110° magnet is used for mass-over-charge-ratio selection. Afterwards the ions are focused by three magnetic quadrupoles and 45° bending magnets lead the ion beam to several experiments positioned along the beam line. Before the

[1]For the experiments reported on in this work only O^{6+} is used.

MOTRIMS experiment the beam is again focused by two magnetic quadrupoles and passes four diaphragms. The first diaphragm is placed 81 cm before the collision center. Between first and second diaphragm, which has a diameter of 1 mm, a beam deflector provided by a plate capacitor is placed. A high voltage pulse can be applied to one of the capacitor plates of the deflector, which sweeps the beam over the second diaphragm creating a pulsed beam. The two additional diaphragms, both having a diameter of 1 mm, are used to achieve better collimation of the projectile beam. The voltages on the deflector plates have been adjusted during the experiment depending on the projectile energy. Thus the shape, the temporal distribution and the size of the projectile beam at the collision center might vary slightly for different measurements and is unknown. After crossing the chamber the projectile ions are collected in a Faraday cup where the current is measured. For different projectile velocities the ion beam currents in continuous mode vary between 85 and 43 nA, dropping by three orders of magnitude when being switched.

3.2.3 Recoil ion momentum spectrometer

The projectiles collide with the target atoms at the center of a recoil ion momentum spectrometer. After the collision the recoil ions are extracted by a transverse extraction field and detected by a two-dimensional position sensitive detector shown in figure 3.4. The recoil ions from the MOT are accelerated in a 7 cm long extraction field after which they freely propagate in a 41 cm long field-free drift region before being detected on a position sensitive detector. In order to create the extraction field the push electrode plate is set to a positive voltage U_{Push}, while the drift tube is on a negative voltage U_{Drift}, as shown in figure 3.4. In order to focus recoil ions starting from different positions but with same momentum onto the same spot on the MCP an additional three ring electric lens is included in the extraction region. Each of the ring electrodes can be set on different voltages U_1, U_2 and U_3. For the detection of Na^{2+} recoils following voltages have been applied: $U_{\text{Push}} = +8.1V$, $U_{\text{Drift}} = -19.6V$, $U_3 = -13.6V$, $U_2 = -14.8V$ and $U_1 = +2.0V$. The spatial distribution of the recoils on the MCP is detected by a two-dimensional delay-line anode (DLD40) from Roentdek [68]. A detailed description on the working principle can be found in 4.6.3. With a TDC resolution of 133 ps per time bin, the bin to position conversion factor of 0.09 mm/bin or 11 bins/mm is obtained for this detector.

3.2.4 Switching schemes

The timing sequence used in the experiment to measure the Na^{2+} spectrum is shown in figure 3.5. At the beginning of each duty cycle, the magnetic trapping field is

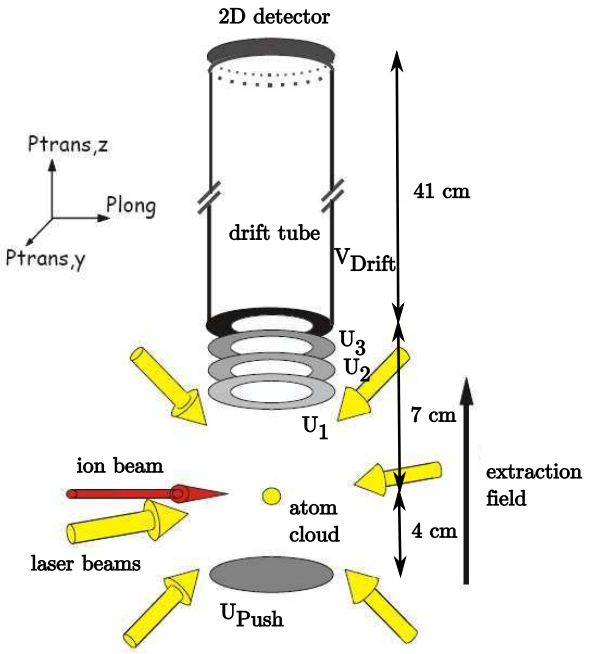

Figure 3.4: Schematic of the Na MOTRIMS setup at the KVI in Groningen. The target atoms are trapped inside the spectrometer. Recoil ions are extracted perpendicular to the incident projectile ion beam (transverse extraction) and detected on a two-dimensional position sensitive detector. The electric field is generated by applying a voltage U_{Push} to the pushing plate and a voltage U_{Drift} to the drift tube. The voltages U_1, U_2 and U_3 can be applied independently. Adapted from [37].

switched off for 5 ms in which the collisions take place. The switching of the magnetic trapping field is necessary to avoid distortion of the trajectories of the recoil ions, which would lead to a reduction in the resolution. After a delay of 1 ms, taking into account the finite switching time and eddy currents of the magnetic field, the projectile beam is swept across the second diaphragm every 70 μs. Only every second ion pulse triggers the experiment. This leaves time for 28 sweeps. After 5 ms the magnetic field is turned on again for 10 ms in order to allow the MOT to restore itself and the cycle is repeated.

Due to measurements from [37], revealing that the atom number does not decrease significantly for 10 ms when the trapping lasers are left on during turn off of the quadrupole field, the cooling and trapping lasers are not switched with the magnetic quadrupole field. Instead the lasers are switched off with a variable delay $\Delta T = 40$ - 50 μs before the ion beam is swept across the atom cloud (falling edge of the TTL

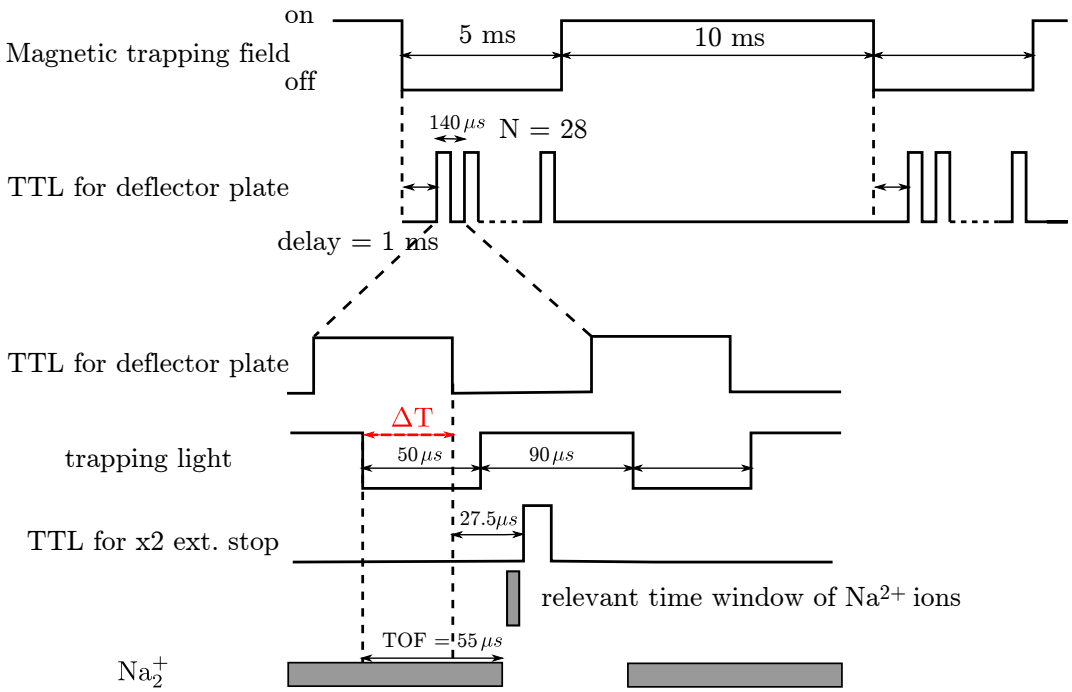

Figure 3.5: Switching scheme of the magnetic quadrupole field, the projectile ion chopper signal, the cooling lasers and the TDC trigger signal. The magnetic trapping field is switched off for 5 ms, every 70 μs the ion beam is swept across the second diaphragm leaving time for 28 sweeps. The ion beam interacting with the atom cloud is produced at the falling slope of the TTL for the deflector plate. The trapping light is switched off for 50 μs with a variable delay ΔT prior to the atom-ion interaction. The Na^{2+} recoil ions hit the detector after a time of flight of about 29 μs after the falling slope of the chopper signal. The gray bars indicated the times during which Na_2^+ ions produced in the MOT are detected (TOF = 55 μs). Note the different time scales for magnetic field and laser beam switching.

for the deflector plates). In the experiment ΔT is adjusted to account for different traveling times of the projectiles from the deflector plates to the collision region at different projectile velocities and is adjusted such that the recoil ions are recorded within the time window of the TDC. Switching off the trapping light is necessary for the following two reasons: First, all target atoms should be in the ground state during the collision. Second, the Na_2^+ molecules[2], which are produced in sodium

[2]For simplicity, these molecules produced by associative ionization will be called MOT molecules in the following.

MOTs via associative ionization of the excited Na atoms [69],

$$\mathrm{Na}^*(3p) + \mathrm{Na}^*(3p) \rightarrow \mathrm{Na}_2^+ + e^-, \tag{3.3}$$

should already have reached the detector before the spectrum of the Na^{2+} ions is recorded. The time for the atoms to decay back into the ground state can be neglected compared to the time of flight of the Na_2^+ ions, which is about 55 μs. The recoil ions produced in the collision with the projectiles, Na^{2+}, have a time of flight of only 27 μs (cf. figure 3.5). In order to avoid MOT molecules in the recorded spectra the trapping lasers are thus switched off early. A delayed signal from the TTL for the deflector plates is further used to provide an external stop to the TDC which delivers the TOF information. After 50 μs the trapping light is switched back on for 90 μs such that the MOT can restore itself.

3.2.5 Data acquisition

Position of the recoil ions on the detector are recorded using a delay-line anode. This delay-line detector is read out by a TDC. The delay-line signals are labeled X_1, X_2, Y_1 and Y_2. A scheme of the data acquisition is shown in figure 3.6. The start of the TDC is provided by one of the delay-line signals, X_2, such that a measurement is only started when an actual ion signal is detected. The other three delay-line signals X_1, Y_1 and Y_2 are used as stops. A fourth stop is given by the delayed signal which switches the deflector plates providing the pulsed ion beam. In order to ensure that the start signal always arrives before the stop signals, all stop signals are delayed. The TDC is read out by a C++ based program (CoboldPC: Computer Based Online and Offline Listmode Dataanalyzer [68]) which reassigns the coordinates as follows: $X_1 = x_1$, deflector signal $= x_2$, $Y_1 = y_1$, $Y_2 = y_2$. In this configuration one spatial coordinate is directly given by $X = -x_1$. The other spatial coordinate is obtained from the difference of two signals of corresponding ends of the delay-line $Y = y_2 - y_1$. The time of flight is given by the signal triggering the deflector plates $T = -x_2$. It is delayed by 27.5 μs such that it always arrives after the Na^{2+} recoil ions, which initialize the TDC, and have a time of flight of 27 μs.

Due to the transverse extraction geometry used in the spectrometer at KVI, the measured recoil ion spectra are translated into physical quantities as follows: The X-position on the detector, which is parallel to the projectile beam, is directly proportional to the longitudinal momentum transferred to the recoil ion. As we saw in subsection 2.1.5

$$p_{long} = a_{\parallel} X. \tag{3.4}$$

Thus a constant links time bins to the longitudinal momentum in a.u.. The energy

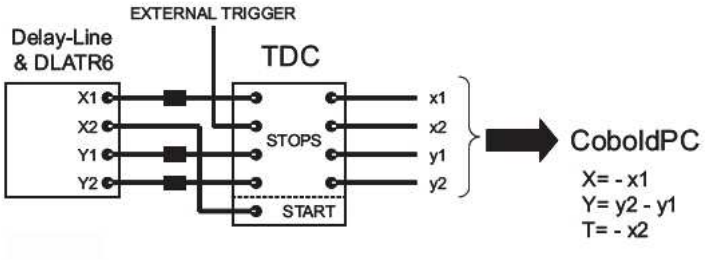

Figure 3.6: Scheme of the data acquisition of the delay-line and the TDC: In order to reduce the amount of false start signals, the TDC is started only when a signal is recorded by the delay-line (X_2). The other three delay-line signals X_1, Y_1 and Y_2 are delayed, indicated by blocks, which ensures that the start signal always arrives before the stop signals. An external trigger signal, which is derived from the signal that triggers the ion beam pulse, serves as the forth stop signal. The times x_1, x_2, y_1 and y_1 measured with the TDC is read out by a PC using the program CoboldPC, which converts the signals into positions X and Y on the detector and time of flight T. Taken from [37].

transferred, the Q-value, is obtained from equation 2.19:

$$Q = v_P(p_{long} + 0.5 n_C v_P), \tag{3.5}$$

with n_C being the number of electrons captured. The conversion factor $a_{\|}$ is obtained from a single-charge transfer spectrum where the main capture channels are well-known [37]. The obtained conversion factor then scales with the square root of the recoil-ion's charge state. The charge state gives the conversion for the X-component of the recoil ion of 12.6 time bins = 1 a.u..

The time of flight and the Y-position of the recoil ions on the detector translate to the transverse momentum components of the recoil ions. Assuming perfect cylindrical symmetry of the detector the same conversion factor $a_{\|}$ obtained for the longitudinal momentum component is used for conversion of the Y-position to the corresponding transverse momentum component. For the time of flight no direct calibration was made in the experiment. The conversion factor is thus chosen such that the transverse momenta have the same magnitude in time of flight and Y-direction. This ad-hoc assumption is *a priori* not justified and leads to a systematic error which cannot be determined.

Using this data acquisition scheme, a raw 2 dimensional detector image as shown in figure 3.7 is obtained. As we saw in subsection 3.2.4, Na_2^+ molecules are constantly produced in a Na MOT by associative ionization by the cooling beams [69]. Following the switching scheme discussed above, we still record MOT molecules in

all recoil ion spectra. The origin of this peak is not understood. However, since these molecules are produced from previously trapped atoms[3], they have almost no initial momentum and can thus be used to determine the origin of the momentum distributions in the longitudinal and transversal Y-direction. Using a spectrum obtained only from ions from a MOT, a two-dimensional Gauss fit on the two-dimensional distribution of the MOT molecules has been performed. It has been verified that the position of this peak does not change in the presence of the ion beam and for different projectile velocities. Using recoil spectra from ions produced in the MOT, the zero of the momentum for the Y-component has been determined to be -97.925 bins and 333.55 bins for the X-component. Assuming a perfectly round MOT and a cylindrical symmetric spectrometer leads to a round projection of the MOT ions on the detector. The difference in $1/e^2$-width of the Gaussian fit has been used to determine the error on the calibration of the Y-component and has been determined to be 10 %. For the time of flight component, the time which corresponds to zero momentum is found by fitting a Gaussian to the TOF distribution.

3.3 Experimental results

In this section the experimental results on the energy dependence in the process of double charge transfer in the system O^{6+} + Na(3s) obtained at the KVI in Groningen are presented. The measured Na^{2+} recoil ion spectra are presented and discussed.

3.3.1 Determination of the inelasticity of the charge transfer

The data set consists of seven measurements at extraction energies ranging from 22 kV down to 10 kV, covering almost a factor of two in the velocity of the projectile, from $v_P = 0.58$ a.u. down to $v_P = 0.39$ a.u.. The obtained data will be discussed based on one exemplary data set obtained for projectile energies of E_P = 6.75 keV/amu. The analysis of the data obtained for the other energies is done accordingly.

The two-dimensional detector image shows the projection of the three-dimensional data onto the xy-plane. The third dimension is the time of flight component, which is proportional to one of the transverse momentum components. The second transverse momentum component, $p_{trans,y}$, is obtained from the Y-position of the recoil ion on the detector and the Q-value is obtained from the X-position of the recoil ion, which is parallel to the propagation axis of the projectile beam. For comparison, two raw

[3]This peak must originate from the MOT since it disappears when the magnetic quadrupole field and the trapping lasers are switched off.

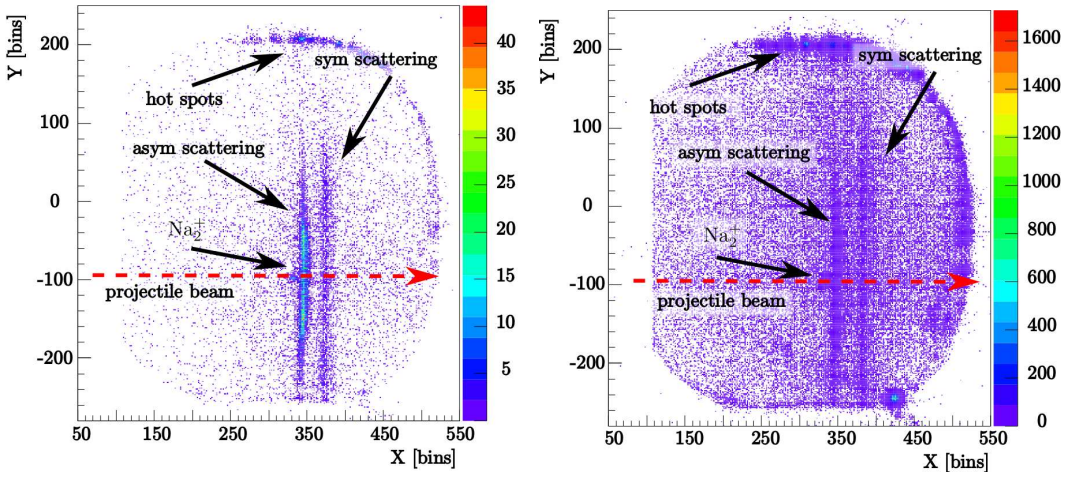

Figure 3.7: Raw detector image obtained with the delay line at the MOTRIMS setup at KVI for $v_P = 0.52159$ a.u. (a) and $v_P = 0.3887$ a.u. (b). The peak originating from molecules produced in the MOT is seen. For lower projectile velocities the cross section for double charge transfer decreases, leading to longer measurement times and thus larger background. The counts at the edge of the detector are hot spots.

data sets are shown in figure 3.7, one for high projectile velocity $v_P = 0.52159$ a.u. and one for a low velocity $v_P = 0.3887$ a.u..

In contrast, a sample of a two-dimensional detector image for $v_P = 0.52159$ a.u. showing the region of the detector plane used for further evaluation is depicted in figure 3.8. The raw data shows two lines in Y-direction which correspond to population of different states in the projectile. The lines do not lie in the center of the detector since the recoil ions did not hit the detector at its center. For the configuration of the spectrometer used in the experiment, recoil ions with large negative momentum components are not projected onto the detector and are thus not recorded. In order not to underestimate the channels with large transverse momenta, only the recoil ions with $p_{\mathrm{trans,y}} > 0$ a.u. are used for further data analysis. This is justified since the negative transverse components are the same as the positive ones due to the cylindrical symmetry (see section 2.1.2). The remaining edges of the detector show artifacts which are due to the detector and are not included in the further analysis. The zero momenta for this data is obtained from the 2D fit on ions resulting from MOT ions (see subsection 3.2.5).

For low projectile velocities, one line appears at $Y = 0$ which originates from non-perfect adjustment of the CFD and are filtered out in the data analysis. The peak of the MOT molecular ions can be seen in both raw detector images, lying

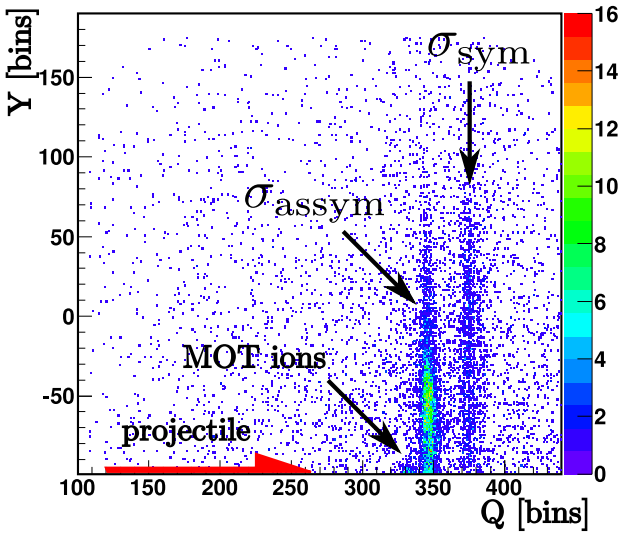

Figure 3.8: Two-dimensional detector image containing the data taken at a projectile energy of 6.75 keV/amu and used for further analysis, integrated over time of flight. Recoil ions with large negative transverse momentum in y-direction are not projected onto the detector. Due to the cylindrical symmetry only the upper half of the transverse momentum distribution is therefore used for further data analysis.

at Y = -98 bins and X = 333 bins. For lower projectile velocities the total cross section for double charge transfer is lower such that, in order to get good statistics, the measurements are longer and thus the background is bigger.

In order to obtain the inelasticity of the double-charge transfer, the data for $p_{\mathrm{trans,y}} > 0$ is projected onto the x-axis. The result for the above data set taken at 6.75keV/amu is shown in figure 3.9. In particular, two main peaks can be distinguished: a large population with a Q-value just below 0 and a double peak structure at smaller Q-values, Q $<$ 30 eV.

Assignment of the experimentally obtained Q-values to the final states in the projectile can be done if the binding energies of the projectile are known. The relevant Q-values for doubly excited $O^{4+}(1s^2nlnl')$ are taken from [70] and are summarized in table 3.2. Due to the non-degeneracy of the l-states the Q-values of the corresponding n-states have a certain width.

With this knowledge the different channels being populated in the collision and shown in figure 3.9 can be assigned: The main peak with Q $<$ 20 eV can be assigned to the population of the states $3ln'l'$, where $n' \geq 5$. The channel corresponding to transfer ionization with one-electron capture into the $O^{5+}(1s^23l)$ state is strongly suppressed. From this one can conclude that transfer ionization plays a minor role

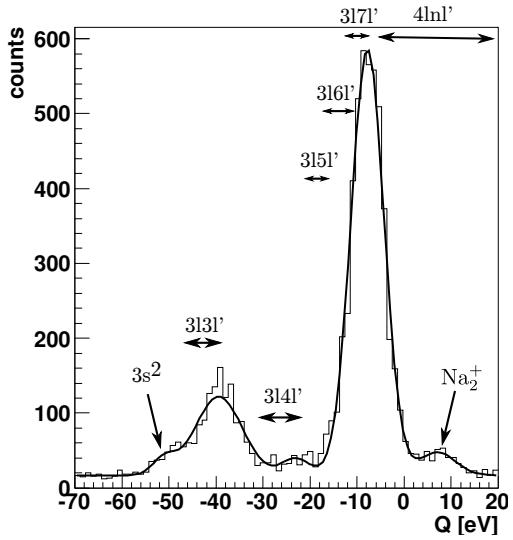

Figure 3.9: Q-value distribution for a projectile energy of 6.75 keV/amu. Population into the asymmetric/symmetric states is shown. The relative cross sections are obtained by integrating over the Gaussian distributions. The peak with positive Q-values originates from Na_2^+. Also shown are the energy ranges for the corresponding channels (cf. table 3.2), taken from [70].

at this impact energy. The channel $3l4l'$ lies between the two main peaks and shows a small population. The second double peak which occurs at smaller Q-values can be attributed to the transfer of electrons in the symmetric final states $3l3l'$ and $3s^2$.

3.3.2 Transverse momentum distribution

Due to the extraction geometry, both the time of flight and Y-component of the data are proportional to the transverse momentum distribution. The transverse momentum distribution in time of flight direction is deduced from the signal given from the deflector plate. Since the projectile beam has, depending on the projectile energy, a time spread of a few hundred ns, the resolution in this direction is poor and the momentum distribution is smeared out. For the population of the different channels the transverse momentum distributions are plotted in figure 3.10 for an energy of 6.75 keV/amu. The left graph shows the distribution for charge transfer into the asymmetric channels ($3ln'l'$, $n' \geq 4$), whereas the right graph shows the distribution for transfer into the symmetric states ($3l3l'$ and $3s^2$). A histogram of the obtained transverse momentum distributions is shown in figure 3.11. The asymmetric channels show a smaller transverse momentum, which peaks around $p_{\text{trans}} = 4.5$ a.u.,

$O^{4+}(1s^2nln'l')$	state	Q-value (eV)
$2s^2$		-200
$2ln'l'$	n'=2	-189 → -164
	n'≥3	-132 → -86
$3s^2$		-54
$3l3l'$	l,l'≥1	-48 → -40
$3ln'l'$	n'=4	-31 → -22
$3ln'l'$	n'=5	-21 → -15
$3ln'l'$	n'=6	-17 → -11
$3ln'l'$	n'=7	-14 → -9
$3ln'l'$	n'≥8	-12 → -2
$3s$	n'=∞	-6
$4ln'l'$		-6 → 22

Table 3.2: Relevant Q-values for doubly excited $O^{4+}(1s^2nln'l')$ resulting from double electron transfer in collisions of O^{6+} with Na($3s$). The binding energies for $O^{4+}(1s^2nln'l')$ are taken from [70].

whereas the symmetric channel has a much broader momentum distribution and peaks at around $p_{\text{trans}} = 8$ a.u.. Transfer into the asymmetric channels thus leads to a smaller scattering angle of the projectile ($\theta = -p_{\text{trans}}/(mv_P)$) and indicates a larger impact parameter than the transfer into the symmetric channels. Furthermore, the transverse momentum distribution of the symmetric channels moves to larger momenta for smaller collision energies.

The investigation of the collisions leading to large momenta transfer suffers from an experimental constraint; the TDC has a finite time window of only 2.2 μs after being triggered. For the current configuration of the spectrometer this time windows corresponds to a total maximum detectable transverse momentum of ±10 a.u.. Since the transverse momenta originating from the population into the symmetric channels is partially larger than 10 a.u., data gets cut in time of flight direction. This cut leads to an underestimation of the population in the symmetric states. In the data analysis this underestimation thus needs to be corrected for. The details on this corrections can be found in appendix B.

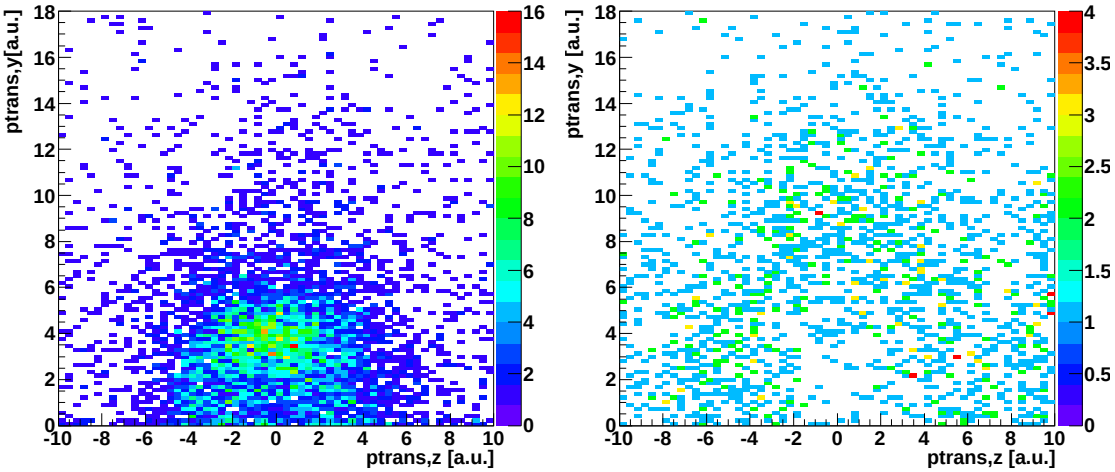

(a) Charge transfer into asymmetric channels **(b)** Charge transfer into symmetric channels

Figure 3.10: Transverse momentum distribution of Na^{2+} at 6.75 keV/amu. Depending on the channels which are populated during the collision, the transverse momentum of the recoil ions is smaller ((a) population of asymmetric channels) or larger ((b) population of symmetric channels), indicating a different transfer mechanism.

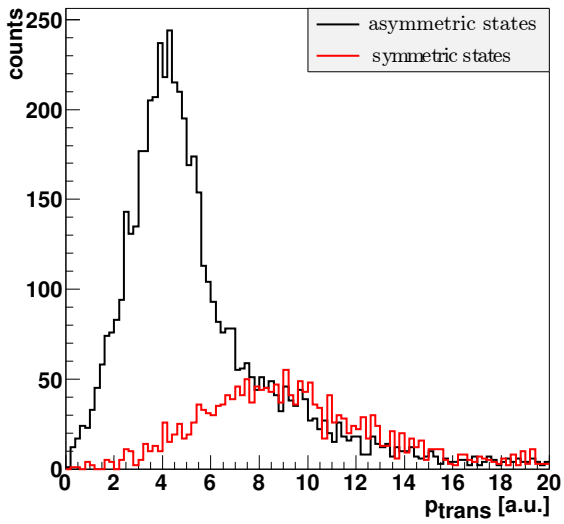

Figure 3.11: Histogram of transverse momentum distributions. Shown are the transverse momentum distributions at 6.75 keV/amu for the symmetric states (black) and the asymmetric states (red).

3.3.3 Discussion

The transverse momentum distributions, which are proportional to the impact parameters, indicate different transfer mechanisms for the population of symmetric states ($3l3l'$ and $3s^2$) than for the population of asymmetric states ($3ln'l', n' \geq 4$). A simplified picture can be obtained from Coulomb potential curves and is sketched in figure 3.12. The discussion follows the ones in [53, 25, 54, 55, 56, 57, 58, 59, 60]. The entrance channel has zero initial energy. On the way in, the Coulomb potential curves are crossed at different internuclear distances. At each crossing, there is a certain probability that the crossing channel can be populated. At large internuclear distances a monoelectronic transition might occur (square). In case of a transfer the system then follows the single-capture curve until it crosses a double capture curve at smaller internuclear distances where a second monoelectronic transition might occur for the second electron (circle). This is a two-step process. Another population mechanism of the double capture channels, involving a dielectronic process, which

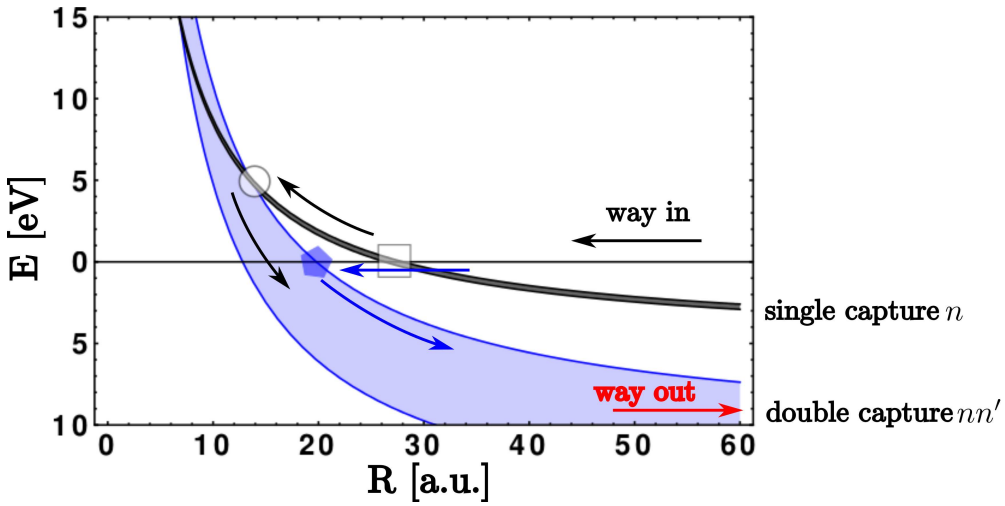

Figure 3.12: Sketch of Coulomb potential curves indicating different charge transfer mechanisms. The system enters with zero initial energy. At a crossing with a single charge transfer curve, an electron has a certain probability to populate this channel (square), and at smaller internuclear distances a certain probability to populate the double charge channel (circle). The double capture channel might also be populated directly (polygon) at smaller internuclear distances. Smaller internuclear distances lead to bigger transverse momenta of the recoil ion. The double capture channel is broad due the degeneracy of the different l-states (shaded area). The difference in energy between the entrance and the exit channel at infinite internuclear distance corresponds to the Q-value.

has been denoted correlated double capture (CDC) [25, 64], might also occur directly at smaller internuclear distances, where the entrance channel crosses directly the double capture channel (polygon). A third mechanism, known from helium-neon collisions, is a correlated transfer and excitation mechanism where the channels can be populated by a two-step process via single electron capture curves similar to the two step process discussed above. First a monoelectronic transition feeds an intermediate state n corresponding to a single electron capture channel. Through electron-electron interaction the second electron is transferred to a second n' orbital while the first electron is promoted to a higher lying orbital $n_2 > n$ [71, 64]. After the transfer on the way out the system follows the populated channels. The energy of the populated channel corresponds to the difference in energy of the entrance channel and the populated channel at infinite nuclear distance and is given by the Q-value. The Coulomb potential curves for the system O^{6+} + Na(3s) are depicted in figure 3.13. Population of the symmetric channels might occur in a double electron capture process at small internuclear distances. As seen from the Coulomb potential curves in figure 3.13 (b), the internuclear distance for crossing with the $3l3l'$ channel happens at R = 4 - 5.5 a.u., population into $3s^2$ at even smaller internuclear distances of R = 4 a.u..

This can be compared to calculations using the CBM, where electron transfer is described in a quasi-molecular picture and multiple electron transfer happens in one step. Furthermore, CBM calculations predict that double electron capture can only occur for internuclear distances $R_{in} < 5.1$ a.u.. In the experiment we measure a transverse momenta of 8.5 a.u. for high projectile velocities (see figure 3.11). The dependence on the transverse momentum on the collision energy as predicted by CBM is shown in figure 3.14 (b). At high projectile energies of 6.75 kev/amu, CBM predicts transverse momenta on the order of 7.5 a.u.. This agrees well with the transverse momentum distribution we measure in the experiment which peaks at 8.5 a.u.. The CBM predicts higher transverse momenta for lower projectile velocities. As seen from figure 3.15 where the transverse momentum distribution for $v_P = 0.39$ a.u. is depicted we measure a higher transverse momentum for lower projectile velocities for population of the symmetric states, indicating that the transfer into the symmetric channels is well described by a one step transfer.

The experiment shows that the channels leading to the asymmetric states $3l4l'$ and $3l5l'$ are at best weakly populated, suggesting that at larger internuclear distances, R > 7 a.u., two-electron transfer between the entrance channel and the double capture channel is not likely. This indicates that the asymmetric channels can only be populated in a two step process. We therefore use the results from TC-BGM calculations (two-center basis generator mode) [52], calculating the transition probability as a function of impact parameters for single electron capture for the

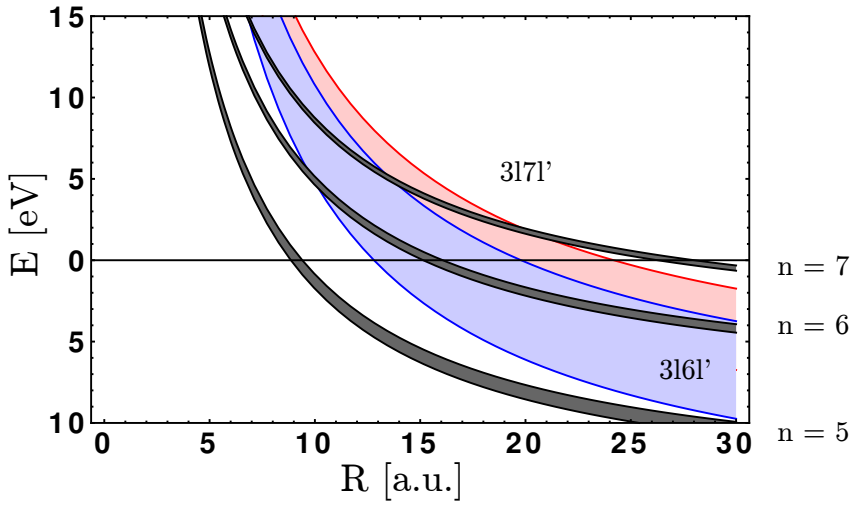

(a) Coulomb potential curves for two-step electron transfer in O^{6+} + Na(3s). Due to the strong coupling of the single capture curves n = 6 and n = 7 to the double charge transfer curves $3l6l'$ and $3l7l'$ this process is very likely.

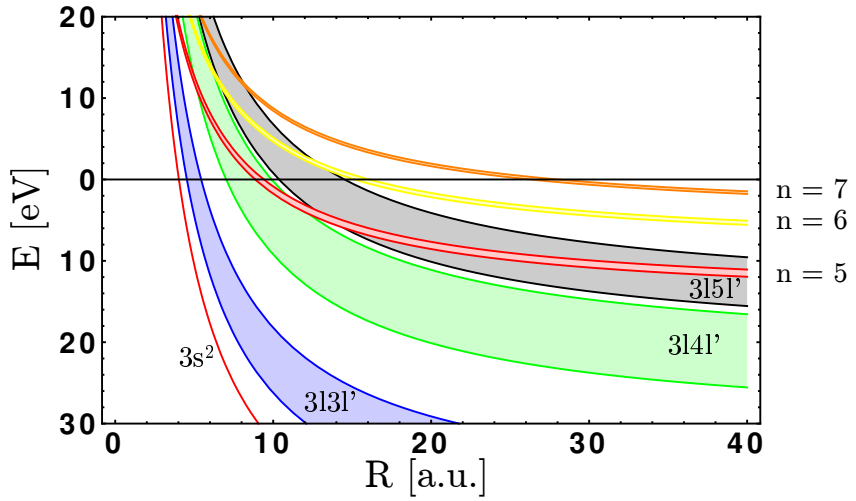

(b) Coulomb potential curves for one-step double charge transfer O^{6+} + Na(3s). One-step transfer into the double capture curves $3l4l'$ and $3l5l'$ is strongly suppressed since the single capture curves are already depleted (see figure 3.13 a), transfer into $3s^2$ and $3l3l'$ happens at small internuclear distances, leading to a large transverse momentum transfer on the recoil ion.

Figure 3.13: Coulomb potential curves for O^{6+} + Na(3s). Depending on the internuclear distance, the entrance channel crosses single or double capture curves. The crossings leading to double capture are at smaller internuclear distances, leading to bigger transverse momenta of the recoil ion. Due to the degeneracy of the l-states, the double capture curves are broad. The energy difference between the incoming and outgoing channel is the Q-value.

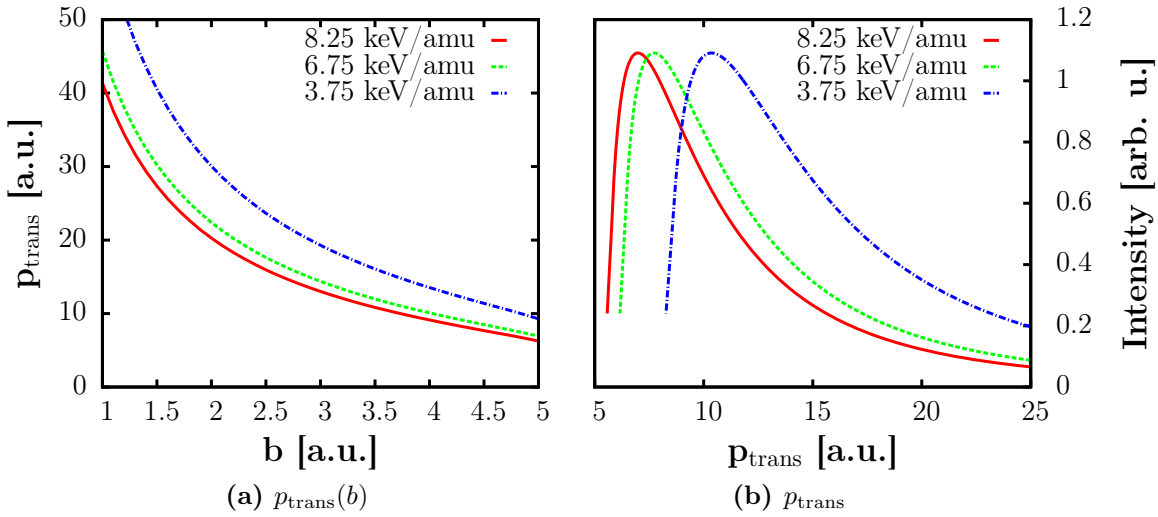

(a) $p_{\mathrm{trans}}(b)$ **(b)** p_{trans}

Figure 3.14: Estimation of the transverse momentum obtained for different impact parameters using the CBM (a) and on the transverse momentum distribution obtained for for double charge transfer in O^{6+}+ Na(3s). The transverse momentum distribution depends on the projectile velocity, shown are the maximum velocity of $v_P = 0.58$ a.u. (solid line), $v_P = 0.55$ a.u. (dashed line) and the minimum projectile velocity of $v_P = 0.39$ a.u. (solid-dashed line) measured in the experiment.

current system. It is shown in [37] that at internuclear distances of R >10 a.u., mainly the states with principle quantum number n = 7 and n = 6 are populated. As seen in figure 3.13 (a) these channels couple strongly to the $3l7l'$ and $3l6l'$ states, whereas the $3l5l'$ and $3l4l'$ band are only crossed at smaller internuclear distances (see figure 3.13 (b)) and might explain the very strong population of these states, as seen in the Q-value spectrum; the transfer into the asymmetric states occurs in a two-step manner, where in a single electron capture first the states $n = 6$ and $n = 7$ are populated. Population of $3l5l'$ and $3l4l'$ is strongly suppressed because of depletion of the incoming single electron captures at larger internuclear distances. The crossing of the potential curves at large internuclear distances resulting in a small transverse momentum which is also measured in the experiment for the population of the asymmetric states.

These data can be compared to helium-ion collisions, where the prominent channel is the population of a symmetric final state, being populated in a two-step transition. In sodium-ion collision, we found the opposite behavior; population of symmetric final states seem to happen in a one step transition. The reverse finding for Na as compared to He collisions is not surprising, since in case of He two equivalent

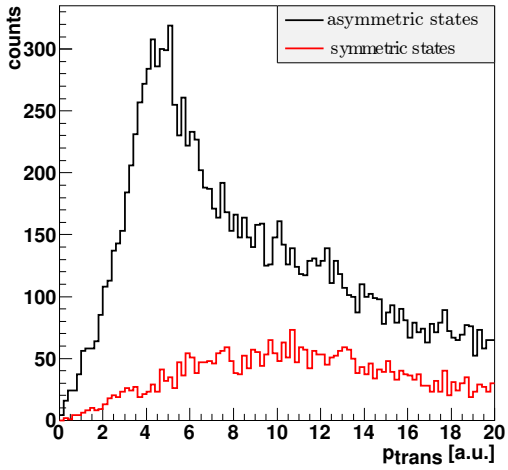

Figure 3.15: Histogram of transverse momentum of recoil ions at low projectile velocities of $v_P = 0.39$ a.u.. Compared to higher projectile velocities (figure 3.11), the transverse momentum component of recoil ions populating symmetric states is larger for smaller projectile energies (red curve), as predicted by the CBM (see figure **??**). The black curve corresponds to electron capture into asymmetric final states of the projectile, which peaks at the same transverse momentum for different projectile energies.

electrons are captured, whereas in Na the initial electrons are starting from different n-shells, which is an asymmetric configuration.

The relative cross sections for the symmetric versus asymmetric states for different projectile velocities is shown are figure 3.16. As discussed in subsection 3.3.2, the data has been corrected for the underestimation of the symmetric channels due to the large transverse momentum. This correction leads to a systematic error which is indicated by the blue points in the graph. The origin of the systematic error is the assumption that the measured transverse distributions are the same in time of flight direction as in y-direction. Due to different cuts for different data sets the systematic error is different for each data set. The energy dependence is striking, at projectile velocities of $v_P = 0.39$ a.u., the symmetric channels are almost as likely to be populated as the asymmetric ones.

In order to compare these results to helium-ion collisions, it needs to be pointed out that since we do not detect the projectile, we cannot distinguish between true double capture and transfer excitation, where the projectile is stabilized through an Auger decay after the collision. Using Auger spectroscopy, it has been reported in the literature that at low collision energies, population into channels involving a dielectronic process during the transfer are dominant [72]. This general behav-

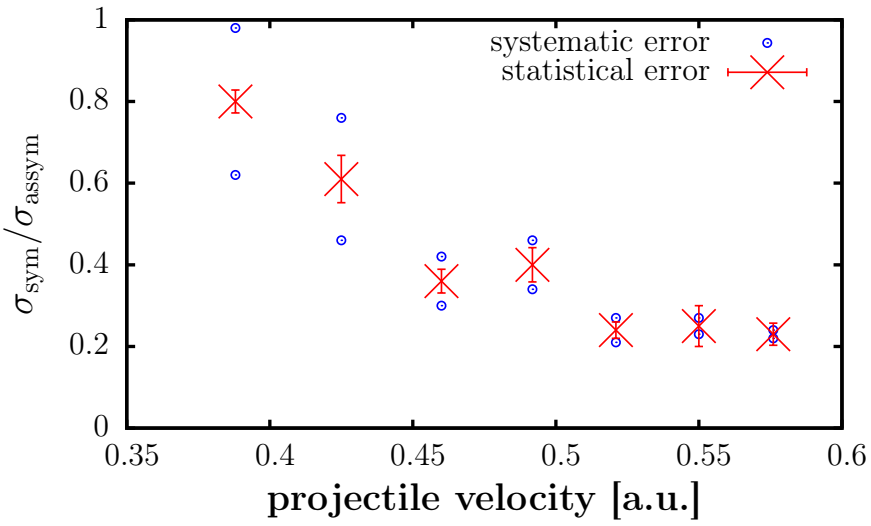

Figure 3.16: Energy dependence of the relative cross sections for the symmetric channels and the asymmetric channel in double charge transfer between O^{6+} + Na(3s). Smaller projectile velocities lead to an increased population of the symmetric states.

ior could be explained by the fact that in collisions with highly charged ions the electron-electron interaction is weak as compared to electron-nucleus interaction (cf. figure 3.13). In a Landau-Zener model the avoided crossings are much larger for monoelectronic transitions than for dielectronic transitions, such that the probability for transitions at strongly avoided crossings becomes weak at low collision energies. On the other hand, using RIMS and separating events leading to true double capture (TDC) from the ones leading to transfer ionization (TI), it has been reported that in case of TDC at higher projectile velocities, population transfer at smaller internuclear distances is more likely [56].

3.3.4 Conclusion

We report on the energy dependence of double charge transfer in ion-alkali collisions. As compared to previous measurements, which investigated the transfer of two equivalent electrons, for the first time transfer of non-equivalent electrons is investigated. Varying the projectile energy from $v_P = 0.39$ a.u. to $v_P = 0.58$ a.u. and thus effectively varying the interaction time the relative cross sections of the population of symmetric ($3s^2$ and $3l3l'$) and asymmetric states have been measured. The smaller the projectile velocity the more likely the symmetric states are populated. This change in symmetry of the electronic state (asymmetric electron configuration

changes to a symmetric one) indicates electron correlation during the transfer which might occur in a one-step process. Using simple Coulomb potential curves, it can be explained that a single step transfer happens at small internuclear distances, leading to large transverse momenta of the recoil ions, as observed in the experiment. Furthermore, for smaller projectile velocities we measure larger transverse momenta of the recoil ions populating the symmetric channels. This trend is also given by the CBM calculations, which also suggests a one-step transfer. These findings are similar to the ones in helium-ion collisions, where, starting from an equivalent electron configuration, the production of nonequivalent electron configurations becomes dominant at low collision energies due to electron-electron interactions [72].

Chapter 4

Experimental setup

This chapter gives an overview of the Heidelberg MOTRIMS setup combining a recoil ion momentum spectrometer (RIMS) [6, 11] with laser cooling and trapping of rubidium atoms in a high density three-dimensional magneto-optical trap (3D MOT) [10], loaded with high flux from a two-dimensional magneto-optical trap (2D MOT) [73, 74]. The main challenge in combining these two fields is to keep high resolution for the spectrometer whilst providing enough optical access for the trapping beams on one hand, and, on the other hand, to avoid distortion of the recoil trajectories by fast switching of the magnetic quadrupole field from the 3D MOT. Furthermore, the setup has to be fully transportable since it will be transported to the HITRAP beamline at GSI in Darmstadt for investigation of multiple-charge transfer between highly charged ions and the trapped ^{85}Rb atoms. The whole setup consists of an optical table for the laser setup and an ultra-high vacuum (UHV) chamber mounted to a 19 inch rack including all necessary electronics. A first generation apparatus has been described in [51]. This apparatus has been upgraded in the current work, in particular a new atom source with a high atomic flux and a new spectrometer with high resolution have been developed.

The next section discusses general aspects of the setup. In section 4.2 the compact laser system used for the 2D as well as the 3D trap is presented. Section 4.3 gives an overview of the vacuum setup and the implementation of the new loading mechanism into the MOTRIMS setup. The details on the atom source (4.4) and the trap are given (4.5). Finally, a detailed description of the RIMS, including simulations on the planned ion-atom collisions, is given in section 4.6.

4.1 General considerations

The goal is to setup a compact and transportable high density atom target for investigation of multiple charge transfer in ion-atom collisions at the HITRAP beamline at GSI in Darmstadt. In order to investigate the charge transfer a high-resolution

recoil-ion-momentum spectrometer, requiring a cold target (see section 2.1.6), will be used. The cold target will be provided by rubidium atoms trapped in a high density magneto-optical trap.

From calculations using the classical over-the-barrier model we estimate the total cross sections for multiple (more than one) electron transfer in collision of rubidium with highly charged ions to be almost two orders of magnitude smaller than in single electron transfer. In order to obtain measurable rates, a dense target with high atom number, high loading flux and no background ions, allowing for high duty cycles, is therefore indispensable. In order to obtain a high density target, the atoms are trapped in a dark spontaneous optical trap (dark SPOT) [18], where densities are one order of magnitude higher than in conventional magneto-optical traps, resulting in an increase in atom number.

Besides these basic physical conditions the main constraint on the experimental setup is the need for a compact and modular design, such that the experiment can easily be transported to GSI and run at the HITRAP facility. Thereby the key parameters were already set by the first generation setup from which the main vacuum chamber and the pumping stage were used in the new design. An overview of the new chamber providing the target is shown in figure 4.1. The whole setup, consisting of a novel atom beam source, an ultracold high density target, the ion detection and the pumping stage is mounted on a mobile rack (see figure 4.1) and has a total size of 1900 mm × 1900 mm × 530 mm. This rack supplies three 19 inch racks for the electronics needed to operate the trap and the spectrometer. The laser system is mounted on a separate laser table and is transported to the experiment using single-mode polarization maintaining fibers.

For loading 3D MOTs with high flux, several techniques are available (Zeeman slower [75, 76], double MOT system [77, 78], LVIS [79]). In order to have a compact and robust setup which can be included in the MOTRIMS setup, we choose to load our target from a 2D MOT [73, 74]. 2D MOTs provide loading fluxes of up to 10^{10}atoms/s. Since the atoms are precooled in a separate chamber, the atom source is decoupled from the collision region and a low background ion rate is ensured. Furthermore, the design of the 2D MOT is compact such that it could be implemented in the current setup. As compared to Zeeman slowers, no magnetic fields, which would distort the trajectory of the recoil ions and thus reduce the resolution of the spectrometer, are present at the collision region. The created beam has a low divergence of 23 mrad and a mean velocity of about 14 m/s, allowing for efficient loading of the 3D trap even if the atom source is at some distance from the trapping region. Furthermore, in COLTRIMS, cold atom beams generated from supersonic expansion are used as a target [3, 80, 5]. The possibility of using the cold atom beam emerging from a 2D MOT will also be investigated for the first time in the

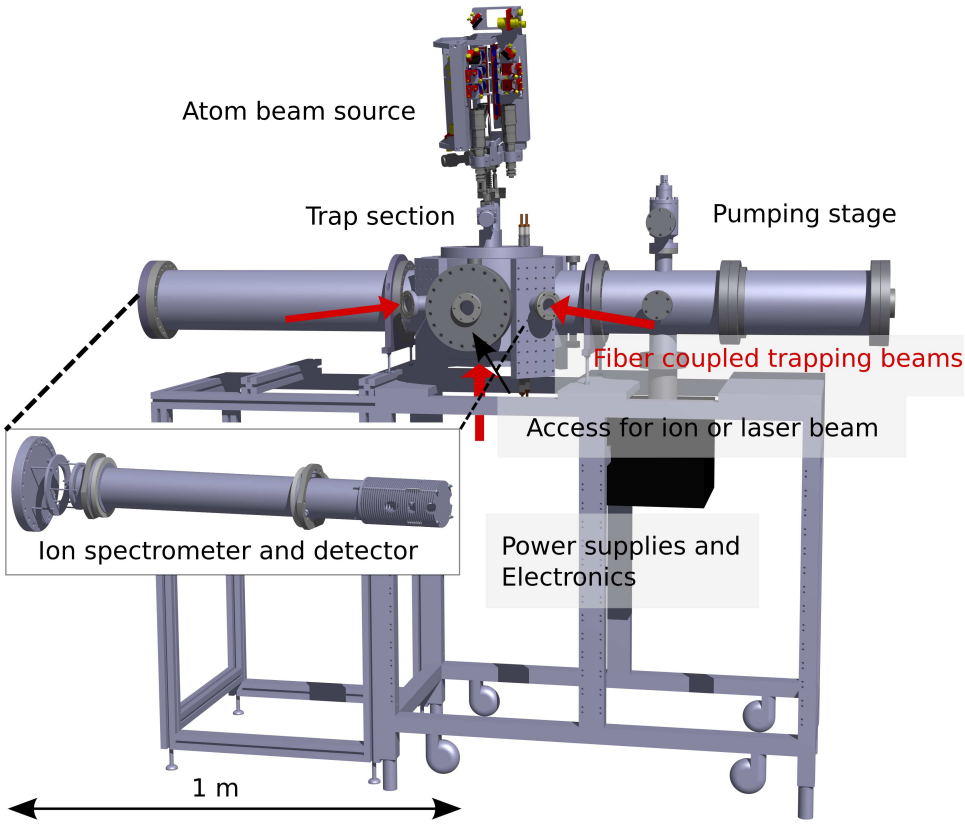

Figure 4.1: Transportable setup. The UHV chamber for the target is compact with a total size of 1900 mm × 1900 mm × 530 mm.

current setup.

In order to trap the atoms in a MOT, a base pressure of $< 10^{-8}$ mbar is needed in the main chamber which is pumped by a combination of an ion getter and a Titanium-Sublimation pump. We achieve a base pressure of 5×10^{-9} mbar in the main chamber. Due to differential pumping in the double-chamber setup, no additional pumping of the atom source chamber is needed, again keeping the setup compact. The main vacuum chamber consists of a stainless steel ultra-high vacuum chamber offering two CF 200 ports, four CF 40 flanges for optical access of the horizontal cooling beams and four CF 150 ports. Two of the CF 150 ports will be used for connection to the beam line at GSI, one for the pumping stage and one for implementation of the recoil ion momentum spectrometer. This means that the vertical cooling beams, absorption imaging, access of a cold atom beam and holders for the quadrupole magnetic field coils all need to be implemented into the last two remaining CF 200 ports.

The target atoms are trapped at the center of the recoil ion momentum spectrometer. Typical resolutions of RIMS are on the order of $\delta \approx 0.05$ a.u. [6, 11], allowing for extraction of spectroscopic information. In order to achieve this resolution, very homogeneous electric fields at the center of the spectrometer are needed. Since the fields inside the spectrometer are weak it is indispensable to shield the inside of the spectrometer from electric stray fields originating from the surrounding ultra-high vacuum chamber, which is on mass. However, in order to combine RIMS with laser cooling and trapping enough optical access needs to be included in the electric field plates. Furthermore, adaption to the current vacuum setup puts a constraint to the outer diameter of the plates. Not only electric stray fields, but also magnetic stray fields reduce the resolution of the spectrometer since the trajectories of the recoil ions will be distorted. Therefore, fast switching of the magnetic quadrupole trapping field of the MOT is implemented, with switching time on the order of 100 μs. This is achieved best when the magnetic field coils are placed inside the vacuum, allowing low currents to generate the needed high magnetic fields and reducing magnetic stray fields due to eddy currents in the steel chamber. Since high magnetic field gradients should be available for a compressed MOT [48] and due to the minimum distance between the pair of coils given by the spectrometer plates, the coils need to be water-cooled.

Making the trap operable at GSI, where the laser room is located on another floor than the beamline, the laser system is mounted in a compact way on a mobile laser table with a total size of $75 \times 150\,\mathrm{cm}^2$. The laser system consists of two separate frequency-stabilized lasers due to the large hyperfine splitting in ^{85}Rb of 3 GHz of the ground state. Due to space constraints on the laser table, the spectroscopy for frequency stabilization is mounted on a separate breadboard with a total size of

$60 \times 40\,\mathrm{cm}^2$. For simultaneous operation of the 2D and 3D MOT, enough cooling laser power is needed to saturate the cooling transition in all beams ($P_{min} = 70$ mW behind the fibers and AOMs), while keeping the setup compact. The beams used for cooling and trapping all need to be shifted in their frequencies independently. This is done using AOMs, which also serve to control the intensity of each beam and can, if coupled into optical fibers afterwards, be used as shutters. For compact splitting and combination of the beams fiber ports cluster [81] are used.

4.2 Trapping laser system

As a target for highly charged ions we use a dense cloud of ultracold rubidium ions. Operation of a MOT demands frequency stabilization of the lasers to the atomic transition used for cooling. The target atoms are trapped in a 3D MOT, loaded from a 2D MOT. Therefore, 8 laser beams with different frequencies are needed. In order to optimize the frequency of each beam and switch them independently, each of the beams passes an acousto-optic modulator (AOM). Furthermore, the trap will be operated at the HITRAP beamline, at GSI Darmstadt. The laser room for the laser systems for the beamline is one floor away from the beamline, such that a separate laser table is needed, where the light is produced, stabilized and manipulated. Transportation to the experiment is done in single-mode polarization maintaining fibers.

^{85}Rb can be trapped in a magneto-optical trap rather easily since there is a closed cooling transition from the ground state. It has a nuclear spin of $I = 5/2$. Due to hyperfine coupling, the ground state $5^2S_{1/2}$ splits up into two sub-states $F = \{2, 3\}$, the excited state $5^2P_{3/2}$ splits up into four substates $F = \{1, 2, 3, 4\}$. The energy splittings of the hyperfine substates of the D_2 line $5^2S_{1/2} \rightarrow 5^2P_{3/2}$ used for cooling of the rubidium atoms are shown in figure 4.2.

The cooling laser drives the $F = 3 \rightarrow F' = 4$ closed cooling transition, but since the energy splitting of the $F' = 3$ and $F' = 4$ sub-states is only 121 MHz, about 0.1 % of the atoms are excited non-resonantly into the $F' = 3$ state. From there they can decay spontaneously into the $F = 2$ ground state which is a dark state for the cooling light. Due to the large hyperfine splitting of 3 GHz of the ground state two different lasers are needed for cooling and trapping. An additional repumping beam driving the $F = 2 \rightarrow F' = 3$ transition pumps the atoms back into the cooling cycle.

In total, this setup, including 2D MOT, dark spontaneous optical trap (SPOT) [18] and absorption imaging requires multiple beams at different frequencies:

- For cooling and trapping in the 2D MOT we need cooling light that is red-

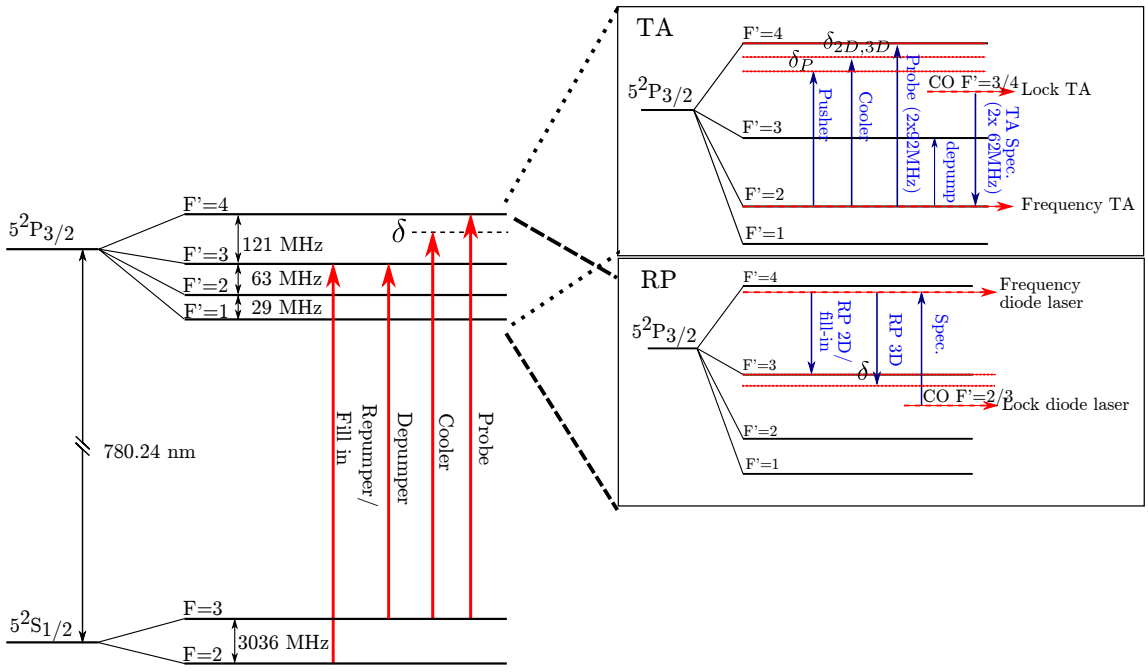

Figure 4.2: Hyperfine level scheme of the D_2 line of ^{85}Rb. The cooling beams are red-detuned from the $F = 3 \rightarrow F' = 4$ transition, while the repumping beams are running on resonance of the $F = 2 \rightarrow F' = 3$ transition. A resonant probe beam is used for absorption imaging. The upper inset shows the stabilization scheme for the TA laser, the lower inset shows the stabilization scheme of the RP laser.

detuned by $\delta_{2D} \approx -2\,\Gamma$, $\Gamma/2\pi = 6.06\,\text{MHz}$ being the natural linewidth, from the $F = 3 \rightarrow F' = 4$ cooling transition and repumping light resonant with the $F = 2 \rightarrow F' = 3$ transition.

- For extraction of the atoms from the 2D MOT an additional push beam is needed, with the possibility to be red-detuned by several linewidth.

- For trapping in the 3D MOT we need cooling light that is red detuned by $\delta_{3D} \approx -1 - 3\,\Gamma$ from the $F = 3 \rightarrow F' = 4$ cooling transition and repumping light on resonance with the $F = 2 \rightarrow F' = 3$ transition.

- For operation of the 3D trap in a dark SPOT configuration, an additional depumping beam is needed, which pumps the atoms actively from $F = 3 \rightarrow F' = 3$, from where they decay into the absolute ground state as well as a fill-in beam ($F = 2 \rightarrow F' = 3$) which pumps the atoms back into the cooling cycle.

The details of the two laser systems will be presented in the following.

4.2.1 Cooling laser system

For simultaneous operation of the 2D and 3D trap, the cooling laser system should provide enough power to saturate the D2 transition ($I_{sat} = 1.6\,\mathrm{mW/cm^2}$ for closed transition) whilst being compact. The Toptica TA Pro is based on an external-cavity diode laser (ECDL) [82] coupled into a tapered amplifier chip. The beam is amplified in a single pass through the chip preserving the spectral properties of the beam and then coupled into a single mode fiber. We use the fiber in order to get mode cleaning after the TA chip and thus high efficiencies in the subsequent beam path, including coupling into AOMs and fibers. The tapered amplifier chip makes it possible to reach output powers up to 1.3 W (730 mW after the fiber). In order to protect the diode laser from retro-reflected light a 60 dB optical isolator is placed between the DL Pro and the TA chip. Between the isolator and the tapered amplifier a test beam is split off which is used for the spectroscopy to stabilize the laser frequency.

The lasers are stabilized using FM spectroscopy [83]. The spectroscopy setup is on a separate breadboard placed under the optical table on a Sorbothane sheet to damp vibrations. The test beam is transported to the spectroscopy in a single-mode polarization-maintaining fiber. On the spectroscopy board (figure 4.3), the beam first passes an AOM (Crystal Technology 3000 Series) in a double-pass configuration and shifts the laser frequency by 2×62MHz. Afterwards the beam is split up, one part passes an $1:3$ telescope and is send through a Rubidium vapor cell to be used for Doppler-free saturation spectroscopy. The other part is coupled into a Fabry-Perot interferometer to monitor single-mode operation of the laser. The laser is locked on the $F' = 3/4$ crossover which provides the largest signal. Due to the AOM the laser is actually running on the $F = 3 \rightarrow F' = 2$ transition (figure 4.2). This locking scheme was chosen so that all necessary frequencies can be generated by one laser system with commercially available AOMs.

On the optical table (figure 4.4), the cooling beam is split up into the depumping, probe, pushing and the two cooling beams by polarizing beam splitters (PBS) in combination with half-wave plates. On the first PBS a small amount of the light is split off for the depumper and passes a single-pass AOM. The first order (shifted by 63 MHz) of the depumper is coupled into a fiber. The zeroth order is recycled and, after passing an AOM in double-pass configuration, is used for the absorption beam. The use of a double-pass AOM here has the advantage that, depending on the density of the cloud that will be imaged, the frequency can be detuned without recoupling the fiber, avoiding optical thickness during imaging.

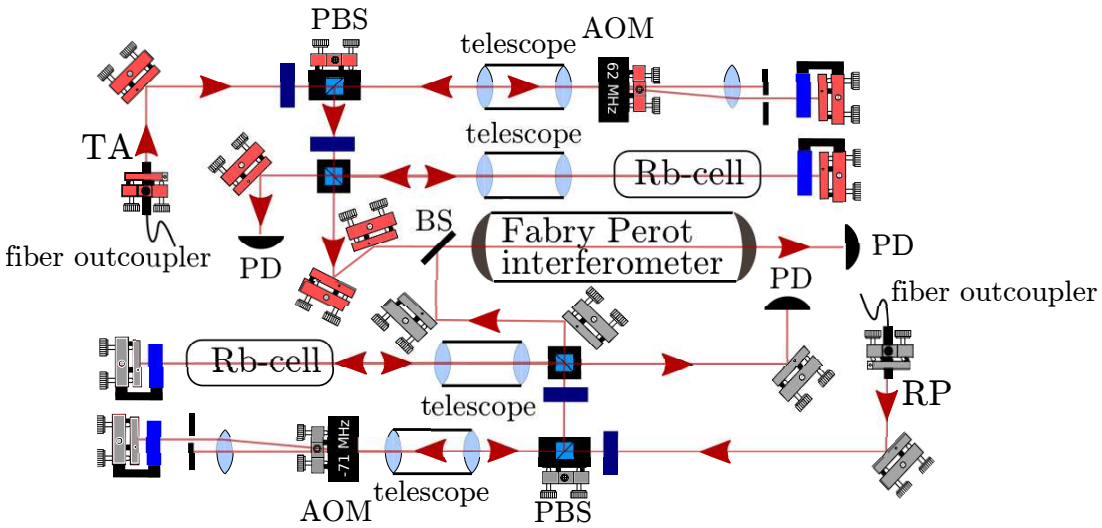

Figure 4.3: Doppler-free spectroscopy for laser lock. Both laser systems are locked using Doppler-free spectroscopy. Light from the table is transported using polarization-maintaining single-mode fibers. The locking point of each laser can be shifted using double-pass AOMs. A Fabry-Perot resonator is used for monitoring single-mode operation.

Most of the light from the TA is split off further downstream into the cooling beams for the 2D and 3D MOTs and the push beam for the 2D MOT. All three beams can be shifted in frequency by double-pass AOMs, allowing to optimize the detuning without readjusting the fiber coupling. Another advantage of the double-pass in cat-eye configuration [84] is that when the AOM is switched off the zeroth order is blocked by the iris placed between the AOM and the retroreflecting mirror. This configuration can therefore also be used to switch the beams without installing any further mechanical shutters that cause vibrations on the table[1].

4.2.2 Repumping laser

The repumping light is generated by a homebuilt external-cavity diode laser in Littrow configuration [82] driven by the MOGbox DLC-202 laser diode controller from MOGlabs [85]. For a detailed description of the diode laser setup see [51]. The laser beam passes an optical isolator to protect the diode laser from back reflections. Then a small fraction of the light is split off and sent to the spectroscopy board using a fiber. This setup is identical to the one of the cooling laser (see figure 4.3). In

[1] When loading into an optical dipole trap additional mechanical shutters are needed to suppress the light

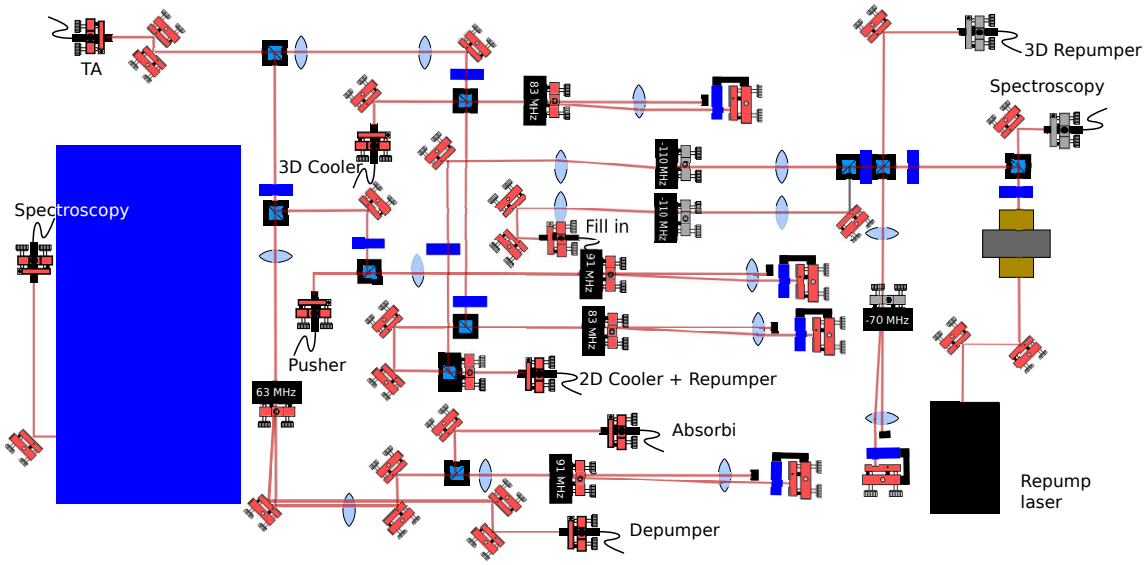

Figure 4.4: Scheme of the laser table. Laser light is produced by a commercial TA and an ECDL diode laser for cooling and repumping. The beams are split up by PBS and each beam can be shifted in frequency by AOMs separately before being coupled into the fibers.

order to generate all frequencies needed with AOMs, we shift the repump frequency using an AOM in double-pass configuration (shifting the beam by $2 \times -71\,\mathrm{MHz}$) prior to the actual spectroscopy where it is locked on the $F' = 2/3$ crossover (see figure 4.2).

On the optical table, the beam is split up into three beams. The repumping beam for the 2D MOT and the fill-in beam are shifted by $-110\,\mathrm{MHz}$ by AOMs in single-pass configuration to be on resonance to the $F = 2 \rightarrow F' = 3$ transition. The repumping beam for the 2D MOT is subsequently superimposed with the cooling light for the 2D MOT prior to coupling into the same polarization-maintaining fiber. The repumping beam for the 3D MOT passes an AOM in double-pass configuration such that the frequency can be optimized during the experiment.

4.2.3 Fiber Port Clusters

All laser beams are coupled into single-mode polarization maintaining fibers on the optical table. Before outcoupling at the experiment, the beams are sent through so-called laser cubes [81]. These are fiber based cubes from Schäfter+Kirchhoff including compact polarization optics. In these cubes the light can be split up or superimposed as desired. The main advantage of them, next to being very compact

and robust, is that on the table itself only one fiber needs to be coupled. For our setup we have three cubes: two cubes only consisting of a half-wave plates plate and a PBS which are used to split the repumping light of the 3D trap as well as the cooling and repumping light of the 2D trap into two output beams. Another more elaborate cube is used to provide the beams for the 3D trap (see figure 4.5). The cooling beam is split into three beams inside the cube. A second input is used to overlap the absorption beam with the vertical cooling beam (z'), whereas the fill in beam is superimposed with the horizontal cooling beams (H1 and H2). At the output of the cubes, the light is coupled again into polarization maintaining fibers, each of 15 m length, and transported to the UHV chamber, which is described in detail in the next section.

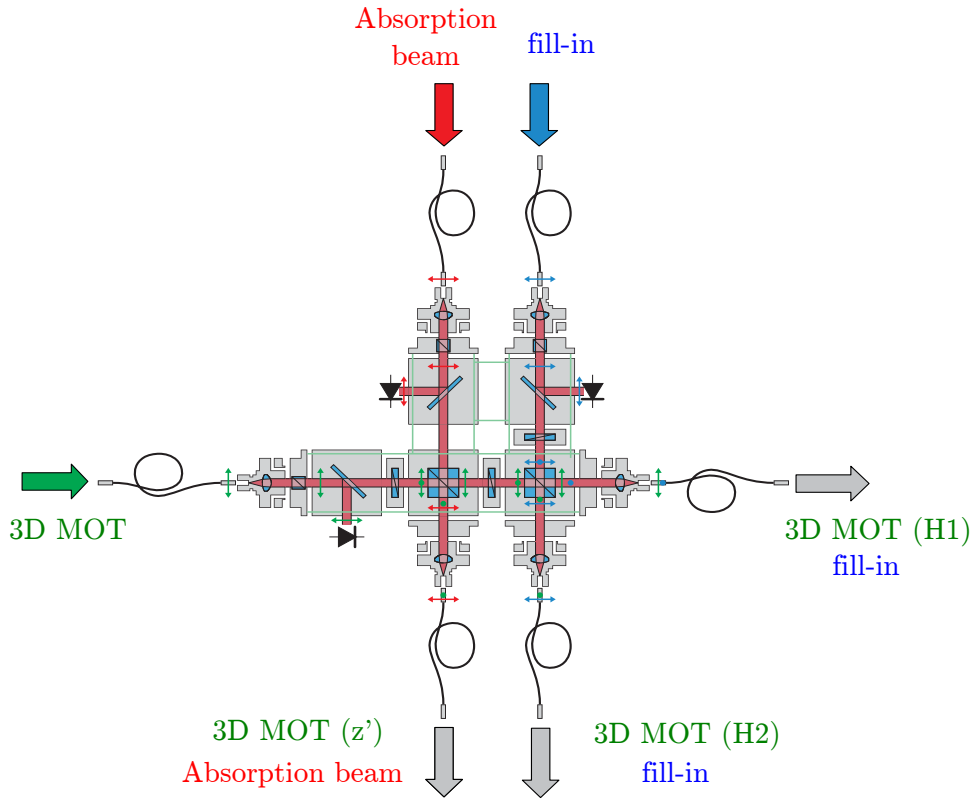

Figure 4.5: Fiber Port Clusters for the 3D trap. The laser cube is used to split up the 3 cooling lasers for the 3D trap. On the z' axis the absorption beam is superimposed, whereas on the H1 and H2 axis the fill-in beam is overlapped. Drawing adapted from [81].

4.3 Vacuum system

The center of the setup is the vacuum chamber (see Figure 4.1). It merges the atom beam source with the atom target, which is located at the center of the recoil ion momentum spectrometer. The main chamber and pumping stage had been designed in a first generation experiment [51], such that an elegant way had to be found to include the 2D MOT, the new magnetic field coils, allowing for fast switching, and the spectrometer in that chamber. The details will be described in the following.

In the main chamber, UHV condition are provided by two pumping systems: A titanium sublimation pump (Ti:Sub) for pumping H_2, N_2 and water combined with a cryo shield by Varian (TSP Cryopanel) which can be flushed with cooling water or liquid nitrogen to increase the pumping speed. Rare gases are mainly pumped by an ion getter pump (Varian Star Cell 55). Without baking we achieve a base pressure of 5×10^{-9} mbar, measured with a vacuum ion gauge (Pfeiffer IKR 270).

The atom source is located in a separate glass cell. The connection between the two chambers is done through one single piece (see figure 4.6) made out of stainless steel. This piece includes a differential pumping hole of 800 μm diameter, which also serves as the exit hole for the atom beam. With this differential pumping, a maximum pressure ratio of 10^{-3} between the two chamber can be achieved without any additional pumping of the glass cell. On the low pressure side the glass cell is attached to a CF 40 flange, whereas the high-vacuum side only requires a CF 16 flange, so that the connection to the experiments is as compact as possible. A bellow including three threaded rods for fine adjustment of the direction of the atomic beam ensures optimal overlap with the cooling region.

For implementation of the 2D MOT into the MOTRIMS setup several geometrical constraints are given; the main chamber only offers two CF 200 ports, where the vertical cooling beam, the absorption imaging and the access for the atom beam must be included. Another constraint is given by the limited optical access available in the spectrometer, where we want to include the atom beam without any further holes than necessary for the cooling and projectile beams. This can be solved by including a CF 16 flange for connection of the 2D MOT into the top CF 200 flange, leaving enough space for the vertical cooling beam, which is coupled into the chamber through a CF 40 viewport. The CAD drawing of the flange is shown in figure 4.7. The atom beam thus forms a small angle of 12 ° with the vertical cooling beam.

A CF 16 valve is placed between the two chamber. This is only a precautionary measure for transportation of the target to the GSI, where a risk of breaking the glass cell exists. Another advantage of the valve is that the 2D MOT setup remains modular and could be tested prior to implementation into the MOTRIMS setup. Furthermore the main chamber can be opened without breaking the vacuum in the

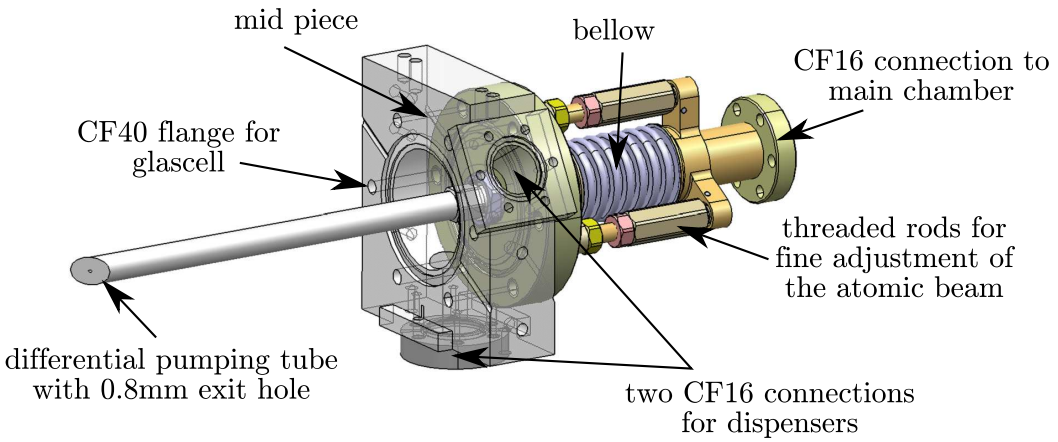

Figure 4.6: Center piece of the 2D MOT setup. The center piece connects the 2D MOT to the main chamber through a differential pumping hole. It also holds all the different components of the 2D MOT [86].

glass cell which would require replacement of the dispenser.

4.4 Cold atom beam source

The objective is to load a 3D MOT with high flux and no background ions. For investigation of multiple charge transfer between ultracold atoms and highly charged ions loading from a two-dimensional magneto-optical trap has several advantages: the high loading flux allows short loading times of the 3D trap and thus a high duty cycle. In particular for experiments where rare events are detected, which might be masked by more likely events like single-charge transfer and lead to the loss of a high number of the trapped atoms, fast loading is important. The background ion rate should also be kept low, ensured by the double-chamber setup, decoupling the atom source from the collision region.

In the following the most important features of the 2D MOT setup will be presented. For a more detailed review please refer to [86]. The compact setup of the 2D MOT has a total size of $20 \times 20 \times 40\,\mathrm{cm}$ and is shown in figure 4.8. Requiring only one CF 16 flange to connect the setup to the main chamber it is very modular and has been implemented successfully in two different setups in our group (MOTRIMS and Rydberg setup). It consists of a glass cell, which is filled with rubidium vapor from organ shaped dispensers (Altechna), allowing for optimal optical access, surrounded by a metal cage holding all the optics. The quadrupole magnetic field is generated by permanent magnets [87], such that the design stays compact since

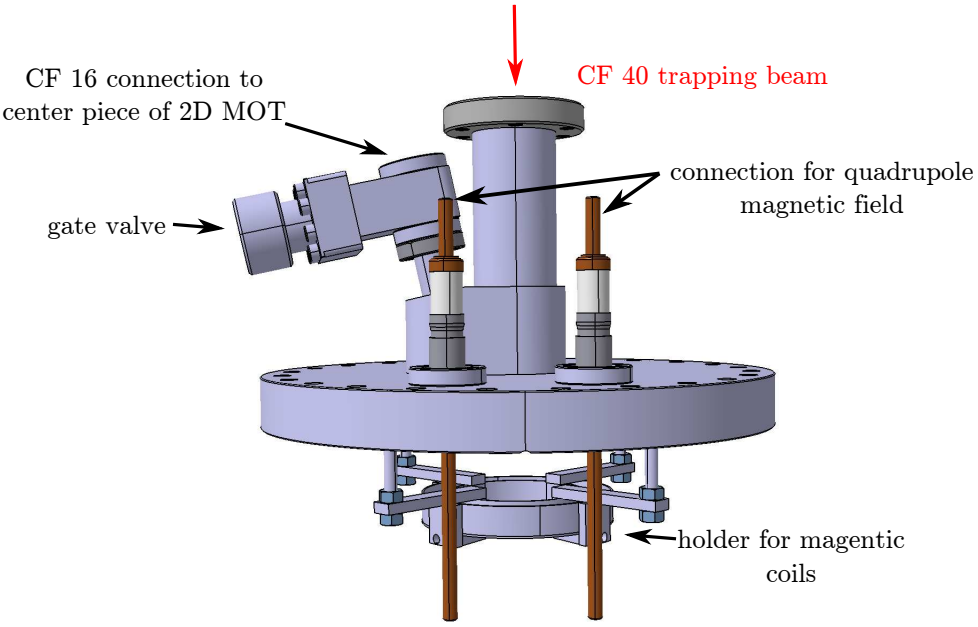

Figure 4.7: CF 200 top flange connecting the 2D MOT to the main chamber. The trapping laser enters the chamber through a CF 40 viewport. The 2D MOT is connected to the main chamber via a CF 16 gate valve forming an angle of 12 ° with respect to the vertical cooling beam. The flange also provides two CF 16 feedthroughs for cooling and electrical contact of the coils generating the quadrupole magnetic field and holds the magnetic coil holders.

extra power supplies and electrical connections for coils are needed. The only connections needed for operation of the atom source are three optical fibers for cooling and pushing the atoms towards the main chamber and electrical connections for the dispensers as well as for the compensation coils for the earth magnetic field. The center piece connecting the 2D MOT to the main chamber (see figure 4.6) further includes two CF 16 feedthroughs for the electric connection of the dispensers and threaded holes so that the optics cage can be attached to it.

The light for the 2D MOT is transported from the optical table using polarization maintaining fibers. Compact outcouplers from Schäfter und Kirchhoff [81], fixed to the mid piece, produce elliptical beams with $1/e^2$ diameter of 22 mm on the long axis and 11 mm on the short axis. The elliptical beam shape is chosen to ensure saturation of the cooling transition all over the cooling region and to have

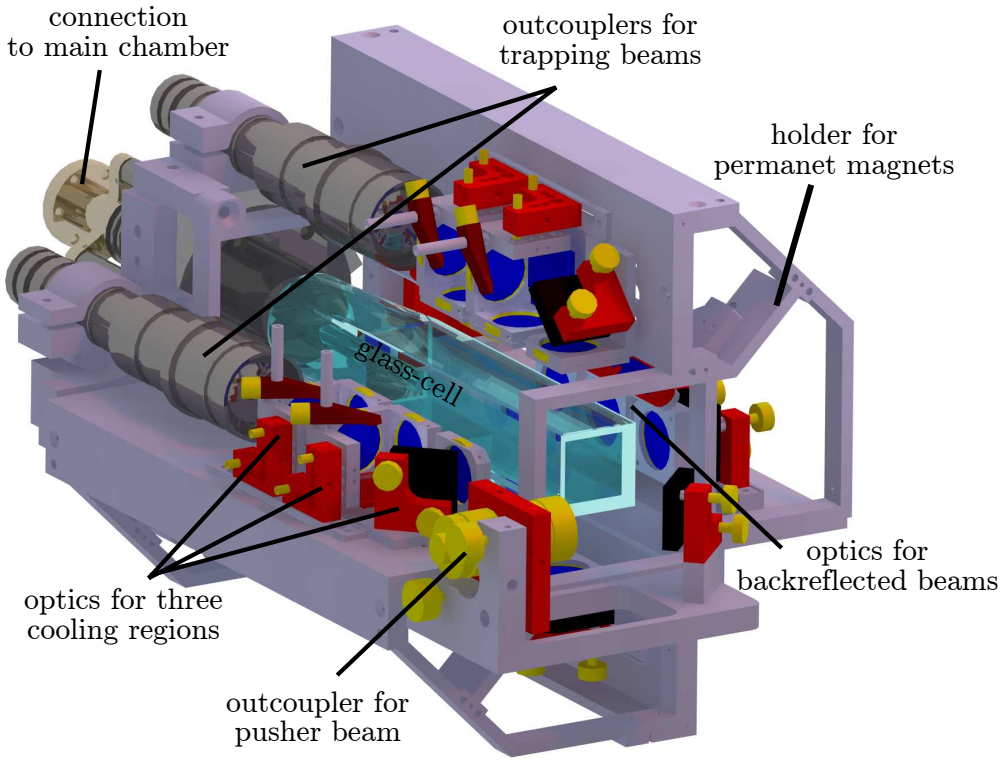

Figure 4.8: Design of the 2D MOT. A cage holding all the optics and the permanent magnets is surrounding the glass cell which is filled with rubidium gas. Taken from [86].

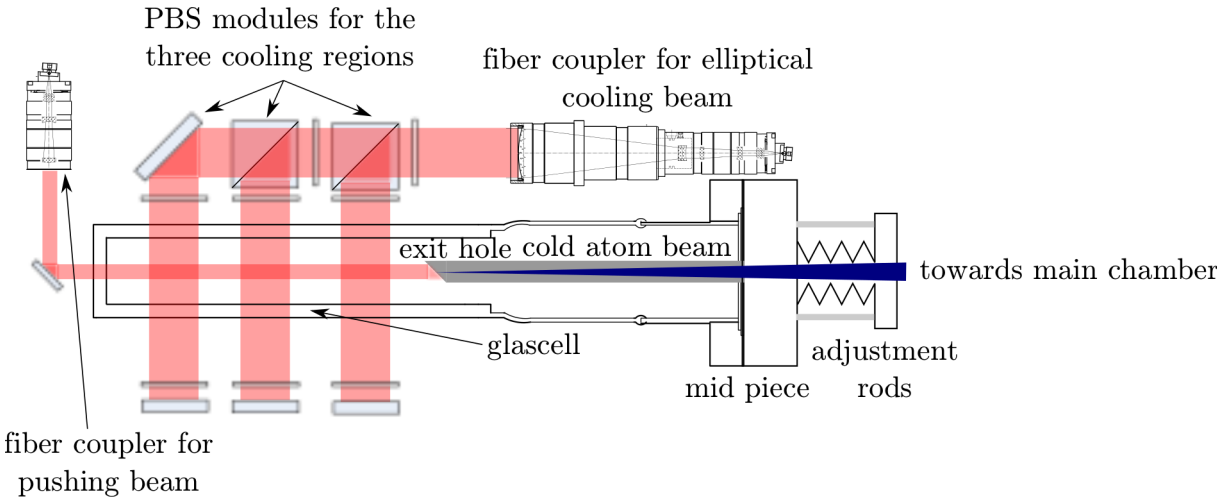

Figure 4.9: Optics module of the 2D MOT (top view). After outcoupling of the cooling beams, they are split up into three beams and retroreflected after passing the glass cell. The pushing beam pushes the atoms out of the cooling region towards the trapping region of the 3D trap.

a long cooling region (the atom flux scales with the length of the cooling region [88, 89]). Both beams than split up into three beams by polarization optics (see figure 4.9), leading to a total cooling length of 66 mm. Before passing the glass cell each beam passes a quarter-wave plate to achieve circular polarization needed for trapping of the rubidium atoms. All optics is placed as close as possible in order to ensure good coupling between the cooling regions. This is done by placing the PBS on 0.5 inch mirror mounts and attaching the half-wave plates plates and the quarter-wave plates on the same mirror mount (see figure 4.10). The power distribution in the cooling beams can be adjusted using the half-wave plates plates. After passing the rubidium cell and another quarter-wave plate the cooling beams are retroreflected. The required quadrupole magnetic field for trapping is generated by 5 permanent magnets, which are also attached to the cage holding the optics. The magnets are aligned such that the zero magnetic field line is homogeneous. They can be positioned at five different positions leading to five different magnetic field gradients. In our case we measured the best atom flux for a magnetic field gradient of 15 G/cm.

We characterized the atom beam generated in the 2D MOT prior to implementation in the MOTRIMS setup. From these measurements we could deduce a flux of 3.5 $\times 10^9$ atoms/s with a mean velocity of 14 m/s [86]. Typical atom-flux distributions are shown in figure 4.11, where the dependence on the detuning of the

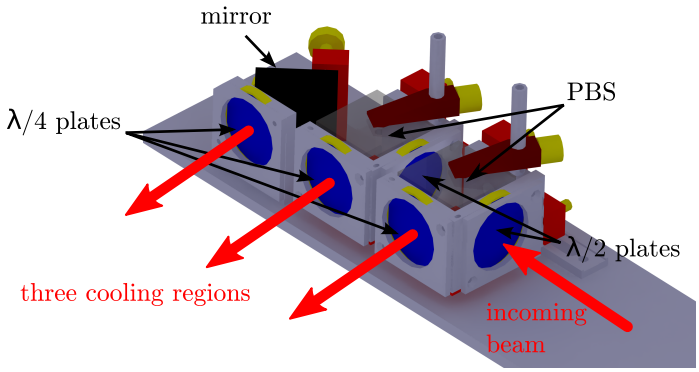

Figure 4.10: Splitting of the trapping beams. These compact optics modules are used to split up the beam for the three cooling regions and to polarize all beams circularly. Taken from [86].

pushing beam is shown. The total flux of the atoms depends crucially on the detuning and power of the pushing beam as well as the power in the cooling beams. The divergence of the beam has been determined to be only 26 mrad, so that, despite the large distance between the atom source and the 3D trap of 48 cm, all atoms can be trapped in the cooling region of the 3D trap. For simultaneous operation of the two-and three dimensional traps typical laser power for the 2D MOT are $P_{Cooler} = 47\,mW$ per beam, $P_{rep} = 8.4\,mW$ and only $P_{pusher} = 600\,\mu W$.

4.5 Target magneto-optical trap

The precooled atoms from the 2D MOT are trapped in a 3D trap inside the recoil ion momentum spectrometer at the center of the main chamber, where they serve as a target for ion/laser beams. As discussed before, one major challenge in combining RIMS with laser cooling and trapping is the fast switching of the magnetic quadrupole field. The details of this will be discussed in the following section.

4.5.1 Magnetic quadrupole field

The magnetic field coils for the MOTRIMS setup have several specifications that need to be fulfilled: In order to have the possibility to compress the MOT, magnetic field gradients up to 60 G/cm should be possible [48]. Due to distortion of the recoil ion momentum trajectories due to changing magnetic field gradients, the switching of the magnetic fields should be fast. Thus the inductance of the coils should be kept

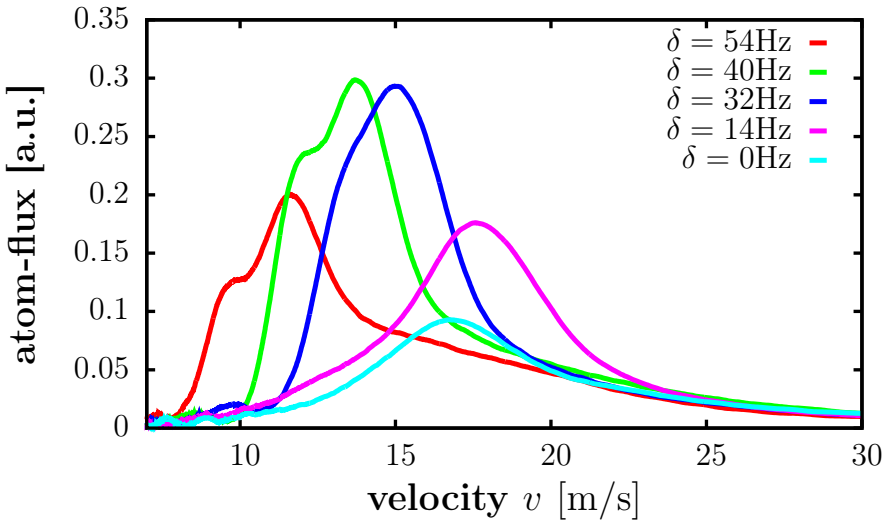

Figure 4.11: Velocity distribution for different detunings of the pusher. Higher pusher detunings shifts the velocity of the atom beam to lower velocities. Taken from [86].

low since the switching time τ of the coils scales with the inductance L. Because $L \propto n^2$, where n is the number of windings, a small number of windings is needed. Furthermore, placing the magnetic fields inside the vacuum and thus lower needed currents reduces the eddy currents induced in the steel chamber, which prolong the switching times.

In order to achieve high magnetic field on the order of 60 G/cm with coils consisting of only few windings high currents up to I =100 A are needed. The power $P = R \times I^2$, R being the resistance of the coil, that needs to be dissipated is up to 330 W, making water cooling of the coils indispensable. This is achieved by using one single hollow copper tube with 2 mm inner and 3 mm outer diameter and 4 m length [35]. Electrical insulation between the windings is done by wrapping a Kapton HN foil with 75 μm thickness around the copper tubes prior to winding the coils. Vacuum connection is done using high power feedthroughs from Vacom (W-HC8-CE-CU64), which consist of hollow copper tube electrically insulated from the flange. The copper tubes used as coils are stuck through the feedthroughs. In order to prevent, in case of a leak, water leaking into the vacuum, the coils are hard soldered to the feedthroughs on the vacuum side. Thus, in case of a leak, 'only' a leak to the atmosphere will appear.

The coils are mounted in anti-Helmholtz configuration with a distance of 120 mm between each other and an inner radius of 35 mm, consisting of 3 radial and 4 axial windings each. They are held in place by magnetic coil holders, which are screwed

into the CF 200 flanges (see figure 4.7). In this configuration, a current of 1 A produces an axial magnetic field gradient of 0.567 G/cm. The resistance of both coils in series is 0.0325 Ω. At typical operation of the MOT, 30 A are applied to the coils, producing a magnetic field gradient of 17 G/cm. Switching times of the current on the order of 100 μs are achieved, however the eddy currents induced in the chamber vanish only after 1.2 ms. Therefore higher currents lead to longer times until the residual magnetic fields have vanished.

4.5.2 Target atoms trapped in a bright MOT

As we saw in section 4.2, the light is guided to the chamber using optical fibers. A major contribution to the compactness of the setup arises from the use of concise optics assemblies which couple the trapping and repumping beams into the chamber. For the operation of the trap as a bright MOT, the repumping and cooling beams are transported to the chamber in the same fibers, having opposite polarizations (see figure 4.5). A compact design from Schäfter and Kirchhoff [81], including fiber outcoulpers, quarter-wave plates and lens, are used to expand the beams to a $1/e^2$ diameter of 20 mm and polarizing the horizontal cooling beams circularly. After passing the chamber the horizontal beams pass another quarter-wave plate and are retroreflected. The vertical beam is also outcoupled using a compact fiber outcoupler. Since the cooling and absorption beam are directed into the chamber with an additional mirror, the quarter-wave plate is placed behind the mirror. After passing the chamber, both beams pass another quarter-wave plate and are subsequently separated using a polarizing film from 3M [90]. Depending on the polarization of the incoming light, this film either reflects or transmits the light. The film is glued on the first lens of the absorption imaging setup and is oriented such that a maximum of the cooling light is reflected (see figure 4.12).

Diagnostics of the trap is done using standard absorption imaging. The optics assembly for the absorption imaging is mounted in a 60 mm cage system from Thorlabs. It consist of a lens $L1$ having a focal length of $f_1 = 200$ mm and a second lens $L2$ with $f_2 = 100$ mm, leading to a reduction of the image of the cloud by a factor of two. The achieved resolution of this system is 72 μm with a depth of focus of 81 μm. More details on this setup are given in the bachelor thesis of D. Gerbert [91].

In the setup, we have a total cooling power of 80.4 mW after the fibers, resulting in a total light intensity of 25.6 mW/cm^2 at the trap center. Detuning the cooling laser by $\delta = 9.2$ MHz and assuming a resonant saturation intensity for rubidium of $I_{Sat} = 1.6$mW/cm^2 [2], leads to a saturation parameter of the trapping transition of

[2] Theorerical saturation intensity for a pure two-level system.

[92]

$$S = \frac{S_0}{1 + 4\delta^2/\Gamma^2} = 1.5, \tag{4.1}$$

where $S_0 = I/I_{Sat}$. This leads to a population in the excited state $F' = 4$ state of

$$\rho_{22} = \frac{S}{2(1+S)} = 0.3. \tag{4.2}$$

In order to reduce losses due to population in the excited state [18], a dark SPOT is implemented in the current setup and will be discussed in more detail in the following section.

4.5.3 Density increase in the dark SPOT configuration

In standard MOTs the density is limited to 10^{10} atoms/cm^{-3} due to scattering and reabsorption of the trap light by atoms, resulting in an outward directed force on the atoms which counteracts the compressive magneto-optical force [47, 48, 49]. Minimizing this rescattering and thus the repulsive forces between the atoms by transferring most of the population in the lowest hyperfine state, which is a dark state for the light, leads to an increase in density of typically one order of magnitude and is the concept of a dark spontaneous force optical trap (dark SPOT) [18]. The underlying mechanism was briefly discussed on the basis of the discussion on the different regimes in a MOT in subsection 2.2.2, a detailed analysis can be found in Townsend *et al.* [47].

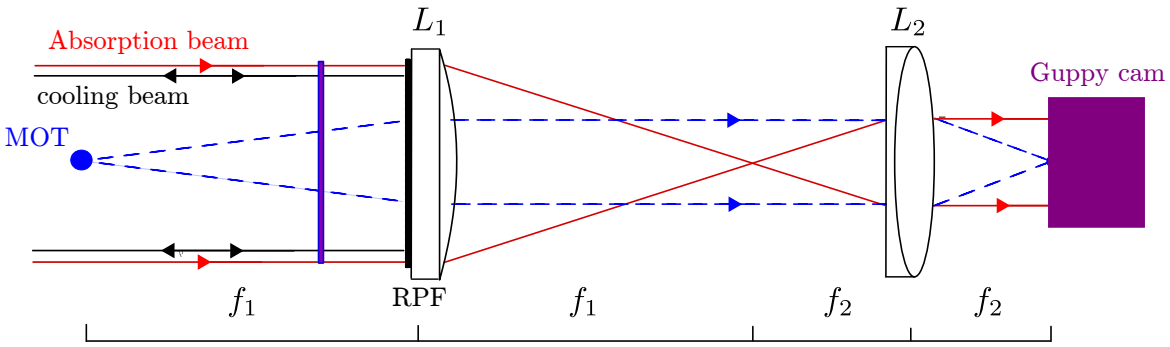

Figure 4.12: Optics assembly in the vertical direction. The cooling beam is separated from the absorption beam after passing a quarter-wave plate using a reflective polarizing film. The cooling beam is retroreflected while the absorption beam passes the imaging optics, casting a shadow of the cloud on the CCD camera (Guppy F-038B).

Experimentally, only the repumping light is blocked at the center of the trap, where the density is highest. Atoms in this region fall into the absolute ground state $5^2S_{1/2}(F = 2)$, which is a dark state for the cooling light (see figure 4.2). An additional depump beam can actively pump the atoms in the dark state. The distribution among the hyperfine ground states is then by the re- and depumping rates (R_{rep} and R_{dep}) between the two states:

$$\frac{N_u}{N_d} = \frac{R_{rep}}{R_{dep}} = \frac{\tau_u}{\tau_d}; \tag{4.3}$$

where $N_{u/d}$ is the number of atoms in the upper and the lower hyperfine ground state respectively. The time constants $\tau_{u/d}$ characterize the dwell times for an atom in one of the two states. A dark SPOT can be characterized by how 'dark' the trap is, which is done in literature by introducing the parameter p, represents the fraction of atoms in the upper F=3 hyperfine state which participate in the trapping cycle:

$$p = \frac{N_u}{N_d + N_u}. \tag{4.4}$$

In analogy to a standard MOT, in a dark SPOT, one can distinguish between a temperature limited and a density limited regime [47]. In the range of small upper state populations, which can be assumed being the case for small depumping intensities, p is well approximated by $p \approx \tau_u/\tau_d$.

In order to realize the dark SPOT in the experiment, a hollow repumping beam is overlapped with the horizontal cooling beams[3]. The hollow beams are produced by physically blocking the beams in their center using a piece of a floppy drive[4] with a diameter of 6 mm. In order to avoid diffraction at the edges, these spots are imaged onto the center of the trap. The optical system for beam collimation and spot imaging has been setup following [51] and is shown in figure 4.13. The beam expands freely after outcoupling of the fiber and before collimation through the lens $L1$. The dark SPOT is imaged onto the trap by the lens $L2$. From the boundary values defined by the setup, namely α (numerical aperture of the fiber), B (image of the dark SPOT) and w (waist of the repumping beam), the remaining parameters can be calculated from the relations

$$\tan(\alpha) = \frac{a}{b} \qquad \tan(\beta) = \frac{a}{c} = \frac{w}{2f_2} \qquad \beta = \alpha(b/f_1 - 1). \tag{4.5}$$

[3]Note that no repumping beam is present in the z'-direction.

[4]After extended investigation of different material which can be used to block light, the inside of a floppy drive turned out to be best suited for our needs (see also the diploma thesis of C. Glück [93]).

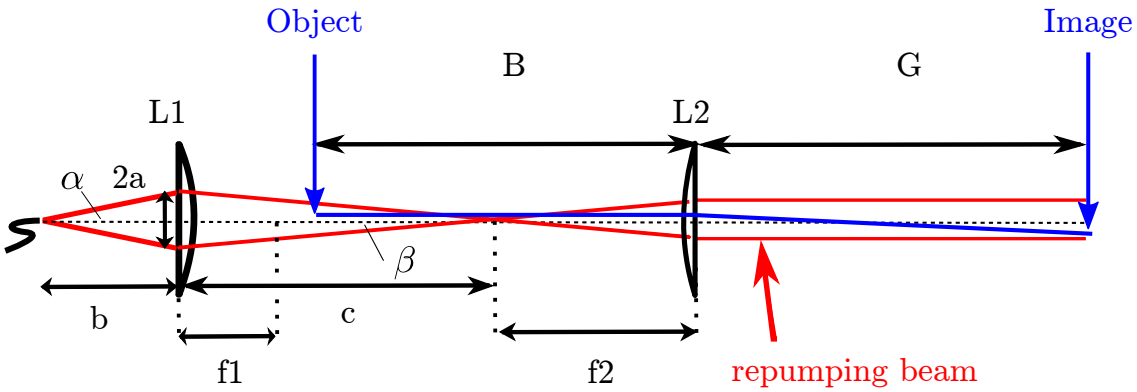

Figure 4.13: Optics assembly for the repump beams used for the dark SPOT. To avoid diffraction the spot is imaged onto the center of the trap in the horizontal plane.

For a 1:1 imaging with $B = 400\,\text{mm}$, $f_2 = 175\,\text{mm}$ and $w = 20\,\text{mm}$ we derive $f_1 = 100\,\text{mm}$, $b = 141.7\,\text{mm}$ and $c = 337.7\,\text{mm}$. The imaging of the dark spot at the position of the trap has been measured with a CCD camera beam profiler[5] and its profile along the x-direction is shown in figure 4.14. At the center of the trap an extinction of 1:1000 is reached.

The optical system is setup on a separate breadboard to ensure maximum stability and directed into the chamber using 2 inch mirrors. Before entering the chamber the repumping beams are overlapped and aligned with the cooling beams on two polarizing beam splitters, which are positioned between the quarter-wave plates and the mirror used for backreflection of the cooling beams.

The optimal parameters for the dark SPOT setup were determined experimentally. For experiments on multiple charge transfer in ion-atom collisions, highest density is important, and the setup was optimized to highest density using absorption imaging. This has been achieved by a dark spot with a diameter of 6 mm. The bright state fraction is given by equation 4.4 and can be measured either using absorption imaging or by detecting the fluorescence. In a dark SPOT configuration the fluorescence (P_d) originates only from the population in the bright state ($F = 3$). The bright state fraction in the trap is given by the ratio of the fluorescence in the dark SPOT configuration to the fluorescence when all atoms are pumped back in the bright state (P_b), corresponding to the peak at $t = 3$ s in figure 4.15:

$$p \approx \frac{P_d}{P_b}. \tag{4.6}$$

[5]Thorlabs, BC106-VIS

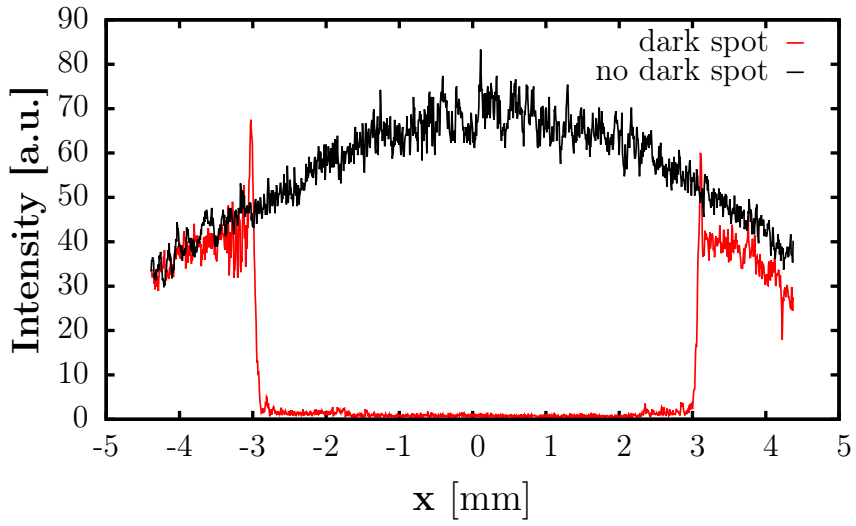

Figure 4.14: Extinction measurement of the dark spot. Shown are beam profiles, with and without the dark spot in the repump beam, measured with a CCD camera beam profiler. The black curve is a measurement without the spot, the red curve is the same measurement with the spot imaged onto the trap plane.

The results for the bright state measurements determined by fluorescence measurements, shown in figure 4.15, are surprising, since we determine $p = 0.35$ in a normal dark SPOT and only $p = 0.26$ in a forced dark SPOT setup[6], whereas $p \leq 0.1$ is expected. This result has been verified using absorption imaging for the normal dark SPOT, leading to $p = 0.08$ [7]. For the forced dark SPOT no data is available due to the low number of atoms in the bright state. The overestimation of atoms in the bright state measured using fluorescence might be due to the low bandwidth of the photodiode such that the peak after turning on the fill in beam cannot be fully resolved in time.

Using absorption imaging, the density in a typical bright MOT has been determined to be 2×10^{10} atoms/cm^{-3}. A density increase of one order of magnitude has been achieved in the dark SPOT setup, leading to densities of up to 2×10^{11} atoms/cm^{-3}, as expected. No effect of the depumper on the density has been observed in the experiment. Figure 4.16 shows the loading curves for the bright MOT (left) compared to the dark SPOT (right). Please note the different scales on the

[6] In a forced dark SPOT configuration the atoms are actively pumped in the dark state using the depumper.

[7] Atom numbers with and without a flash from the fill-in beam prior to absorption imaging, pumping the atoms back in the bright state, are compared.

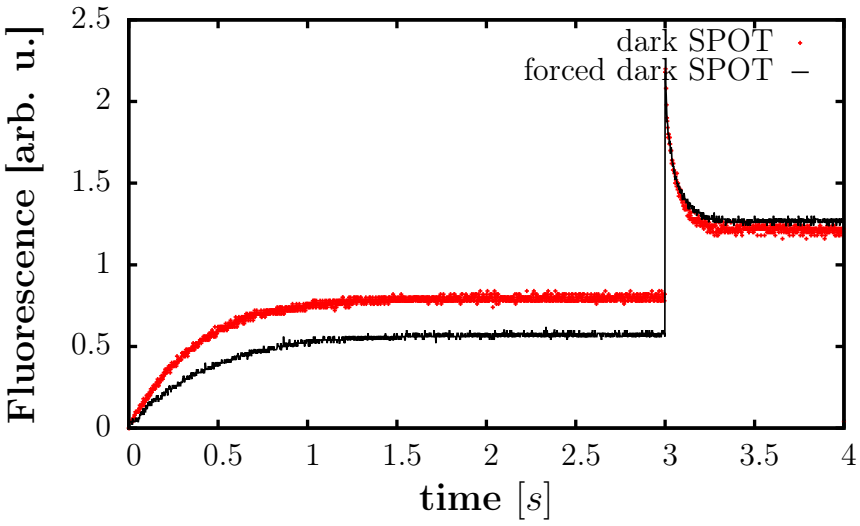

Figure 4.15: Fluorescence measurements of the forced dark SPOT (black curve) and a normal dark SPOT (red points). The MOT in dark SPOT configuration is loaded and at t = 3 s the fill in beam is switched on pumping all atoms back in the bright state. From the ratio of the fluorescence of atoms detected in the dark state and the one at t = 3 s, when all atoms are in the bright state, the bright state fraction is determined.

time axis and the number of atoms. In a bright MOT, typically $2.90(1) \times 10^8$ atoms/cm^{-3} with a loading rate of 3×10^9atoms/s at a temperature of $200\,\mu K$ are trapped[8]. Switching to a dark SPOT setup (without depumper) $7.4(6) \times 10^8$ atoms/cm^{-3} are trapped at a temperature of $170\,\mu K$ at a reduced loading rate of 1×10^9atoms/s.

4.6 Recoil ion momentum spectrometer

The dense and cold atom cloud will be used as a target for highly charged ions and is therefore trapped at the center of the recoil ion momentum spectrometer. Time and position focusing of ions produced inside the spectrometer enables the detection with high resolution of any momentum transferred to the recoil ion during collision with either a photon or an ion. Before describing all the details of the spectrometer developed in this work, first some general considerations will be discussed.

[8]The temperature of the atoms has been determined by time of flight measurements, where the ballistic expansion of the cloud is measured.

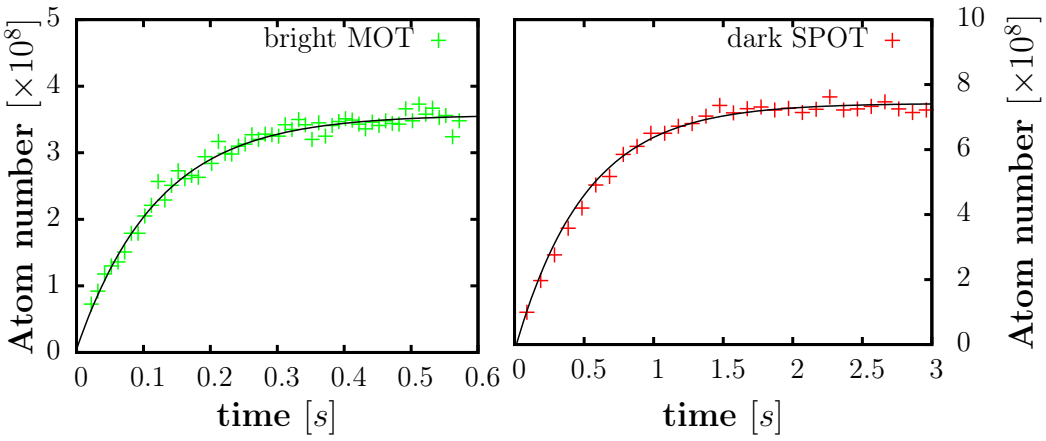

Figure 4.16: Loading curves of the targets. Note the difference in the axis for the two targets. The bright MOT traps $2.90(1) \times 10^8$ atoms with a loading rate of 3×10^9atoms/s, whereas the dark SPOT traps up to 7.4×10^8 atoms with a loading rate of 1×10^9atoms/s.

4.6.1 Design of the spectrometer: general considerations

Time-of-flight focusing of ions has been achieved by W. C. Wiley and I. H. McLaren in 1955 [94]. Key element is a spectrometer consisting of two different electric field regions, the acceleration region and a field-free drift region. One can show analytically that focusing in the time domain is achieved when the drift region is twice as long as the acceleration region. In order to include position focusing, a third field geometry, which acts as an electric lens, must be included. Therefore RIMS setups consist of three different field regions: a weak electric field for extraction of the ions from the collision region, a strong electric field region to focus the ions followed by a field free drift region. These setups are standard setups in the field of COLTRIMS. For a review refer to [3, 80, 5]. The resulting Laplace equation of this electric field configuration can only be solved analytically. Several commercial programs are available. In order to adapt the design of a RIMS to the current setup, all simulations in this work have been performed using SimION [95].

Different designs for these spectrometers are common: only few plates, separated by a large distance to generate the fields, which usually have 'curtains' to shield the inside are mostly used for velocity map imaging [96] and in the MOTRIMS setup in the group of R. Hoekstra in Groningen, described in chapter 3 [37]. In the COLTRIMS community it is more common to have many thin electrodes only separated by a few mm from each other. Shielding is achieved if the distance d between the plates is smaller than the diameter of the electrode rings. In the current

setup we follow this design.

The design of the spectrometer has several free parameters: the number of electrodes, the position of the focusing electrode, which determines the resolution and the position of the focal plane, inner/outer diameter of the plates as well as the distance between the plates. In order to determine some of the parameter the following constraints need to be taken into account: Since the field inside the spectrometer is weak it is indispensable to shield the inside from electric stray fields originating from the surrounding ultra-high vacuum chamber, which is on mass. In order to combine RIMS with laser cooling and trapping enough optical access needs to be included in the field plates. The trapping lasers of our setup have a $1/e^2$ diameter of 20 mm and puts a lower limit to the size of the holes in the spectrometer. This puts a limit to the inner diameter of the plates, since it needs to be large enough so that the electric field homogeneity is not affected. Furthermore, the spectrometer will be used to detect multiple charge transfer between highly charged ions (up to bare uranium) which leads to high momentum and Q-values of the recoil ion.

Another constraint is given by the mechanical setup. The only available connection to the vacuum chamber for the spectrometer is a CF150 flange, which puts an upper constraint to the size of the outer diameter of the electrodes and the drift tube. In the following the mechanical design and the results of the simulations are described in detail.

4.6.2 Mechanical design

The spectrometer head is shown in figure 4.17 and is similar to the design described in [41]. It consists of 34 stainless steel electrodes. Each electrode, except for the first one which is a full circle, has an outer diameter of 100 mm and an inner diameter of 75 mm and a thickness of 1 mm. The electrodes are all mounted on four M3 thread rods. In order to prevent electrical contact between the plates, ceramic spacer are placed between the plate. The distance between neighbouring plates is 4 mm. Since ceramics might charge up, in particular when the spectrometer is used in combination with an ion beam, and thus lead to a huge electric stray field inside the spectrometer, each of the ceramic spacers is covered with a stainless steel ferrule. Only 0.5 mm of the ceramic spacer is thus visible. All adjacent electrodes are connected by 1 MΩ resistors each. The resistors are squeezed through holes of 650 μm leading to good electrical contact (see figure 4.18). 12 out of all the plates have some sections cut for optical access of the trapping lasers. Special care must be taken of the three plates at the center. These need optical access from 4 sides, so that they are cut into four pieces. The neighboring electrodes, which are still in one piece, are used to position the four pieces of electrodes. The non-connecting electrodes and

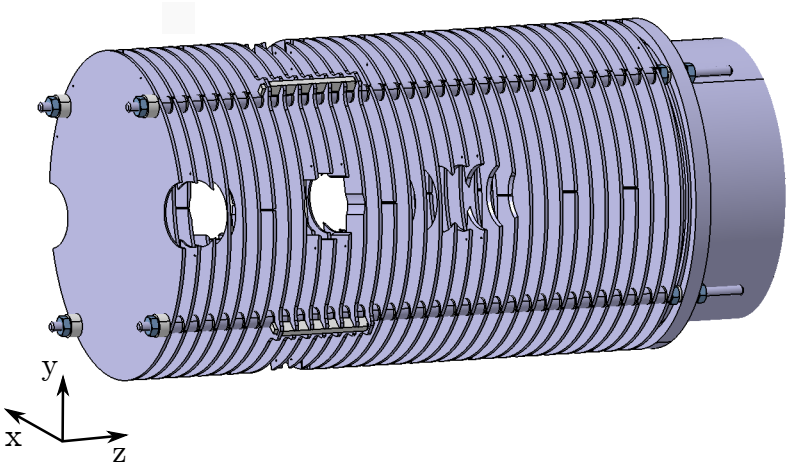

Figure 4.17: Mechanical design of the spectrometer head. The spectrometer head consist of 34 electrodes, connected to each other in a resistor chain. Ceramic spacer insulate the plates and are covered with ferrules. Also seen are the extra lugs and ceramic plates, holding in place the plates which are cut into four pieces. Note the particular coordinate system, which has been adopted from SimIon [95].

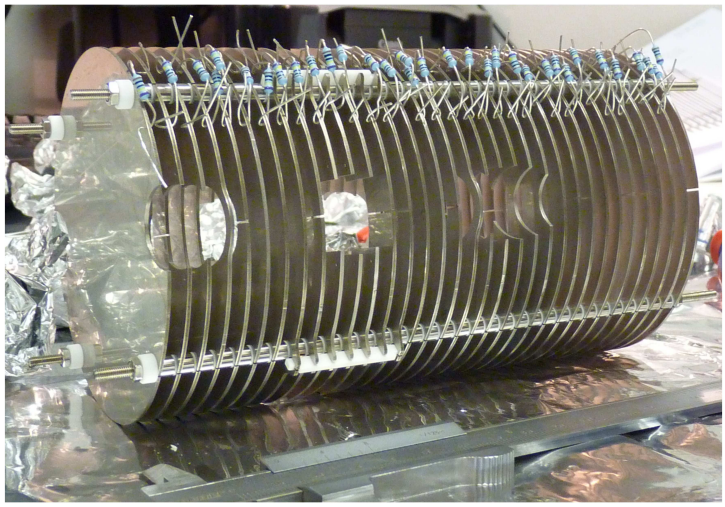

Figure 4.18: Pictures of the spectrometer head. The 33 plates are connected through 1 MΩ resistors, the 34th plate being the drift tube. The plates have holes for optical access for the laser and the projectile beam.

their neighboring electrodes have extra lugs at their outside. A ceramic plate which fits into these lugs is used as a place holder. Thus they are fixed and cannot move during transportation. The remaining ring electrodes, the drift tube and all ferrules are sliced in order to prevent eddy currents induced by switching of the magnetic quadrupole field.

Numbering the pusher plate as plate 0 and the drift tube as plate 34, we apply an extraction voltage U_p to the pusher plate. The collision region, corresponding to the center of the trapping region, is situated at plate 11 and is grounded so that the effect of electric stray fields from the surrounding chamber are reduced. Plate 14 is set to an independent voltage, the focus voltage U_f. The drift tube itself is part of the spectrometer and can be set to an independent voltage. It is set to the same potential as the mesh in front of the downstream detector.

4.6.3 Position sensitive detection and data acquisition

For detection of the ions' time of flight and position the downstream detector consists of a multichannel plate (MCP) assembly in Z-stack configuration in combination with a delay-line anode, commercially available from Roentdek (DLD 80) [68]. The MCPs have an active diameter of 80 mm and is followed by a delay-line anode with a linear active diameter of also 80 mm. Two-dimensional position readout is done by the delay-line, consisting of wires wound around a support in two dimensions. The pitch for one revolution is about 1 mm. A charged particle hitting the MCP releases an electron cloud from the MCP back. This cloud is accelerated towards the delay-line which is on a slightly higher potential (typically +270 V) and produces a charge pulse which subsequently propagates along the wire[9]. The perpendicular signal speed $v_\perp$ depends on the size of the delay-line and is in our case 0.95 ns/mm. Detecting the time difference of the charge pulses at each end of the wire of the delay line, X_1 and X_2, one can now deduce the position X on the detector form the time difference δt (see figure 4.19):

$$X = X_1 - X_2 = 2 \cdot t_1 \cdot v_\perp - 2 \cdot t_2 \cdot v_\perp \tag{4.7}$$

$$\Rightarrow X = \tfrac{t_1 - t_2}{2 v_\perp}(X_1 - X_2). \tag{4.8}$$

The same holds for the y-direction such that two-dimensional information is obtained.

Time-of-flight is measured by recording the ion signal from MCP back as a stop signal, where the start is given by the projectile beam. An ion hitting the MCP

[9] In order to reduce dispersion during propagation, each wire is in reality a Lecher line, i.e. a pair of wires set to a slightly different potential of 36 V by a block of batteries.

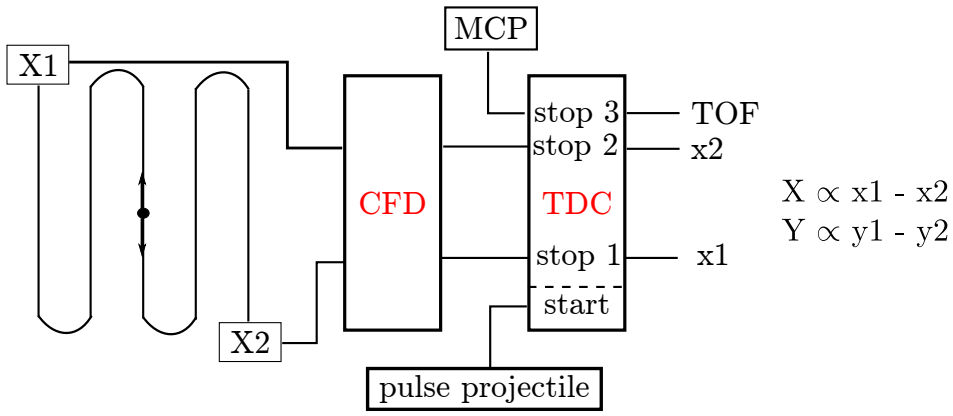

Figure 4.19: Sketch of delay-line anode and data acquisition. The ion hitting the MCP induces a signal on the delay line which propagates along the wire. At the end the signal is outcoupled capacitively. After discrimination in a constant fraction discriminator (CFD), the time of the signals $X1$ and $X2$ is measured using a TDC. From the difference in time the position X on the delay-line can be deduced. Time of flight information is obtained by measuring the time difference between the pulsed projectile beam, creating the recoil ion, and the ion hitting the MCP.

short circuits the plates, inducing a voltage drop on the stack. Both the MCP back signal and the delay-line signals are coupled out capacitively. This signal is further preamplified in a differential amplifier before being discriminated in constant-fraction discriminators, which gives out a logical NIM signal. These signals are further detected by a time-to-digital converter (TDC, TDC8HP from Roentdek), measuring the times with a high resolution of 25 ps.

4.6.4 Characteristics of the spectrometer

Assuming again that the electric field within the spectrometer head is constant and neglecting any initial momentum of the recoil ion in z-direction, an analytic expression for the time of flight depending on the extraction field E can be obtained from equation 2.23:

$$t(E) = \sqrt{\frac{2L_{\text{extrac}}m}{qE}} + \frac{L_d}{\sqrt{2L_{\text{extrac}}qE/m}}, \tag{4.9}$$

where L_{extrac} is the distance the recoil ion travels inside the spectrometer head, L_d is the length of the drift tube and q is the charge state of the recoil ion. Together with equation 2.21, the maximum detectable momentum in x and $y-$direction depending

on the extraction field can be obtained:

$$p_{\text{long,max}} = p_{\text{trans,y,max}} = m\frac{r_{det}}{t(E)}, \tag{4.10}$$

where r_{det} is the radius of the detector. The result for our geometry is shown in fig. 4.20.

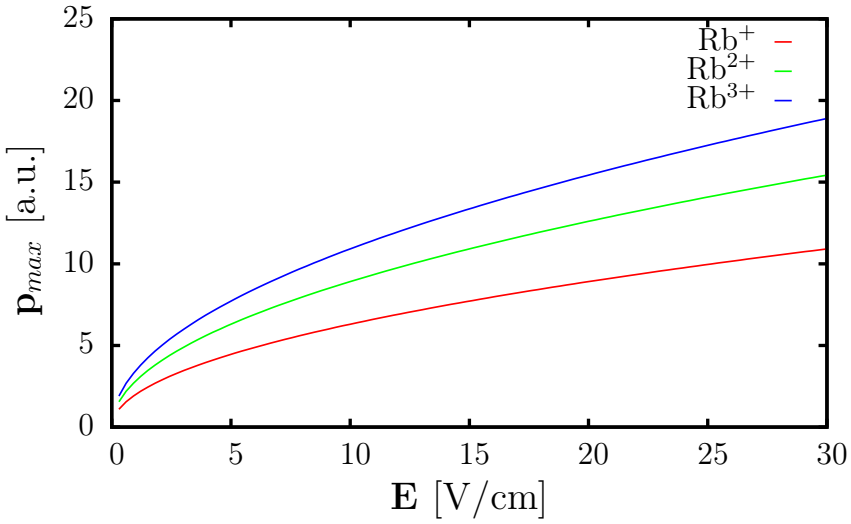

Figure 4.20: Maximal detectable momentum in x and y-direction as a function of the extraction voltage E due to finite size of the detector. Depending on the charge state and the extraction voltage of the spectrometer, an upper limit for detection with 4π solid angle exists. Shown are the maximum momenta for Rb^+ (red), Rb^{2+} (green) and Rb^{3+} (blue).

4.6.5 Time and position focusing

In order to detect the recoils' ion momentum with high resolution, the initial ion distribution needs to be focused in time and position, i.e. ions starting from different positions along the time of flight axis should all arrive on the detector at the same time, while ions starting from different position along the projectile/laser beam axis should all hit the detector at the same position. The design of the spectrometer is therefore a trade off between resolution in space and in time. Since the electric field configuration inside the spectrometer acts as an electric lens, the position of the focal planes for time of flight and position differs. In order to determine the best configuration (number of electrodes, position of collision region, position of focusing

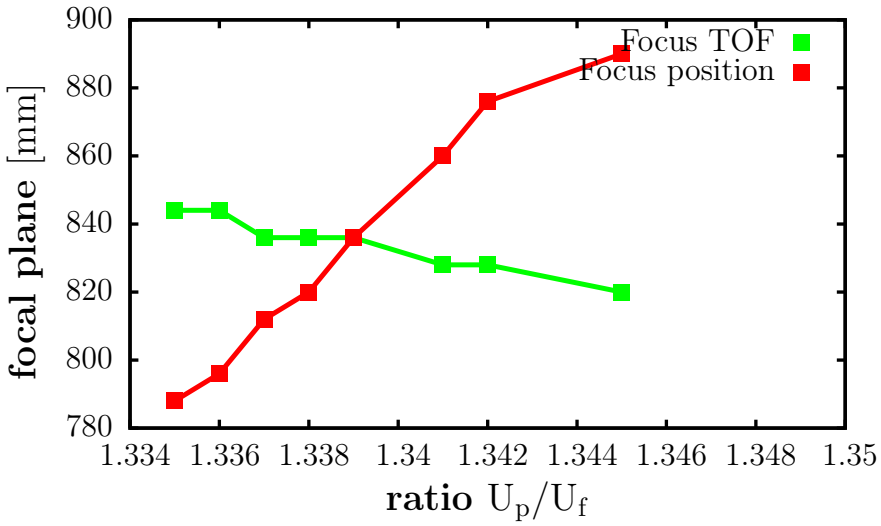

Figure 4.21: Simulation of the focal planes TOF and position focusing. The electric lens is optimized for having the best trade off of the resolution in time of flight and position. For our design the optimal was found for a ratio of $U_p/U_f = 1.339$ at a distance of 785.5 mm from the collision region.

lens, position of focal plane, resolution) the ratio of pushing to focusing voltages U_P/U_f is varied in the simulation and for each the focal planes for time of flight as well as position are determined. The intersection of both is than chosen to be the focal plane in the experiment, i.e. the position of the detector. In total the spectrometer has 34 electrodes, the last one being the drift tube. The total length of the spectrometer head is thus 170 mm, followed by a 666 mm field free drift tube. The collision region is situated at electrode 11, which corresponds to a distance of 50.5 mm away from the pushing electrode. Electrode 14 is used as the focusing plate. This configuration leads to a focal plane of the spectrometer at 836 mm from the pushing voltage, i.e. 785.5 mm downstream the collision region, with an optimized ratio of $U_p/U_f = 1.339$. The result is shown in figure 4.21.

The principle of time and position focusing is shown in figure 4.22. Doubly-charged rubidium ions emerging from a sphere with 6 mm diameter start from the position of the collision region either without initial momentum, or with a momentum of 10.9 a.u. either in time of flight direction or in y-direction. The pushing plate is set to 30 V, leading to an electric field of 1.76V/cm. Ions with no momentum hit the detector at the center after a time of flight of 90.35 μs. Ions starting with initial momentum in transverse direction hit the detector 475 ns later when applied to the time of flight direction and 16.8 mm outside the center when applied

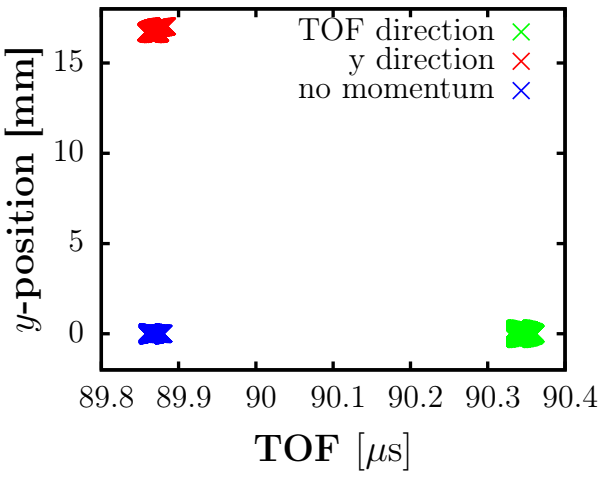

Figure 4.22: Focusing characteristics of the spectrometer. Simulation of 1000 ions starting from the collision region with a spherical distribution (6 mm diameter) and no momentum (blue), $p_{trans} = 10.6$ a.u. in y-direction (red) and in TOF direction (green). The ions are focused in position and time of flight onto the detector. Due to the size of the target imperfect focusing can be seen.

to the y-direction. The initial size of the ion distribution of 6 mm is focused down in position to $\delta y < 170\,\mu$m and in time of flight to 5 ns. Simulations show that the resolution is limited by the size of the target: the same simulations for a smaller initial ionization volume of 1 mm in diameter show that the ions will be focused down to $\delta y < 20\,\mu$m and $\delta t = 1$ ns.

Since the size of our trapped atoms turned out to be much bigger than originally thought, this size dependence is investigated further for smaller momentum transfer, resulting in a smaller area of the detector which is covered such that the effect can be seen better. Simulations for typical momenta transferred from photoionization (see sec. 5.1.3) are shown in figure 4.23. Due to the much smaller momentum transferred of only 0.1862 a.u., the electric field in the spectrometer head is lowered to 0.3 V/cm. Again, momentum is applied either in TOF or in y-direction. For comparison ions without initial momenta are also simulated. The left figure shows the focusing of an initial spherical ion distribution of 1 mm diameter, while the right figure shows the same simulation for an initial spherical ion distribution of 6 mm. The rather large ionization volume of 6 mm also shows non-perfect focusing for the ions starting from outside the focal plane of the electric lens.

In order to get best resolution, a small ionization volume is needed. There are several possibilities of how this can be achieved; either by focusing down the projec-

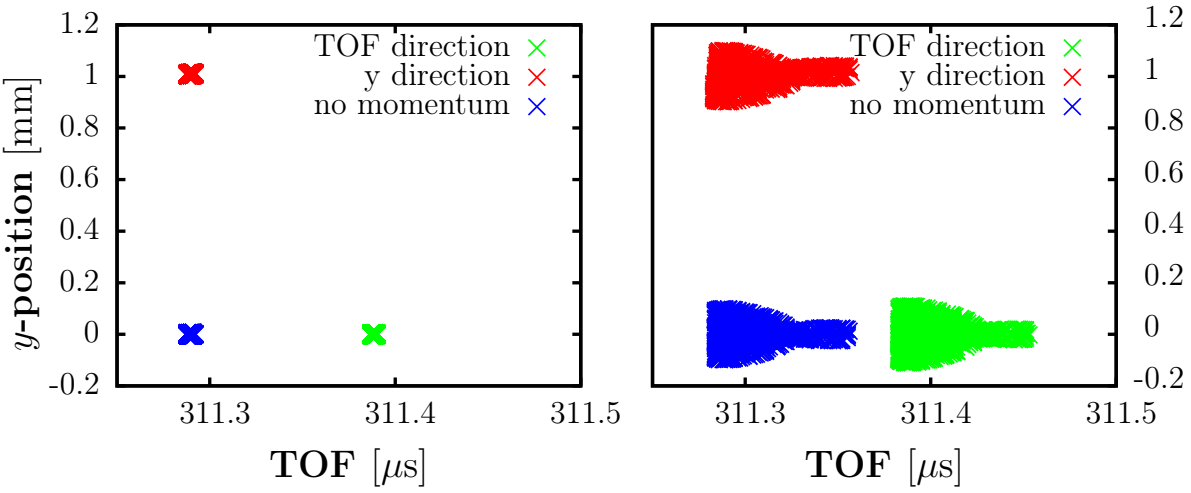

Figure 4.23: Simulation of 1000 ions from a sphere with 1 mm diameter starting at the position of the magneto-optical trap (left) and a sphere of 6 mm (right) with either no initial momentum or initial momentum of 0.1862 a.u. either in direction of time of flight or in y-direction. The resolution is limited by the size of the initial cloud.

tile beam, which is easy to implement for photoionization experiments, but rather difficult for ion beams, since the initial beam shape of the ion beam must be well known. Not only the characterization of ion beams is rather elaborate, but also the size of the focus itself is limited by repulsive interaction among the ions in the beam itself. Another possibility is to apply a higher magnetic field gradient, which leads to higher switching times of the target and thus slower repetition rates. Also, the atoms expand after switching off the magnetic field with a velocity of about 0.2 m/s such that longer switching times lead to smaller densities of the ionization volume. The most elegant solution is to transfer the trapped atoms in a dipole trap and is planned as a next step (typical sizes of dipole traps are on the order of 100 μm in a single beam dipole trap or even 30 μm when a dimple is included.).

4.6.6 Simulations on ion-atom collisions

The longitudinal as well as the transverse momentum in y-direction are directly proportional to the position X/Y of the recoil ion hitting the detector (see section 2.1.5). Using SimIon simulations, the parameter linking position and momentum (see equation 2.21) in x- and y-direction for the $U_P = 30$ V, used in this section, are determined to $a = 0.65$. In the case of time of flight (see equation 2.24), $b = 23.0$ is obtained. These parameters are of course a function of the applied pusher voltage as

well as the charge state of the recoil ion. However, the spectrometers differ slightly from the simulations. Therefore, these parameters are determined experimentally from know spectra which are measured prior to the actual experiment.

The setup is designed to investigate multiple charge transfer between highly charged ions and rubidium atoms at the HITRAP facility at GSI Darmstadt. In this facility slow highly charged ions up to bare uranium will be available. In first test experiments collisions between rubidium atoms and Ar^{16+} from an EBIT, which is connected to the same beamline, are planned:

$$Rb(5s) + Ar^{16+} \longrightarrow Rb(5s)^{n+} + Ar^{(16-n)+}. \tag{4.11}$$

In these experiments very large scattering angles up to 0.5 mrad and energy transfer of 150 eV are expected [56]. Exemplary simulations for four different scenarios at a projectile velocity of $v_P = 0.3$ a.u. have been performed: two different Q-values $Q = 150$ eV and $Q = 151$ eV with corresponding scattering angles of 0.3 mrad and 0.5 mrad. For the simulations 1000 ions are Gaussian distributed with a size of $\sigma_{x,y,z} = 0.3$ mm. The extraction field within the spectrometer is 1.76 V/cm such that a large area of the detector is covered. The three-dimensional distribution of the recoil ions at the focal plane is shown in figure 4.24. Due to the symmetry of the collision the projection shows a ring in the transverse momentum direction. The different Q-values result in discrete lines along the x-direction.

The projection of the ion distribution on the xy-plane shows the focusing characteristics of the spectrometer. The initial spatial ion distribution is focused down to a final $\sigma_x = 0.03$ mm and is thus one order of magnitude smaller than initially. The resolution of the spectrometer for these parameters is simulated to be $\delta p_{trans} = \delta p_{long} < 0.05$ a.u..

The overlap of the target with the projectile beam must not necessarily be in the center of the spectrometer head. The focusing capability of the spectrometer for small deviation from the center are shown in figure 4.26 for an initial ion distribution with $\sigma = 0.3$ mm produced with a Ar^{16+} projectile beam at a velocity of $v_P = 0.3$ a.u. and a Q-value of $Q = 150$ eV. Even if the collision region is displaced by 5 mm from the center of the spectrometer, the ions are still focused to less than 60 μm, which is still smaller than the typical resolution of an MCP.

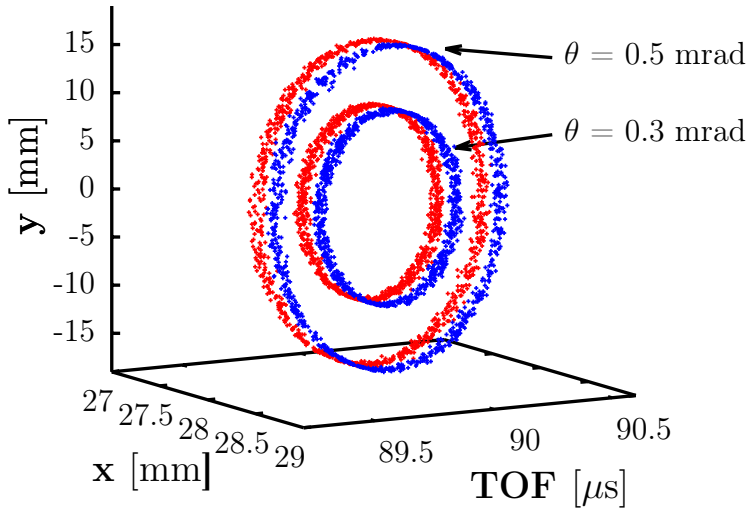

Figure 4.24: Simulated time of flight and position of the projected ion distribution after collision with Ar^{16+} and a Q-value of 150 eV (red) and 151 eV (blue) with scattering angles of $\theta = 0.3$ mrad and $\theta = 0.5$ mrad respectively.

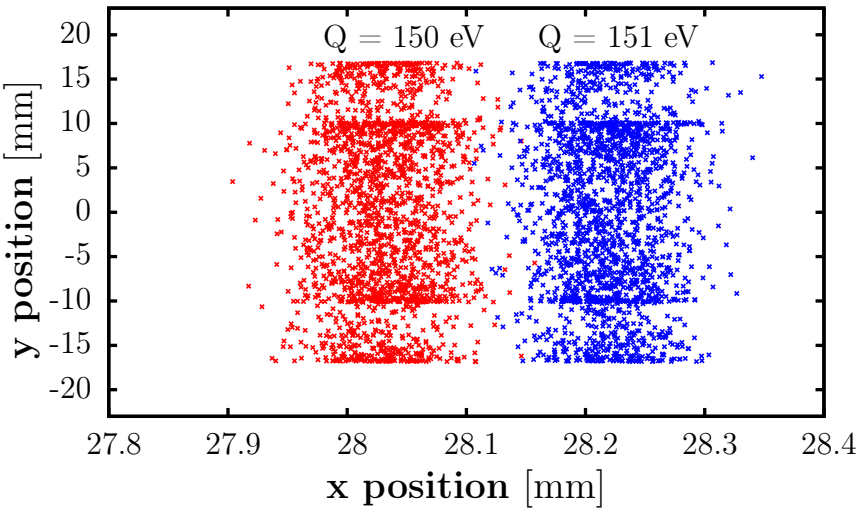

Figure 4.25: Projection on the xy-plane of the simulated ion distribution. The initial size of the ion distribution is focused down by one order of magnitude from $\sigma = 0.3\,\text{mm}$ to $\sigma = 0.03\,\text{mm}$, leading to a resolution better than $\delta p = 0.05\,\text{a.u.}$

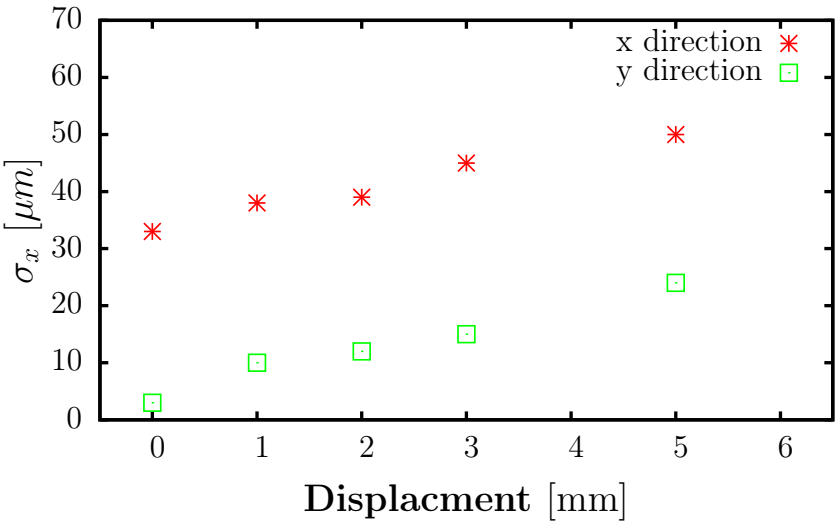

Figure 4.26: Focused ion distribution for displacement of the ionization volume from the center of the spectrometer head. Even for a displacement of 5 mm from the center of the trap the projected ion distribution is still well below 100 μm, which is the typical resolution of MCPs.

Chapter 5

Characterization of the setup using photoionization

This chapter presents the first experimental results obtained with the upgraded setup. Non-resonant two-photon ionization of cold rubidium atoms is used as a versatile tool to characterize the setup. The theoretical background on photoionization is given in section 5.1. In first experiments, photoionization is used to characterize the atom beam as well as the 3D MOT. The experimental setup is presented in section 5.2. This measurement does not only represent an alternative and independent measurement tool for state of the art density measurements, but also, for the first time, gives insight into the optimized spatial arrangement of the atom beam generated from the 2D MOT with respect to the trapping in a 3D MOT and is described in section 5.3. In section 5.4, we show how photoionization of magneto-optical traps can be used to characterize the recoil ion momentum spectrometer. The velocity distribution of the atom beam is an alternative to calibrate the spectrometer, presented in section 5.5.

5.1 Photoionization

Photoionization of atoms can occur during interaction of an atom with an electromagnetic field. In a rigorous treatment both the atomic system as well as the radiation field need to be treated quantum mechanically, although many textbooks treat the radiation field classically. In this section the treatment proposed by [97] and summarized in [98] will be followed. Photoionization occurs when an atom in an initial state $|\phi_i\rangle$ absorbs a photon with energy $\hbar\omega_{\text{photon}}$ bigger than the ionization energy E_{ion} of that initial state

$$\hbar\omega_{\text{photon}} > E_{\text{ion}}. \tag{5.1}$$

The energy released in this process is the difference between the binding energy and the photon energy. This energy is distributed among the resulting ion and the ejected electron according to momentum conservation.

The interaction between an atom and a radiation field can be seen as a perturbation of the non-interacting Hamiltonian $\hat{H}_0$ of the atom and the photon field. The perturbation causes time-dependent transitions between the unperturbed eigenstates $|\phi_i\rangle$ of the initial system and can, in the low intensity limit, well be described by the time-dependent perturbation theory. The system is then described by the Hamiltonian

$$\hat{H} = \hat{H}_0 + \hat{W}(t), \tag{5.2}$$

where $W(t)$ is the interaction Hamiltonian. The eigenstates $|\phi_i\rangle$ of the unperturbed Hamiltonian H_0 form a complete basis in which the time-dependent wavefunction $|\Psi(t)\rangle$ of the system can be expanded. The transition probability per unit time from the initial to the final state $|\phi_f\rangle$ in the first order perturbation theory is given by Fermi's Golden rule:

$$P_{|\phi_i\rangle \to |\phi_f\rangle} = \frac{2\pi}{\hbar} \left| \langle \phi_i | \hat{W} | \phi_f \rangle \right|^2 \rho(E_f = E_i), \tag{5.3}$$

where $\rho(E_f)$ is the density of final states in the continuum and its precise definition depends on the normalization of the final states.

In case of a quantized radiation field, the non-interacting Hamiltonian is a sum of the atomic and a radiative field part:

$$\hat{H}_0 = \hat{H}_A + \hat{H}_F. \tag{5.4}$$

The interaction Hamiltonian $\hat{W}(t)$ is given by

$$\hat{W(t)} = \frac{e}{mc} \sum_i^N [\hat{\mathbf{p}}_\mathbf{i} \cdot \hat{\mathbf{A}}_\mathbf{i}(r,t) + \hat{\mathbf{A}}_\mathbf{i}(r,t) \cdot \hat{\mathbf{p}}_\mathbf{i}], \tag{5.5}$$

where $\hat{\mathbf{A}}_\mathbf{i}(r,t)$ is the vector potential obtained using the Gauge theory, $\hat{\mathbf{p}}_\mathbf{i}$ is the momentum of the electrons, m the mass, e the elementary charge and c the speed of light. In the first order perturbation theory again the quadratic contribution of the vector potential can be neglected. In this quantized radiation picture, the initial state $|\phi_i\rangle$ and final state $|\phi_f\rangle$ can be written as a product of an atomic eigenstate $|\Phi_n\rangle$ of $\hat{H}_A$ and an eigenstate of the field operator $\hat{H}_F$:

$$|\phi_i\rangle = |\Phi_i\rangle |..., n_\lambda, ...\rangle, \qquad |\phi_f\rangle = |\Phi_f\rangle |..., n'_\lambda, ...\rangle. \tag{5.6}$$

n_λ and n'_λ are the occupation numbers of the eigenstates. The corresponding energies of the final states E_i and E_f are the sum of the respective eigenvalues ϵ_i and ϵ_f of $\hat{H}_A$ and the energy of the photon field. During absorption, usually only one mode contributes while all other modes play the spectator role and

$$E_i = \epsilon_i + n_\lambda \hbar\omega_\lambda \qquad \text{plus energy of spectator modes,} \tag{5.7}$$

$$E_f = \epsilon_f + n'_\lambda \hbar\omega_\lambda \qquad \text{plus energy of spectator modes.} \tag{5.8}$$

From this the energy conservation can be deduced

$$\epsilon_f - \epsilon_i = (n_\lambda - n'_\lambda)\hbar\omega_\lambda, \tag{5.9}$$

saying that the energy gain of the atom corresponds to the energy loss of the photon field.

If the wavelength of the absorbed photons is much larger than the spatial size of the atom the dipole approximation holds. In this case the matrix elements can be reduced to only a matrix element involving the atomic degrees of freedom and reads:

$$W_{fi} \propto \sum_{i=1}^{N} \langle |\Psi_f| \boldsymbol{\pi}_f \cdot \hat{\mathbf{p}}_i |\Psi_i\rangle F_\lambda \tag{5.10}$$

where $\boldsymbol{\pi}_f$ is the polarization of one mode λ and F_λ stands for the field contribution, given by

$$F_\lambda = \langle ..., n_\lambda, ... | \hat{b}_\lambda + \hat{b}^\dagger_\lambda | ..., n'_\lambda, ... \rangle. \tag{5.11}$$

$\hat{b}_\lambda$ and $\hat{b}^\dagger_\lambda$ are the annihilation and creation operators for photons which respectively lower or raise the number of photons in one mode defined as $\hat{b}^\dagger_\lambda |..., n_\lambda, ...\rangle = \sqrt{n+1}|..., n_\lambda + 1, ...\rangle$ and $\hat{b}_\lambda |..., n_\lambda, ...\rangle = \sqrt{n}|..., n_\lambda - 1, ...\rangle$. It follows that the transition rate is proportional to the number of photons absorbed from one mode λ and the ionization rate can be written as the product of a cross section σ_{ion} and the number of photons per unit time and area Φ

$$P_{|\phi_i\rangle \to |\phi_f\rangle} = \sigma_{\text{ion}} \cdot \Phi. \tag{5.12}$$

The cross section is then given by

$$\sigma_{\text{ion}}(E) = 4\pi^2 \frac{e^2}{\hbar c} \hbar\omega_\lambda |\boldsymbol{\pi}_\lambda \cdot \mathbf{r}_{fi}|^2. \tag{5.13}$$

Due to the normalization of the final states $\langle \Phi_f(E) | \Phi_f(E') \rangle = \delta(E - E')$, $\mathbf{r}_{fi}$ has the dimension of length times the inverse square root of an energy, such that the

cross section has the dimension of an area.

5.1.1 Multiphoton ionization of atoms

Pulsed lasers have enough energy in one pulse to induce multiphoton ionization, i.e. the absorption of more than one photon per pulse where the energies of the photons sum up, leading to ionization even if the photon energy is lower than the ionization energy of the atom. This is called multiphoton ionization. Two different scenarios are possible: the atom absorbs two or more photons non-resonantly, where no atomic state is resonant to the photon energy (see figure 5.1 c)). In case the atom has a bound state resonant with the photon energy of a mode of the ionizing field, the process is called resonance enhanced multiphoton ionization (REMPI) and is sketched in 5.1 b).

The process of multiphoton ionization is less likely than one-photon ionization and higher orders need to be included in the perturbation theory to describe it. Multiphoton ionization almost exclusively occurs in the light field of pulsed lasers, where the peak intensities are high enough. For two-photon ionization the probability of ionization is obtained from second order perturbation theory and the ionization probability is now proportional to the square of the photon flux [97, 99]

$$P_{|\phi_i\rangle \to |\phi_f\rangle} = \sigma_{2,\mathrm{ion}}(\omega) \cdot \Phi^2, \tag{5.14}$$

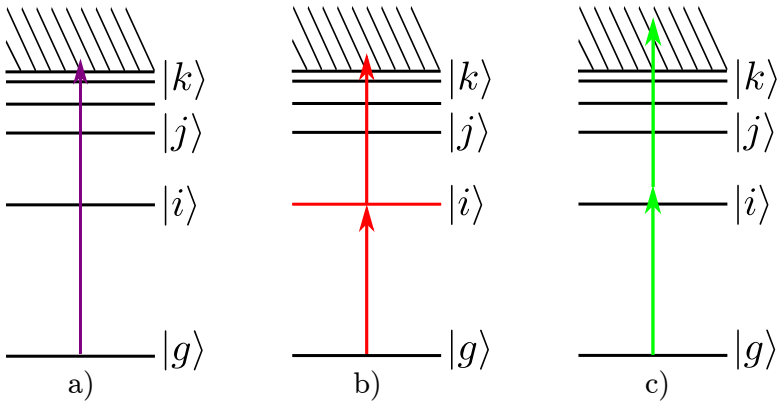

Figure 5.1: Ionization schemes for multiphoton ionization. In a) absorption of one photon, where the photon energy is bigger than the ionization energy of the atom, leads to ionization. In b) REMPI is shown, where the atom absorbs two photons, the first photon populates a bound state of the atom. In c) non resonant multiphoton ionization is shown.

where $\sigma_{2,\mathrm{ion}}(\omega)$ is the two-photon ionization cross section and is proportional to the summation over all intermediate states m, weighted with the detuning ΔE

$$\sigma_{2,\mathrm{ion}}(\omega) \propto \sum_m \frac{\langle f|\hat{\mathbf{d}}|m\rangle\langle m|\hat{\mathbf{d}}|i\rangle}{E_m - E - i - \hbar\omega - i\eta\hbar}. \tag{5.15}$$

$\hat{\mathbf{d}}$ is the dipole operator. The term $i\eta\hbar$ can be neglected in case of nonresonant multiphoton ionization. Including the fact the multiphoton ionization is only observed in pulsed laser with pulse length τ and repetition rate ν_{rep}, the rate for two-photon ionization is given by

$$R(\omega) = \tau\nu_{rep} \cdot N_a \cdot \sigma_2(\omega) \cdot \Phi^2. \tag{5.16}$$

N_a is the number of atoms in the ionization volume.

The experiments reported on in this thesis are all done in the low intensity regime. However, with the development of very short, high intensity laser pulses many different effects have been observed. Namely above threshold ionization can be observed, where a bound electron can absorb more photons than needed for ionization and the electron energy spectrum shows a whole series of equidistant energy peaks, each separated by one photon energy [100]. At high enough intensities of the radiation field the external field dominates the ionization process by modifying the atomic potential. Different regimes can be distinguished here, depending on how strong the atomic potential has been modified. Tunneling ionization occurs when the potential barrier is lowered by the external field and the electron can tunnel through, even if the electron is still in a bound state [101]. When the potential barrier is lowered even further, such that even the ground state is not bound any more, over-the-barrier ionization occurs [102]. Depending on the pulse length, the ionized electron can rescatter with the electric field [103].

5.1.2 Angular distribution of photoelectrons

In photoionization experiments one important feature is the angular distribution of the ejected electron. In the case of one-photon ionization of ground state atoms the angular distribution of photoelectrons is given by the differential cross section for photoionization [104] and can be written as

$$\frac{\mathrm{d}\sigma^{(1)}}{\mathrm{d}\Omega} = \frac{\sigma_{\mathrm{total}}}{4\pi}(1 + \beta_2 P_2(cos(\theta))), \tag{5.17}$$

where θ is the angle between the direction of the emitted electrons and the quantization axis, in this case the polarization axis of the ionizing light. σ_{total} is the total

ionization cross section and P_2 is the second order Legendre polynomial. β_2 can take values between -1 and 2 and is called the anisotropy parameter. For $\beta_2 = 0$ the emission is isotropic, whereas for β_2 = -1 and $\beta_2 = 2$ the anisotropy is largest. The angular distribution for these cases is depicted in polar coordinates in figure 5.2.

Equation 5.17 is only valid for an isotropic initial state, i.e. when all m-substates of the initial atoms are equally populated. Therefore, in the case of resonant or nonresonant multiphoton ionization, where the intermediate states populate more than one m-substate, higher order Legendre polynomials have to be included. The only exception is resonant multiphoton ionization when all states being populated have the same number of m-levels and the light is linearly polarized. For all other cases of N-photon ionization equation 5.17 can be generalized to [105]

$$\frac{\mathrm{d}\sigma^{(N)}}{\mathrm{d}\Omega} = \frac{\sigma_{\mathrm{total}}}{4\pi} \sum_{j=1}^{N} \beta_{2j} P_{2j}(cos(\theta)). \tag{5.18}$$

The physical interpretation of this distribution is that starting from a spatially isotropic atom the interaction with the incoming photon leads to a dipole character of the total system, displayed in the spatial anisotropy. For N photon absorption, the spatial anisotropy is increased N times, again due to the dipole character of each photon-atom interaction. Thus angular distributions including higher polynomials always have higher spatial anisotropy, i.e. higher emission probability along the polarization axis of the laser. The angular distribution for two-photon ionization with $\beta_4 = 1$ is shown in figure 5.2 a) and b). In both cases β_2 is kept constant as compared to 5.2 c) and d), now including a second order polynomial of $\beta_4 = 1$, as a typical example of two-photon ionization.

5.1.3 Multiphoton ionization of rubidium atoms

In the following multiphoton ionization of ^{85}Rb is described in more detail. In the current experiment a pulsed frequency doubled Nd:Yag laser emitting light at 532 nm with a pulse width of 10 ns and a repetition rate of 20 Hz is used for non-resonant two-photon ionization of the magneto-optically trapped atoms. Due to the cooling and trapping light, which is resonant with the D2 line ($5S_{1/2} \rightarrow 5P_{3/2}$), we estimate that always a fraction of 30 % (see section 4.5) of the atoms are in the excited state. Ionization from the ground state is achieved by switching off the trapping light prior to ionization. The ionization energy from the ground state is 4.177 eV, the one from the excited state is 2.58 eV. One photon of the Nd:Yag laser carries 2.33 eV such that ionization from both states involves absorption of two photons. The energy width of one laser pulse is only 0.2 μeV and can be neglected. The

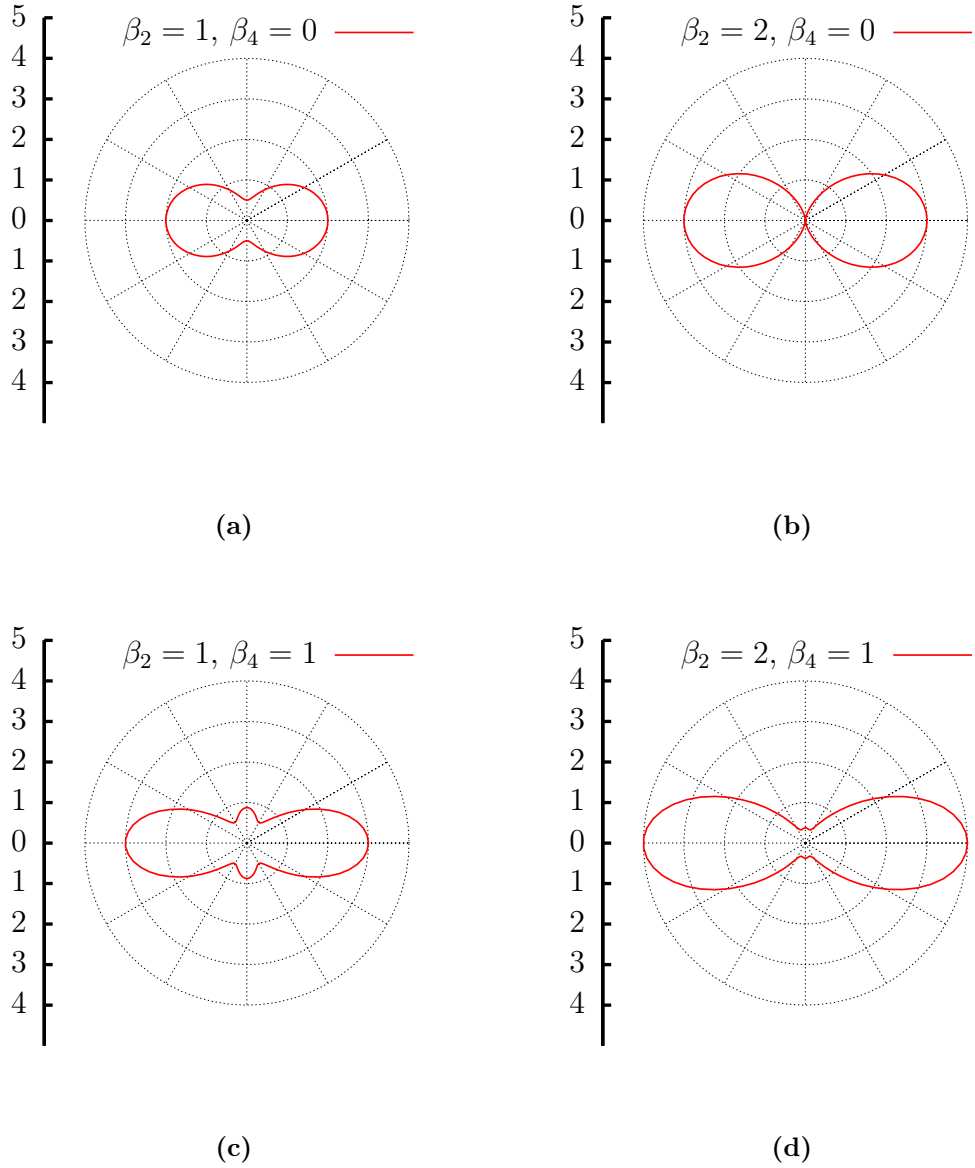

Figure 5.2: Angular photoelectron emission distribution for different anisotropy parameters during multiphoton ionization.
Upper graphs: one-photon ionization: a) $\beta_2 = 1, \beta_4 = 0$, b) $\beta_2 = 2, \beta_4 = 0$,
Lower graphs: two-photon ionization: c) $\beta_2 = 1, \beta_4 = 1$, d) $\beta_2 = 2, \beta_4 = 1$,

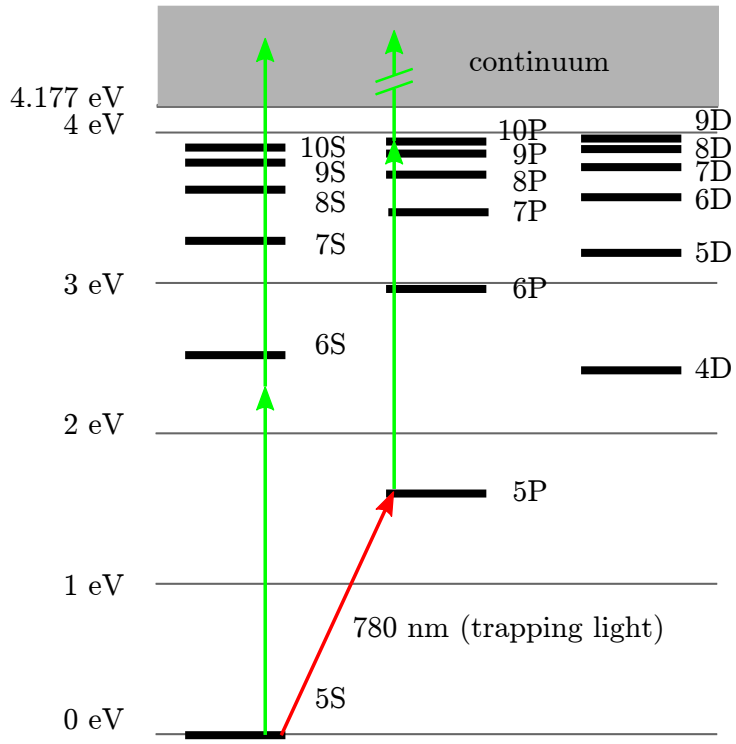

Figure 5.3: Energy level diagram of ^{85}Rb. Only the important levels for multiphoton ionization discussed in the text are shown. Hyperfine splittings are not shown. Values taken from [106].

energy level diagram including the most important levels that need to be considered for multiphoton ionization is shown in figure 5.3.

Ionization from the ground state leads to

$$Rb(^2S_{1/2}) + 2h\nu \rightarrow Rb^+(^1S_0) + e^- + \Delta E \tag{5.19}$$

with an excess energy of $\Delta E = 0.543$ eV. Leaving the trapping light on and ionizing from an excited state leads to $\Delta E_{\text{exc}} = 2.0$ eV. The excess energy translates into kinetic energy of the fragments, i.e. the electron and the rubidium ion (see equation equations 2.15 and 2.16). It follows that the final center of mass velocity of the recoil ion is

$$v_{Rb} = \sqrt{\frac{2\Delta E}{m_{Rb}(\frac{m_{Rb}}{m_e} + 1)}}, \tag{5.20}$$

where m_{Rb} is the mass of rubidium and m_e the electron mass. This leads to $v_{Rb} = 2.645$ m/s for the recoil ion. For comparison the mean velocity of atoms trapped

in the magneto-optical trap is on the order of 0.2 m/s. Ionization from the excited state $5P_{3/2}$ leads to $v_{Rb,exc} = 5.5$ m/s.

One color two-photon ionization cross sections of rubidium have been been studied extensively experimentally and theoretically in the literature [107, 108, 109, 99]. It depends in particular on the wavelength due to the occurrence of destructive interference or resonant transition, depending on the ionization path. The wavelength dependence of one-color two-photon ionization for rubidium has been measured by [107].

For the photon energy of the ionization light used in this work, λ =532 nm, a two-photon cross section from the ground state of $\sigma = 2.29(14)\times10^{-49}$ cm^{4}s has been measured in [107] using the trap loss method [110].

5.2 Experimental setup for the photoionization measurements

All measurements reported on in this section are done using the same experimental setup and are based on the non-resonant two-photon ionization of cold rubidium atoms using a pulsed frequency-doubled Nd:YAG laser at 532 nm [111, 112]. The dominant process at these low intensities is non-resonant two-photon ionization from either the ground or the excited state

$$Rb(^2S_{1/2}) + 2h\nu \rightarrow Rb^+(^1S_0) + e^- + \Delta E_1 \quad (5.21)$$

$$Rb(^2P_{3/2}) + 2h\nu \rightarrow Rb^+(^1S_0) + e^- + \Delta E_{\mathrm{exc}}, \quad (5.22)$$

releasing an excess energy of $\Delta E_1 = 0.543$ eV and $\Delta E_{exc} = 2.08$ eV respectively.

The duration of the laser pulses is 10 ns at a repetition rate of 20 Hz. The output power of the laser at 532 nm is 245 mJ which would in our setup ionize 10^5 atoms per laser pulse and would lead to a Coulomb explosion. Since we want to measure the recoil ions' momentum with high precision even a low number of ions per laser pulse would interact on their way to the detector and broaden the measured spectrum. Only one ion per laser pulse is therefore necessary. In order to only have one ion per laser shot typical powers needed are, depending on the laser focus and density in the rubidium target, about 5 orders of magnitude lower than the available laser power. Hence a glass plate is placed right after the output of the pulsed laser, splitting up less than 1 % of the laser light used for the experiment. The main part is dumped in a beam dump. The remaining intensity of the laser beam can be further attenuated using neutral density filters with different optical densities. The laser is placed on a separate optical table and is coupled into the chamber with mirrors. The target is

situated at the center of the recoil ion momentum spectrometer, and can, depending on the experiment, either be the atom beam generated by the 2D MOT or atoms trapped in the 3D MOT. A schematic sketch is depicted in figure 5.4.

The last two mirrors are used to walk the beam and optimize its overlap with the target, leaving it perpendicular to the y- and z-axis of the spectrometer. After the last mirror a lens with focal length f = 400 mm focuses the laser down to a $1/e^2$-diameter of 20 μm at the interaction volume, resulting in a Rayleigh range of z_R = 2.36 mm. This lens is positioned on a single-axis translation stage such that it can be translated along the x-axis of the spectrometer with high precision. Since some of the atom-light interaction described in the following depends on the polarization of the ionization laser, a polarizing beam splitter (PBS) is placed behind the lens, giving a well-defined polarization axis. It is followed by a half-waveplate,

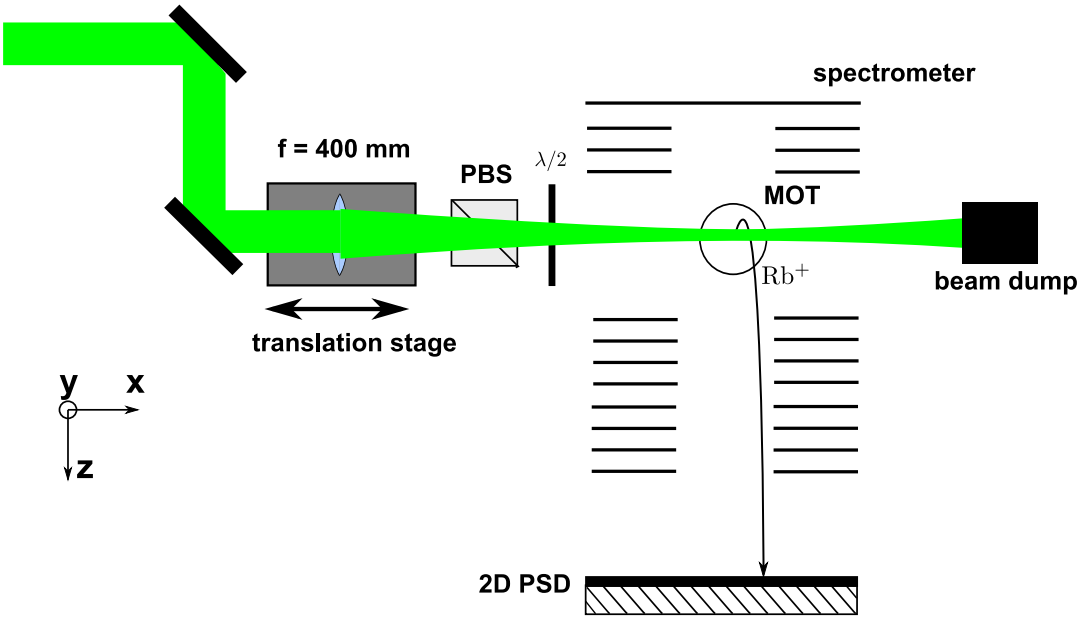

Figure 5.4: Sketch of the experimental setup for the photoionization measurements. A pulsed laser is coupled into the chamber with two mirrors and is focused onto the target atoms (atom beam or 3D MOT) at the center of the recoil ion momentum spectrometer. For best overlap of the laser focus with the target, the focusing lens is positioned on a single-stage translation stage. A polarizing beam splitter (PBS) defines the linear polarization axis of the laser which can be rotated using a half-waveplate. After photoionization, the recoil ions are accelerated towards and detected by a 2 dimensional position sensitive detector (2D PSD) which they reach after a certain time of flight.

such that the polarization axis of the linearly polarized light can be rotated. After ionization the recoil ions are pushed out of the interaction volume by an electric field of 0.28 V/cm which is applied to the electrodes of the spectrometer and accelerated towards the downstream ion detector which consists of a MCP followed by a delay-line anode. Detecting the recoil ion in coincidence with the laser pulse, time of flight and position of the recoil ions can be determined (see section 4.6).

5.3 Using photoionization for characterization of the targets

5.3.1 Density profile of the trapped atoms

In a first experiment the spectrometer setup can be used as a simple ion counter. The pulsed laser photoionizes the trapped atoms which are, as described above, subsequently accelerated towards the ion detector using a weak electric field. The number of ions produced in a certain time is counted. As described in section 4.5, the 3D trap can be operated either in a bright MOT or in a dark SPOT configuration. The standard way to characterize cold atom clouds is absorption imaging [113]. Using this technique we can characterize the trapped atoms in atom number, size, peak density and temperature. From these measurements we deduced an increase of density, depending on the parameters used for the dark SPOT, of up to one order of magnitude. The problem with density measurements in a dense cloud is that the cloud might get optically thick for the absorption beam, leading to an error in the calculation of the peak density in the cloud. An independent measurement of the density profile of the could can be performed using photoionization.

For the density profile measurements the laser focus is scanned through the cold atom cloud along the x-axis of the spectrometer using a translation stage and the ionization rate is measured as a function of the position of the lens. As we saw in section 5.1, this rate is proportional to the interaction volume and the number of atoms in this volume and thus to the density[1]. This means by scanning the laser focus through the cloud, the density profile of the cloud can be measured. Due to the Rayleigh range of the pulsed laser of 2.3 mm, the measured density profile is convoluted with the intensity profile of the ionizing laser. The results for both the bright MOT and the dark SPOT of these scans is shown in figure 5.5 a). The density profile is scanned with a resolution of $x = 1$ mm. The green crosses correspond to

[1]Neglecting the difference in the photoionization rate due to the excited state fraction in the bright MOT (in a dark SPOT most atoms are in the ground state), this rate can be directly compared to the density measurements using absorption imaging.

the ionization rate of the bright MOT, whereas the black circles correspond to the ionization rate measured from a dark SPOT. The red curves are Gaussian functions fitted to the density profiles. The use of a Gaussian fit function for the density profile of the bright MOT is questionable, since within the error bars also a flat top distribution could be fitted at the center of the could, as expected in the density limited regime in the MOT [114]. From the Gaussian fit functions we deduce a maximum rate of 65 Hz from the bright MOT, compared to 351 Hz from the dark SPOT, which corresponds to an increase in rate and thus density of 5.4. The FWHM of the dark SPOT is 9.3 mm and thus slightly larger than the size of the bright MOT, which amounts to a FWHM of 8.6 mm. Since this measurement is convoluted with the intensity distribution of the ionization laser, the FWHMs are overestimated by about 4 %. From the corresponding absorption images for the dataset presented here we expect a peak density of 2.0×10^{10} atoms/cm^3 in the bright MOT, whereas the peak density in the dark SPOT is determined to be 1.2×10^{11} atoms/cm^3, corresponding to an increase in density of a factor of 6 which agrees well with the ionization measurements within the error bars.

5.3.2 Density profile of the atom beam

The technique of photoionization offers a unique tool to characterize the density profile of the atom beam, which is otherwise done by measuring the atom beam fluoresce using a light sheet. This measurement leads to large systematic errors due to the unknown fraction of photons detected.

In the following, only the atom beam is used as a target. To compensate for the reduced density in the atom beam, the intensity in the photoionization laser is increased by a factor of 10. From the ionization measurements of the 3D traps, a density can be deduced from the ion rate. The laser is again scanned through the atom beam along the x-axis of the spectrometer using a translation stage. The results of the scan through the atom beam are shown in figure 5.5 b). Again, the data is fitted with a Gauss function, leading to a maximum rate of 4.1 Hz, which corresponds to a peak density of 1×10^7 cm^{-3}. The FWHM size of the atom beam is 11.18 mm, from which the divergence of the atom beam can be deduced and is determined to be $\alpha = 23.3$ mrad, α being the full opening angle, since the distance from the exit hole to the interaction volume is 480 mm. This divergence corresponds to a transverse temperature in the atom beam of $v_T = 0.19$ m/s, which is on the same order as measured in the 3 dimensional trap.

Next to the determination of the density in the atom beam, this measurement also gives unique insight in the spatial position of the 2D MOT with respect to the 3D MOT and is of great interest for the design of 2D MOTs. As described in

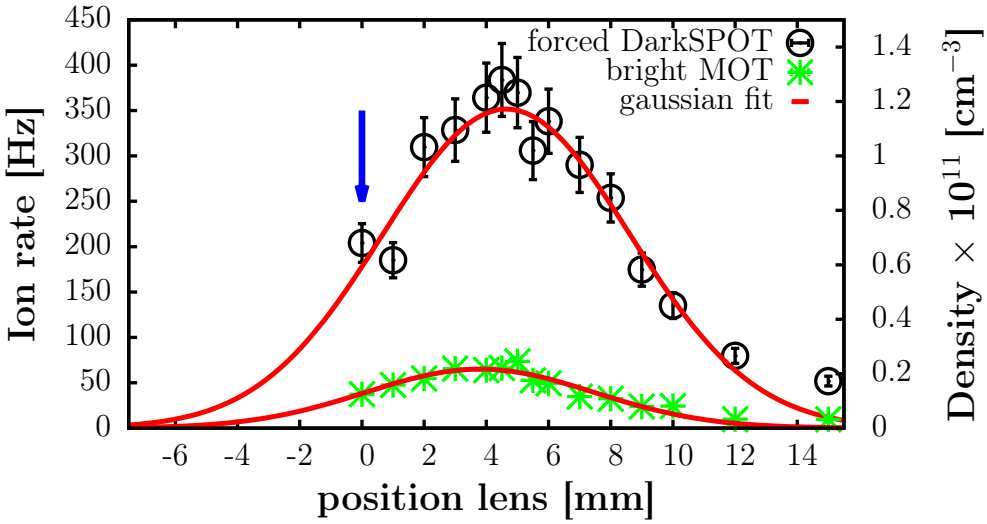

(a) Position dependent photoionization rate of the 3D targets

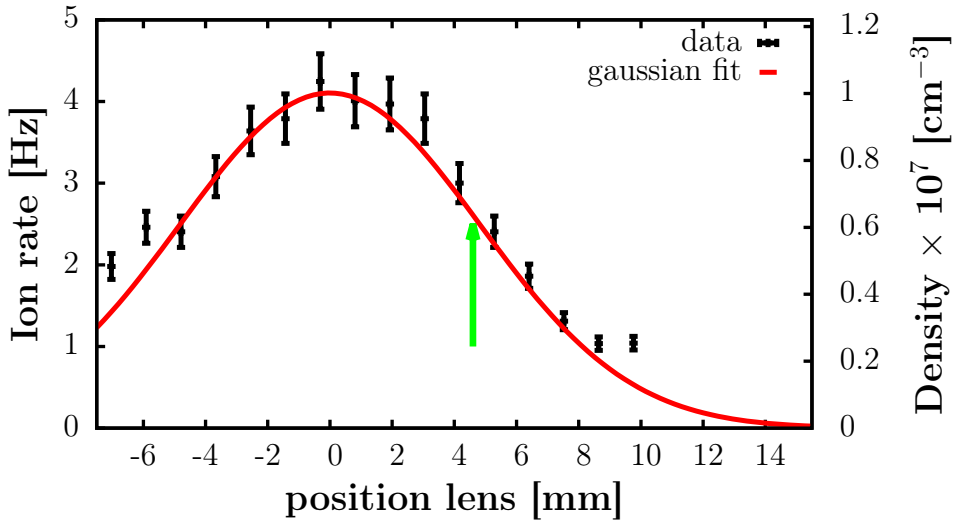

(b) Position dependent photoionization rate of the atom beam

Figure 5.5: Density profile measurement of the atom beam and the dark SPOT and bright MOT convoluted with the intensity profile of the ionizing laser as a function of the position of the ionizing laser (the Rayleigh range of the laser is 2.3 mm). The laser with a focus of 20 μm is scanned through the atom cloud and the atom beam in order to determine the column density profile. The size of the MOT in bright state is 8.6 mm (FWHM), in the dark SPOT 9.3 mm (FWHM) and the size of the atom beam at the interaction volume is 11.2 mm. The arrows indicate the positions of highest density in the atom beam and the 3D MOT respectively. The error bars correspond to the statistical errors.

section 4.4, using a bellow to connect the 2D MOT module to the main chamber, the direction of the atom beam can be changed. With this bellow, the position of the atom beam with respect to the trapping volume and the position of the trapped atoms can be optimized. This is necessary due to the following two reasons: if the atom beam hits the center of the 3D MOT, the relatively warm atoms from the 2D MOT collide with the trapped atoms, leading to a loss in the 3D trap. On the other hand, the atom beam needs enough overlap with the cooling volume to scatter enough photons for being trapped. As we see from the measurements in figure 5.5, the best position of the atom beam is not at the center of the 3D trap, but has been measured to be 4.5 mm away from the center of the 3D trap. The position of the atom beam with respect to the 3D trap is indicated by the blue arrow in figure 5.5 a), whereas the position of the center of the 3D trap is indicated by the green arrow in figure 5.5 b).

5.3.3 Velocity distribution of the atom beam

State of the art characterization of atom beams generated by 2D MOTs is done by detecting the fluorescence by shining in resonant laser light onto the atom beam. Velocity characterization can be done using a time of flight method, where the 2D MOT is periodically switched off and the decay of the fluorescence is measured as a function of time [87, 86]. The decay of the fluorescence signal gives a time of flight distribution, which can be transformed into the longitudinal velocity distribution of the atom beam. This method has been used to characterize our 2D MOT prior to its implementation in the MOTRIMS setup and the details of it can be found in the diploma thesis of B. Höltkemeier [86].

We want to use the same principle using photoionization measurements, which gives us an independent measurement on the velocity distribution of the atom beam and can be compared to the results obtained from the fluorescence measurements from [86]. The ion rate is now measured as a function of time after switching off the 2D MOT. We therefor use the signal of a laser pulse to trigger the experiment. A fast photodiode (EOT, 23-2397A) picks up a signal from the pulsed laser. This signal is discriminated and triggers a pulse generator (Quantum Composer, 9520), which is used to switch off the AOMs of the lasers of the 2D MOT a variable delay Δt prior to the ionization process. Furthermore, a second signal from the pulse generator is delayed by the time of flight of the recoil ions in the spectrometer and drift tube and is used to gate the MCP back signal, such that only ions are recorded which are ionized from the laser pulse. By changing the delay Δt, the velocity distribution of the atom beam is scanned. Special care has to be taken, since the time of flight of the atom beam is about 40 ms, whereas the repetition rate of the laser is 20 Hz,

e.g. the time difference between the pulses is 50 ms. In order to ensure that also the slowest atoms have reached the detection region before the atom beam is switched back on, only every fifth laser pulse is used to trigger the experiment. The ion rate is now measured as a function of the delay Δt.

The laser settings for the 2D MOT are adjusted to the ones used in the fluorescence measurements, i.e. total power in the cooling beams is $P_{\text{cooler}} = 124\,\text{mW}$ at a detuning of δ = -12 MHz, and 6.6 mW in the repumping beams. The pushing beam carries a power of 0.9 mW at a detuning of $-40\,\text{MHz}$. The results of these measurements are shown in Fig. 5.6. The solid line is an interpolation of the data points taken using the photoionization time of flight measurements. The dashed line is the fluorescence signal. The data has been scaled to the same area under the curves. The deduced velocity distributions from the two independent measurements agree well. The mean longitudinal velocity is 13.6 m/s with a FWHM velocity spread of 3.5 m/s, which corresponds to 0.25 a.u..

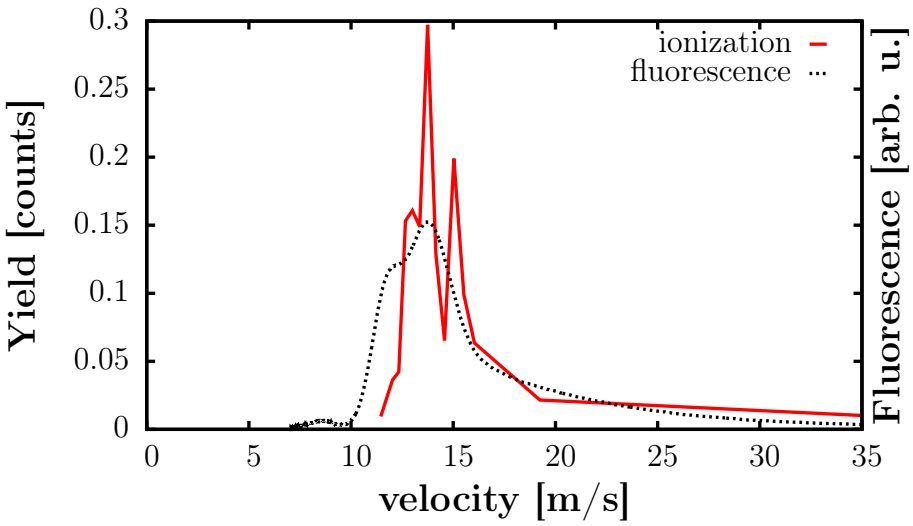

Figure 5.6: Measured velocity distribution of the atom beam using a time of flight method, where the number of atoms in the beam is determined as a function of time after the 2D MOT has been switched off. The solid curve is an interpolation of the TOF measurements ionizing the atoms from the atom beam. The dashed curve is the fluorescence measurements (from [86]). The data has been scaled such that the area under the curve is the same. The mean velocity is 13.6 m/s with a FWHM velocity spread of 3.5 m/s.

5.4 Characterization of the recoil ion momentum spectrometer

We want to use the recoil ions' momentum after photoionization to characterize the RIMS. Therefor the momentum of the recoil ions is measured by detecting the recoil ions' time of flight and position. As we saw in section 4.6 time and position focusing of the recoil ions in the spectrometer is obtained by including an electrical lens in the electric field configuration. One plate is set to an independent voltage such that the spectrometer consists of one field region for extracting the recoil ions, and one for focusing the recoil ions.

For the ionization process several considerations need to be taken into account: The target should be in a well defined initial state, which can be achieved by switching off the cooling lasers prior to the ionization process. Furthermore, space charge effects need to be avoided in the experiments, since this would lead to a broadening of the measured spectra. Also, detection of the position of the recoil ion using the delay-line is only possible for detection of single hits. Therefore the intensity in the laser pulse should be attenuated such that only one ion per laser pulse is produced. Furthermore the magnetic trapping field should be switched off in order to obtain best resolution. The experiment can thus not be operated in continuous mode any more.

From equation 5.22 we can deduce that ionization of ground state atoms using 532 nm light results in a center-of-mass momentum of the recoil ion of 0.1885 a.u., which corresponds to a center-of-mass velocity of 2.6 m/s. The velocity of the atoms in the trap, at a typical temperature of 200 μK, yields to a momentum spread of 0.017 a.u., whereas the longitudinal velocity spread in the atom beam is on the order of 3.5 m/s (FWHM), corresponding to 0.25 a.u.. The experiment is thus performed using 3 dimensionally trapped atoms. Using linearly polarized light the ejected electrons are most probably ejected along the polarization axis of the laser (see section 5.1) leaving the recoil ions with a momentum kick in opposite direction. The momentum of the recoil ion can be measured using the recoil ion momentum spectrometer and can be used to calibrate and characterize the spectrometer. The polarization axis of the ionizing laser can either be parallel to the time of flight axis[2], leading to recoil ions with momenta transferred and detected along the time of flight, or can be rotated such that it is parallel to the y-axis of the spectrometer and the recoil ions then hit the detector at different Y-positions.

[2]In order not to confuse the reader the momenta parallel to the polarization axis of the laser are not called longitudinal momenta as it is usually done in the literature, but transverse,y/tof, such that it is consistent with the notation throughout the thesis.

5.4.1 Timings and data acquisition

In RIMS, the three-dimensional information on the momentum transferred to the recoil ion is obtained from the position where the ions hit the detector and their time of flight (see section 2.2.1). In the experiment this information is gained using a delay-line anode, where spatial information is obtained from the arrival times of signal induced on the delay-line with respect to an initial trigger. The ions hitting the MCP induce voltage spikes in the delay-line, which are coupled out capacitively and are preamplified, before passing a constant fraction discriminator (CFD), giving out a logic NIM signal. The ion signal from the MCP triggers the internal clock of a time-to-digital converter (TDC). The signals from the delay-line anode are sent to the TDC as stops. Time of flight information is obtained from a logic signal generated by the laser pulse, which is delayed in time by a constant delay such that it always reaches the TDC after it has been triggered and is used as a fifth stop. An overview of the data acquisition used in the experiment is shown in figure 5.7. The raw data from the TDC is read out by a personal computer, stored in its memory and written down as .root file [3] once the measurement is finished.

The whole experiment is triggered by the repetition rate of the pulsed laser. The trigger from a laser pulse is obtained by detecting a small amount of the laser pulse with a fast photodiode (EOT, 23-2397A) which is subsequently discriminated. The discriminator gives out a logic TTL signal, which triggers a pulse generator (Quantum Composer, 9520). This pulse generator delays the signal and gives out three pulses: the trigger for the experimental control which switches off the MOT[4], two signals which are delayed by the time of flight of the ions in the drift tube, one used for the fifth stop in order to obtain the time of flight information, and one which is used as a gate for the MCP back signal. This gate suppresses background in the measurements. Since the background in the experiment is low, typically 20 Hz coming from ions produced in the MOT and dark counts of the MCP, the gate is usually set to 2.2 μs. In background measurements it has been verified that no background ions are recorded in this time window. Thus only events originating from the laser pulse trigger a measurement.

The switching scheme is shown in figure 5.8. The whole experimental sequence is synchronized to the pulsed laser. The magnetic trapping field coils are switched off 1.18 ms prior to the atom-photon interaction such that no eddy currents are present during photoionization. In order to avoid optical pumping when switching off the trapping field, the trapping light of the 3D trap is switched off simultaneously. The

[3] For more details please refer to http://root.cern.ch/root/InputOutput.html

[4] The experimental control could not be used instead of the pulse generator due to its insufficient time resolution of 10 ns.

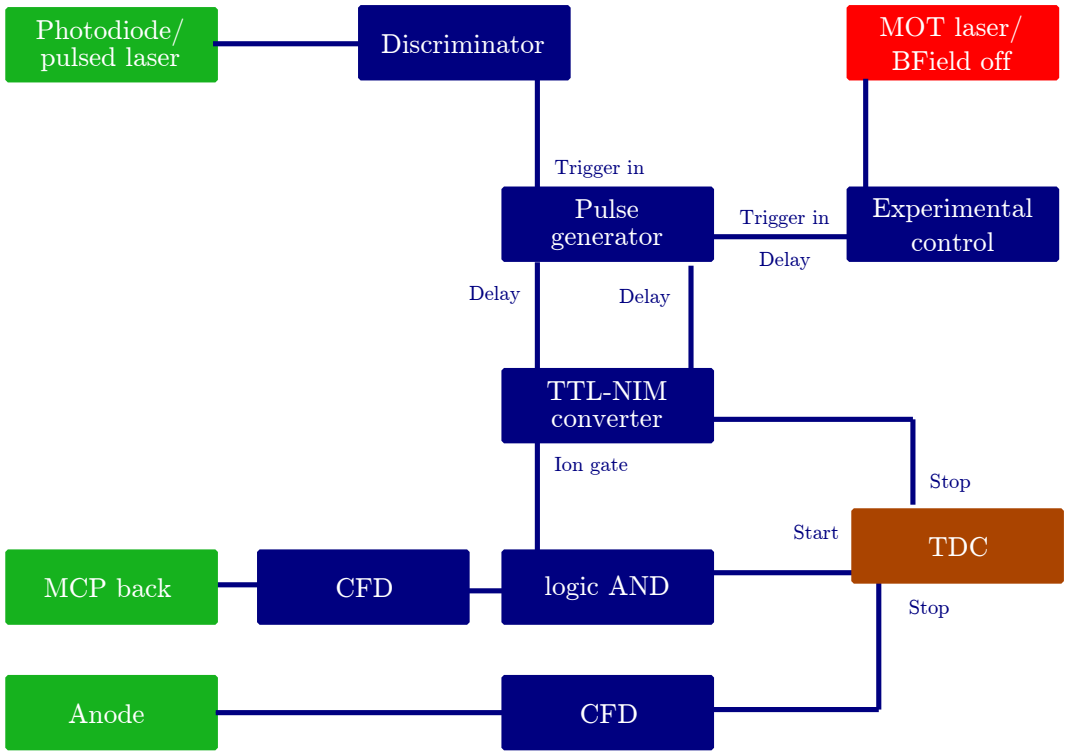

Figure 5.7: Data aquisition for photoionization measurements. The pulsed laser triggers the whole sequence. A signal from the laser pulse is discriminated and used to trigger a pulse generator. One output of the pulse generator is used to trigger the experimental control, switching off the magnetic trapping field and the 3D MOT lasers prior to ionization. The ion signals are coupled out from the MCP back and the delay-line anode capacitively and are discriminated using CFDs (Constant Fraction Discriminators). The MCP back signal is gated with another delayed signal from the pulse generator and starts the TDC, such that only photoionized ions are recorded. Position information on the recoil ions is obtained from the delay-line anode while time of flight information is obtained from the time difference between the laser pulse and the ion hitting the MCP.

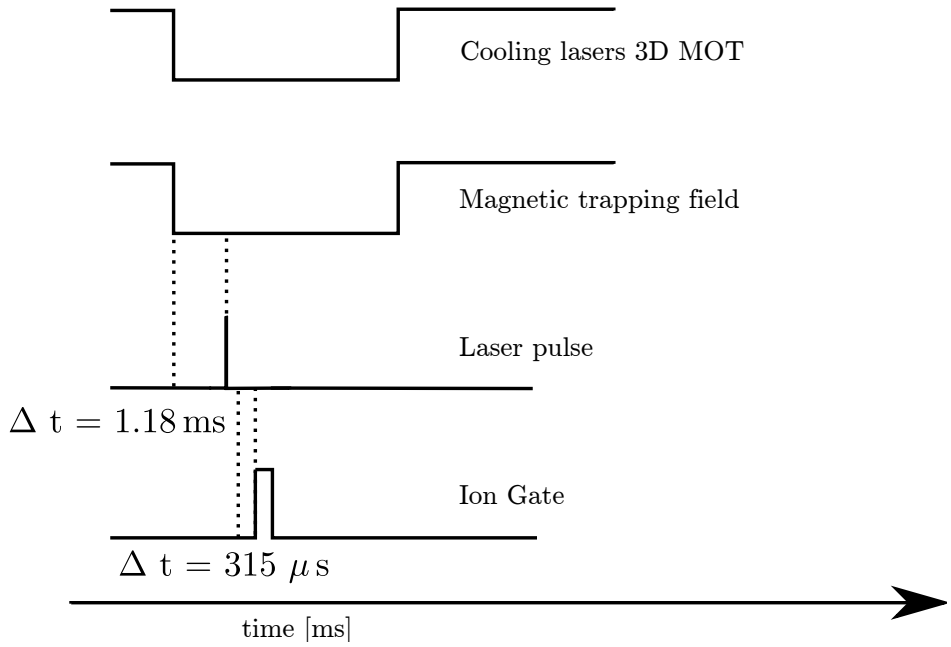

Figure 5.8: Timings for the photoionization measurements in pulsed mode. A delayed signal from the pulsed laser is used to trigger the experiment. The cooling lasers and magnetic trapping field are switched off 1.18 ms before ionization, such that all eddy currents have vanished. The ion gate is used to gate the MCP back signal 315 μs after the ionization pulse, which corresponds to the time of flight of the ions in the drift tube.

ion gate is delayed by the time of flight of the ions in the dirft tube and is typically 315 μs.

5.4.2 Simulations of the real detector

Opposed to the optimized resolution of the detector, all data in this thesis were taken connecting the focusing voltage U_f to plate 16 instead of plate 14. In order to analyze it's effect on the resolution, investigation of the optimal focusing voltages and focal plane are repeated (see section 4.6) with simulations using SimION. Changing the ratio $U_\mathrm{P}/U_\mathrm{f}$ the focal planes in TOF and position are determined. The results are shown in Fig 5.9. From the simulations we see that the optimal focal plane is shifted by 20 mm to 856 mm, at now a ratio of $U_\mathrm{P}/U_\mathrm{f} = 1.425$. In the experiment the focal plane, corresponding to the position of the detector, cannot be moved, such that either the time of flight or position can be optimized.

Using $U_\mathrm{P}/U_\mathrm{f} = 1.39$ and $\mathrm{U_P} = 5$ V, which corresponds to the ratio optimized in

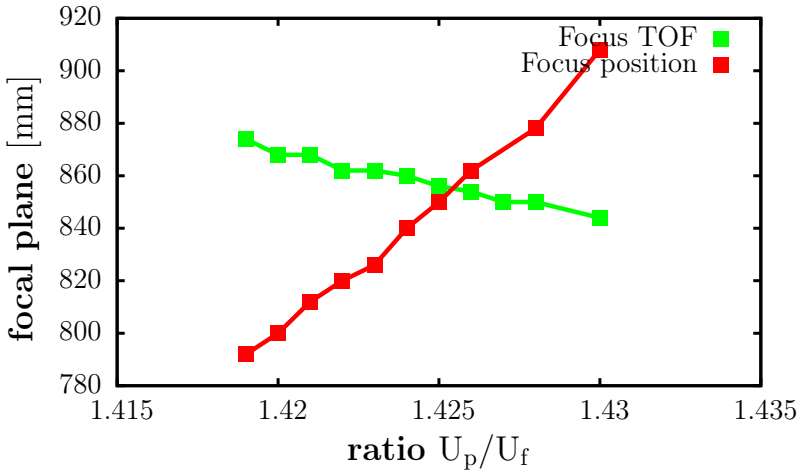

Figure 5.9: Simulation of the focal planes for time of flight and position focusing for the current configuration of the spectrometer. By changing the ratio of the pushing and the focusing voltage, the focal planes in TOF and position are determined.

the experiment, the focusing capabilities of the spectrometer are shown in figure 5.10. Ions without any momentum would hit the detector at the center after a time of flight of 312.15 μs. Applying an initial momentum of $p_{TOF} = 0.18$ a.u. to the recoil ion along the time of flight axis leads to a difference in time of flight of $\delta t = 107$ ns. Recoil ions with the same initial momentum along the y-axis of the spectrometer will be projected at Y = 0.96 mm outside the center of the detector after the same time of flight as the ones without any initial momentum. Initially, 1000 ions were distributed on a sphere with a diameter of 1 mm at the collision region of the spectrometer. From this graph it can be seen that in the current configuration of the spectrometer the focusing capabilities are expected to be better in space than in time.

5.4.3 Experimental results

The spectrometer is characterized using photoionization measurements of rubidium ground state atoms. The laser beam profile of the pulsed laser is not a perfect TEM00 mode such the focus, using a lens with focal length f = 400 mm, leads not as expected to a waist of 7.5 μm, but instead to a waist of 20 μm and a corresponding Rayleigh range of $z_R = 2.3$ mm. As described above the polarization axis of the ionizing laser can be rotated such that the initial recoil ion distribution can be altered and the recoil ion momentum spectrometer can be characterized in its time of flight as well as in its spatial behavior.

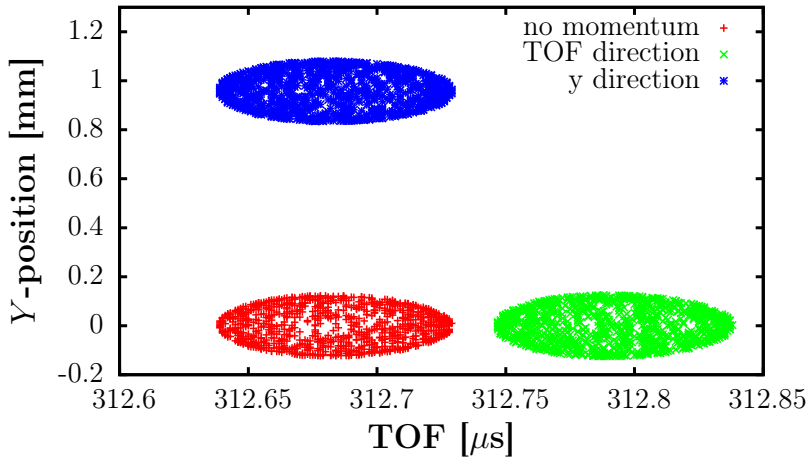

Figure 5.10: Simulated ion distribution on the detector plane. Ions starting from a spherical distribution with 1 mm diameter are focused in space and time onto the detector plane. An initial momentum kick of 0.1862 a.u. parallel to the TOF axis of the spectrometer results in a difference in TOF of $\delta t = 107\,\text{ns}$, whereas ions with the same initial momentum along the y-axis of the spectrometer hit the detector 0.96 mm away from the center.

In the experiment, plate 11, corresponding to the position of the collision region, is set to mass by an electrical connection of the plate to the chamber, such that the influence of electric stray fields from the surrounding is minimized. The voltage difference is still set to roughly about 5 V, such that the pusher plate is set to U_P = 0.985 V and the drift tube is set to U_{Drift} = -4.0 V. The focusing voltage can be set independently to a voltage and is optimized during the experiment for best resolution which is found for U_F = -0.39 V. No big effect of the focusing voltage is observed on the spatial resolution. This might either be due to the fact that the collision region is forced on mass by the electric contact to the surrounding chamber, such that changing the focusing voltage only has a minor effect because the electric field in the main region of the spectrometer head (from the pusher plate to the collision region) is not changed when changing the focusing voltage, or due to electric stray fields from the surrounding chamber which limit the resolution of the spectrometer at these low electric fields of only 0.28 V/cm. The influence of stray electric fields could be investigated by increasing the extraction field and see if the resolution increases. However, due to the very small distance at which the ions hit the detector already at these low fields, this cannot be investigated measuring the ions' recoil from photoionization experiments. A larger recoil momentum like e.g. in ion-atom collisions is needed.

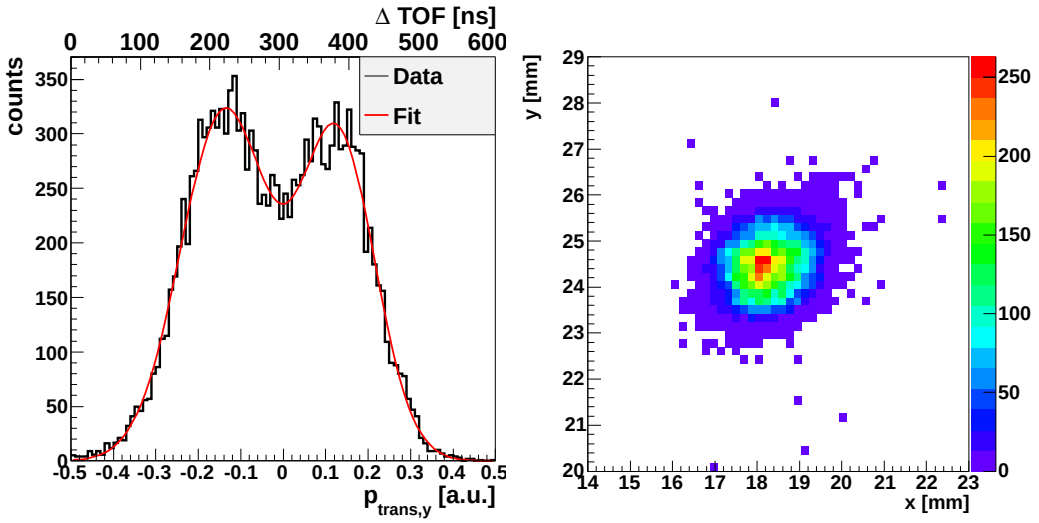

(a) Time of flight distribution **(b)** Raw detector image

Figure 5.11: Time of flight distribution of photoionized recoil ions. The ionization laser is polarized parallel to the time of flight axis of the spectrometer. Due to the recoil momentum of the ejected electrons the recoil ions start with an initial transverse momentum of $p_{trans} = 0.18$ a.u. either along or opposite the time of flight direction. The FWHM of the time of flight distribution is 0.2 a.u. and gives an upper limit for the achievable resolution. The recoil ions hit the detector in one spot.

The measured recoil ion momentum spectra for photoionization with the pulsed laser, the polarization axis of the laser beam being parallel to the time of flight axis, is shown in figure 5.11. The recoil ions with different directions have a difference in time of flight of 224 ns, which corresponds to a difference in momentum transferred to the recoil ion of $p_{trans} = 2 \times 0.18$ a.u. Thus the calibration factor in time of flight axis is 0.00168 a.u./ns. The upper limit for the achievable resolution along the time of flight axis can be obtained by fitting a Gaussian function to the wings of the time of flight distribution. This results in an upper limit of 0.2 a.u. (FWHM).

Rotating the polarization axis of the ionizing laser such that it is parallel to the y-axis of the spectrometer leads to a transverse momentum component of the recoil ions along the y-axis of the spectrometer. As shown in figure 5.12 the time of flight distribution now only shows a single peak, while the recoil ion distribution on the xy-plane of the detector shows two peaks, as expected. For this data set the difference in position of these two peaks along the y-axis is 0.96 mm, leading to a conversion factor of 0.39 a.u./mm. Note that from the simulations presented above where the resolution of the detector has not been included we would expect twice

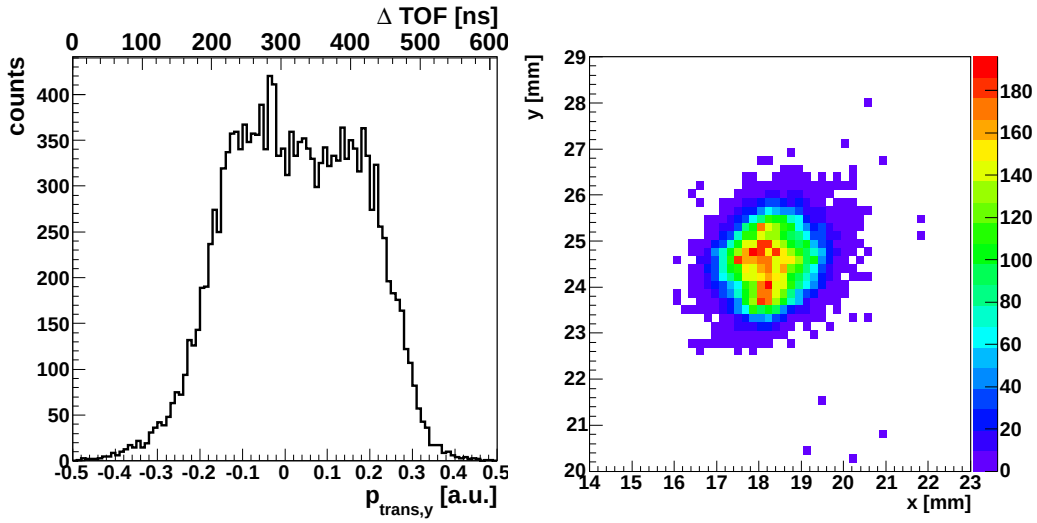

(a) Time of flight distribution **(b)** Raw detector image

Figure 5.12: Time of flight and spatial distribution for recoil ions originating from photoionization with a laser polarized along the y-axis of the spectrometer. Due to the polarization of the laser the recoil ions have an initial momentum component along the y-axis. The time of flight distribution only shows one peak, while the spatial distribution on the detector shows two peaks along the y-axis.

the measured distance. Projecting the recoil ion distribution on the y-axis and again fitting a Gaussian distribution to the projection leads to an upper bound in spatial resolution of the spectrometer of 0.37 a.u.. Thus, opposite to what is expected from the simulations, the resolution in time of flight is a factor of two better than in y-direction.

5.4.4 Angular distribution of photoionized recoil ions

Photoionization leads to an angular distribution of the ejected electrons, and thus the recoil ions, following a Legendre distribution. The angular distribution can be deduced from the transverse momentum components of the recoil ions. Depending on the polarization axis of the ionizing laser the recoil ions are ejected along the time of flight or the y-axis of the spectrometer, resulting in a dipole like distribution. In the transverse momentum distribution this should result in two peaks either along the time of flight axis or along the Y-component.

The measured transverse momentum distributions of the photoionized recoil ions, with polarization axis along the time of flight axis and the y-axis, respectively, are

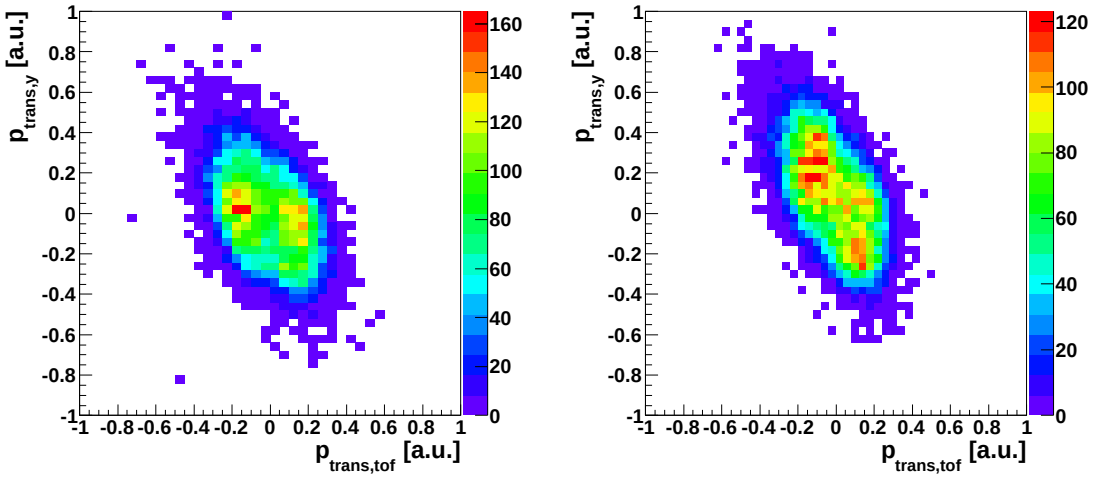

(a) Polarization axis parallel to tof direction.

(b) Polarization axis parallel the y-axis.

Figure 5.13: Transverse momentum distribution of photoionized recoil ions. The distributions reflect the dipole like character of the photoionization process. Opposite to what is expected, rotating the polarization axis of the ionization laser by 90° does not lead to a rotation of 90° in the transverse momentum distribution. The ions having different trajectories in the spectrometer have a different time of flight.

shown in figure 5.13. They reflect the dipole like character of the photoionization process. The spectrum should be rotated by 90° when the polarization of the ionization laser is rotated. The measured transverse distribution of the recoil ions is shown in figure 5.13 b). The polarization axis is parallel to the y-axis of the spectrometer, which means that both peaks should have the same momentum in time of flight direction. This is not the case, the two peaks show a difference in time of flight of about 300 ns. SimION simulations show that even for ions starting up to 1 cm away from the symmetry axis of the spectrometer or away from the collision area, the ions still hit the detector after the same time of flight. We thus exclude the possible that this difference in time of flight is due to the position of the target in the spectrometer, which is in the experiment some mm away from the simulated position.

One explanation for the difference in time of flight in the two peaks we observe might be electric or magnetic stray fields. This possibility is investigated using an analytical model for the spectrometer: At the detector, these two peaks only have a distance of 1 mm which can also be assumed to be the upper limit for the distance of the different ion trajectories inside the spectrometer. This means that the fields

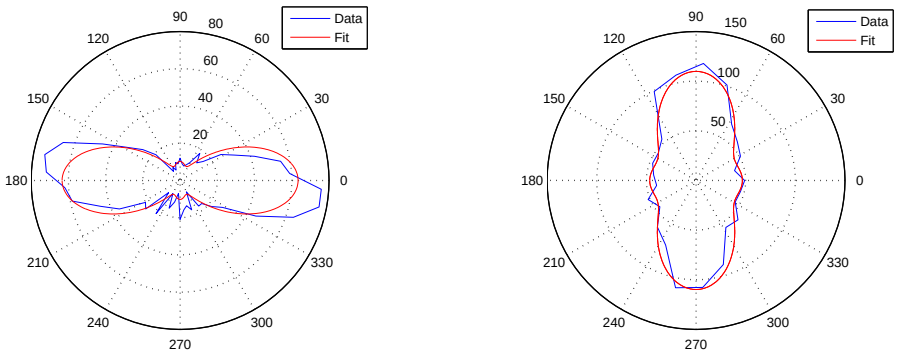

(a) **(b)**

Figure 5.14: Angular distribution of the recoil ions obtained from photoionization, reflecting the dipole like characteristics of the ionization process. In (a) the polarization axis of the laser is parallel to the time of flight axis. In (b) the polarization axis of the ionization laser has been rotated by 90°, leading to a rotation of the ejected electrons and thus recoil ions. The blue curve is an interpolation of the data points, the red curve is a fit using eq. 5.24 to the data.

have to differ on this small length scale. We estimated that for a time difference of 300 ns at the detector a magnetic field gradient on the order of 10 G/cm or an electric field difference of $\Delta E = 0.0002$ V/cm would be needed. Both of these gradients do not seem realistic. The magnetic fields outside the ultrahigh vacuum chamber have been probed with a Hall probe and only fields in the range of the earth magnetic field could be detected. Therefore, the origin of this nonlinearity cannot be explained by stray fields and its source is still under investigation.

The upper limit for the spatial resolution of the spectrometer has been obtained from projection of the data onto the y-axis. The non linearity in the time of flight we observe for different trajectories along the y-axis of the spectrometer leads to a broadening of the projected data and could thus explain the poor spatial resolution compared to the resolution in the time of flight direction.

Calling the angle between the $p_{trans,tof}$ and $p_{trans,y}$ axis θ, one obtains the angular distribution of the recoil ions. The polar plots of these results are shown in figure 5.14. The angular recoil ion distribution for the polarization along the y-axis is taken from a projection on the xy-plane (see fig 5.12 b)) instead of the $TOF - y$-plane where the already discussed non linearity dominates the distribution. Due to the cylindrical symmetry of the spectrometer in the xy-direction this substitution of the axis is justified. The blue curve is an interpolation of the data points, while

the red curve is a fit to the data using equation 5.24. Since the ionization process is a two-photon process the anisotropy parameter up to second order needs to be included.

The measured spectra of the recoil ions are convoluted with the resolution of the spectrometer. Due to the difference in resolution along the two transverse momentum components in the spectrometer, the angular distribution does not agree, leading to different values for the anisotropy parameters. From figure 5.14 a), $\beta_2 = 1.6$ and $\beta_4 = 1.04$ is obtained, whereas from figure 5.14 b) $\beta_2 = 0.6$ and $\beta_4 = 0.4$ is obtained due to the reduced spatial resolution of the spectrometer.

5.4.5 Simulated recoil ion distribution

Simulations of the measured ion distribution have been performed using SimIon. The initial ion distribution is given by the spatial and temporal shape of the ionization laser used in the experiment convoluted with the spatial atom distribution in the MOT. The initial spatial ion distribution in y-and TOF-direction is given by the square of a Gaussian distribution with $\sigma_{laser} = \sigma_y = \sigma_{TOF} = 20$ μm since it is a two-photon process and the ionization probability is thus given by the square of the intensity distribution of the laser. In x-direction the ion distribution is given by the square of the laser's intensity distribution, $I(x)^2$, convoluted with the spatial distribution of the 3D MOT ρ_x and reads [5]:

$$R(x) = \rho_x \cdot I(x)^2. \tag{5.23}$$

The temporal shape of the initial distribution follows the temporal shape of the laser pulse, which is a Gaussian pulse with FWHM of 10 ns. Furthermore, the ion distribution obtained from a photoionization process has an angular distribution described by Legendre polynomials and the differential cross section reads (see section 5.1.2 for more detail):

$$\frac{\mathrm{d}\sigma^{(N)}}{\mathrm{d}\Omega} = \frac{\sigma_{\mathrm{total}}}{4\pi} \sum_{j=0}^{N} \beta_{2j} P_{2j}(cos(\theta)). \tag{5.24}$$

For the following simulations 1000 ions with an angular distribution following a random Legendre distribution and with the anisotropy parameters obtained from the experiment are used ($\beta_1 = 1.6$ and $\beta_4 = 1$). The corresponding angular distributions are shown in figure 5.15.

[5] The density distribution of the MOT follows a Gaussian distribution, whereas $I(x) = \frac{I_0}{1+(x/z_{\mathrm{R}})^2}$.

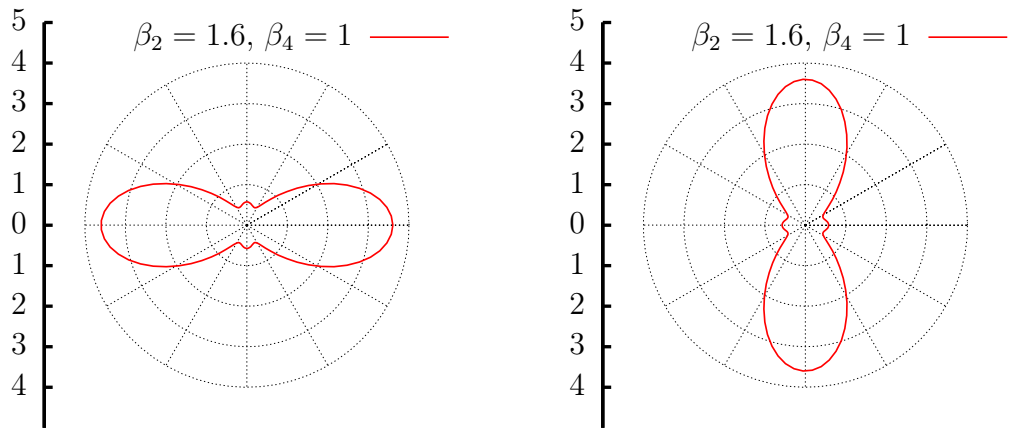

Figure 5.15: Polar plot of the initial angular ion distribution used for the simulations. The polarization axis of the ionizing laser is set parallel to the time of flight axis (a). Setting the polarization axis parallel to the y-axis of the spectrometer rotates the recoil ion distribution by 90° (b).

The simulations are done using the same electric field configuration as have been used in the experiment, i.e. the pusher plate is set to U_P = 0.985 V, plate 11 is forced on mass, plate 16, the focusing plate is set to U_F = -0.39 V and the drift tube is set to U_D = -4.0149 V. This corresponds to a ratio U_P/U_F = 1.39. The data obtained from the simulations are convoluted with the measured resolution of the detector, i.e. σ_{TOF} = 0.04 μs and $\sigma_{\mathrm{x}} = \sigma_{\mathrm{y}}$ = 0.47 mm.

The results of the simulations with the laser polarization along the time of flight axis are shown in figure 5.16. The recoil ions have, due to the momentum transferred either along or opposite the time of flight axis, a difference in time of light of Δtof = 200 ns (figure 5.16 a)), while they hit the detector in the same spatial spot (5.16 b),). The simulations thus agree well with the the experiment in which we measure Δtof = 190 ns. Rotating the polarization axis of the laser such that it is parallel to the y-axis of the spectrometer now leads to the same time of flight of all recoil ions (figure 5.17 a), while the initial momentum component in y-direction leads to a difference in position of Δy = 1.4 mm in this direction where the ions hit the detector (see figure 5.17 b) and the Y-component is now proportional to the transverse momentum component along the y-axis. In the experiment we measured

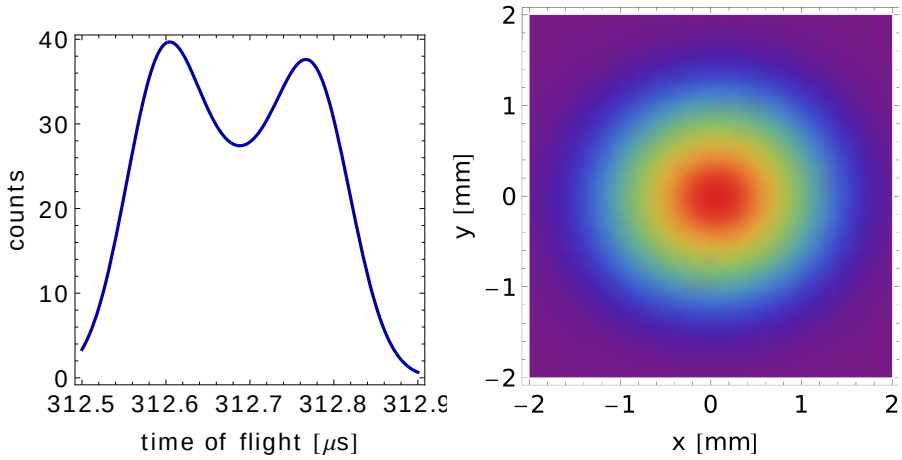

(a) Time of flight distribution. **(b)** Detector image

Figure 5.16: Simulated ion distribution for polarization of the ionizating laser along the time of flight axis convoluted with the resolution of the detector. Due to the momentum of the ejected electrons along the time of flight axis the recoil ions hit the detector with a difference in time of flight of 200 ns.

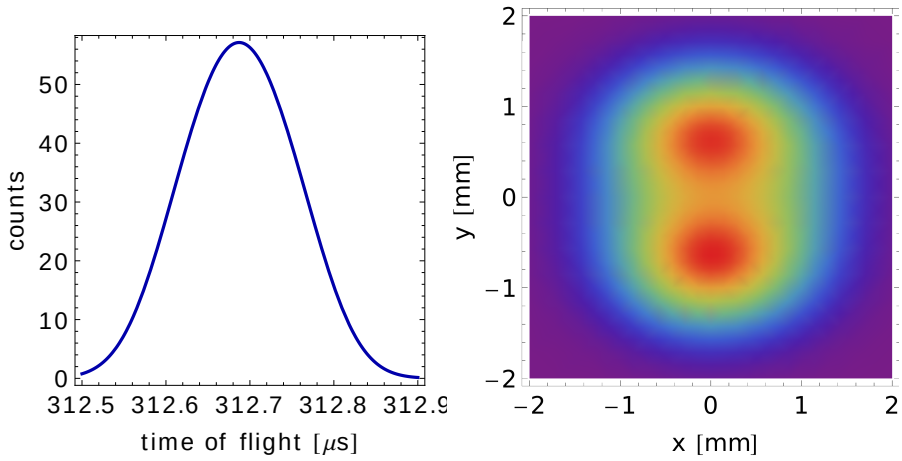

(a) Time of flight distribution. **(b)** Detector image

Figure 5.17: Simulated ion distribution for polarization of the ionizating laser along the y-axis of the spectrometer, convoluted with the resolution of the detector. Due to the recoil ion momentum ions hit the detector at $\delta Y = 1.4$ mm.

$\Delta y = 0.8 \pm 0.2$ mm and is thus smaller than in the simulation. As compared to the simulations of a spherical initial ion distribution, where the resolution of the spectrometer have been neglected, the peaks in time of flight and position are move closer to each other due to the reduced resolution.

5.4.6 Ionizing from the excited state

Leaving the repumping and cooling laser of the 3D trap during the ionization measurement on leads to two-photon ionization of atoms not only from the ground state, but also from the excited state:

$$Rb(^2P_{3/2}) + 2h\nu \rightarrow Rb^+(^1S_0) + e^- + \Delta E_{exc}\,. \tag{5.25}$$

The ionization energy from the excited state is $E_{\text{ion}} = 2.58\,\text{eV}$ so that at the wavelength of $\lambda = 532\,\text{nm}$ two photons are necessary for ionization. This leads to an excess energy of $E_{exc} = 2.063\,\text{eV}$, imparting a momentum of 0.39 a.u. on the recoil ions. The corresponding time of flight spectrum is shown in Fig. 5.18. The spectrometer behaves linearly over this energy range. The ionization rate from the excited state is lower than ionization from the ground state because only about 30 % of the atoms are in the excited state.

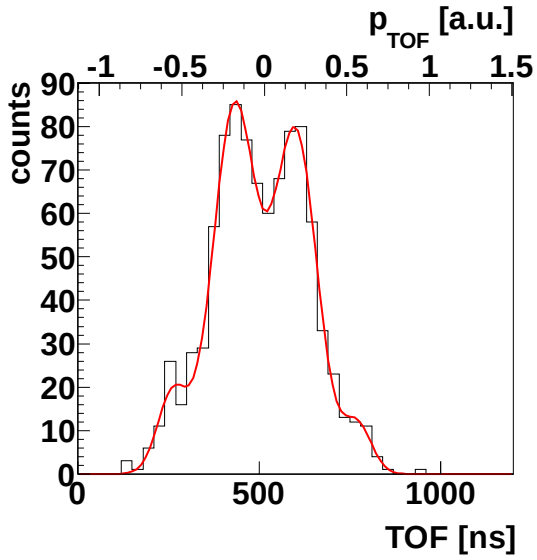

Figure 5.18: Time of flight distribution for ionization from the ground as well as the excited state. Ionization from the excited state results in a recoil of 0.39 a.u. and can be detected in the TOF spectrum as separate peaks.

5.5 Characterizing RIMS using the velocity distribution of an atom beam

The velocity distribution in the atom beam generated by the 2D MOT can be used to calibrate the spectrometer on a larger area than using the recoil ions from photoionization[6]. Therefor the atoms from the atom beam are photoionized and the recoil ions are used to detect the velocity distribution. Since the atom beam propagates almost parallel to the y-axis of the spectrometer, the projection of the measured recoil ion distribution on the y-axis of the spectrometer is, including corrections for the angles of the atom beam with respect to the x- and y-axis of the spectrometer, proportional to the velocity distribution. As we saw in section 5.4, the recoil ions get a momentum of $p_{trans} = 0.18$ a.u. during the ionization process, which corresponds to a velocity of $v_{Rb} = 2.6$ m/s. Typical longitudinal velocity spreads in our atom beam generated from the 2D MOT are 3.5 m/s, such that the momentum of the recoil ion originating from the photoionization process can be neglected in these measurements and the measured transverse momentum component only originates from the initial temperature of the target.

The detector image of the recoiling ions from atom beam is shown in figure 5.19 for two different configurations of the 2D MOT, one for an atom beam originating from the 2D MOT without an additional pushing beam (a) and one with a pushing beam (b) [7]. For comparison, the detector image for recoil ions photoionized from a 3D MOT are shown in figure 5.19 (c). Due to the low recoil momentum of the ions originating from the 3D MOT, the y-position of the 3D MOT on the detector is used to define the zero momentum position on the detector. The velocity distribution of the atom beam is known from independent fluorescence measurements performed in [86]. These fluorescence measurements are used for calibration of the spectrometer in the range 0-35 m/s by assuming a linear dependence between the position of the recoil ions hitting the detector and the velocity of the recoil ion. We optimize the calibration such that best agreement of the RIMS measurement is obtained with the fluorescence measurement[8]. For the data set with pushing beam this leads to a calibration factor of $6.6\ ^{1.24}_{-0.7}$ m/s per mm on the detector. From the data without the pushing beam we obtain a factor of $6.24\ ^{+0.8}_{-0.8}$ m/s per mm. Both calibration factors thus agree within the error bars and are shown, together with the calibration factor obtained from the photoionization measurement (red data point) in figure 5.20. The

[6] The momentum transferred during photoionization corresponds to 2×0.1862 a.u. $= 5.2$ m/s while the atom beam has velocity components up to 30 m/s.

[7] Including a pushing beam leads to lower longitudinal velocities and higher atomic flux in the atom beam

[8] For the optimization the area under the curves is normalized to 1.

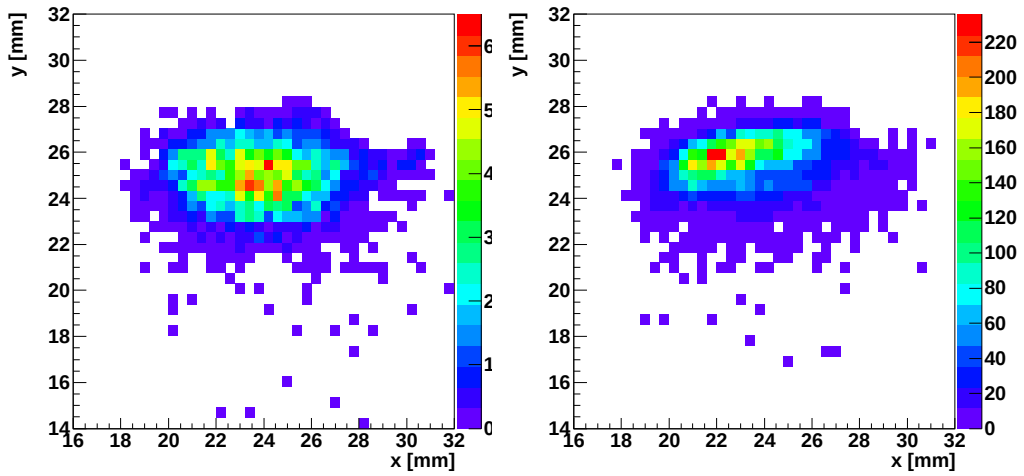

(a) No pusher **(b)** Pusher detuning at - 40 MHz

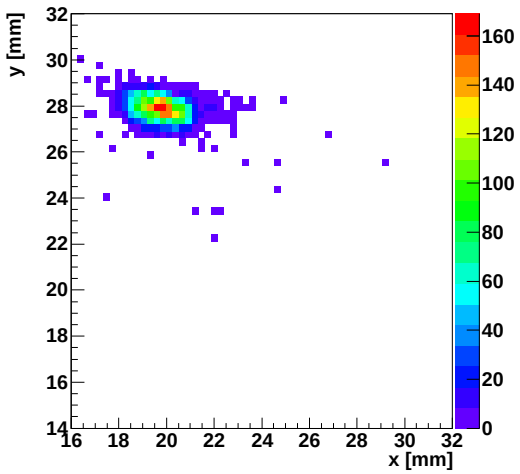

(c) Recoil ions originating from a MOT

Figure 5.19: Detector image of recoil ions originating from photoionization of atoms from the atom beam. Due to the geometry of the setup, the Y-position of the recoil ions is proportional to the longitudinal momentum component of the atom beam. Projection of the spectrum on the y-axis thus leads to the velocity distribution in the atom beam. In a) an atom beam generated in a 2D MOT without a pushing beam is used as a target for the photoionization, in b) the 2D MOT is operated with pushing beam. In c) photoionization from a 3D MOT is shown, which can be used to determine the position corresponding to zero momentum on the detector.

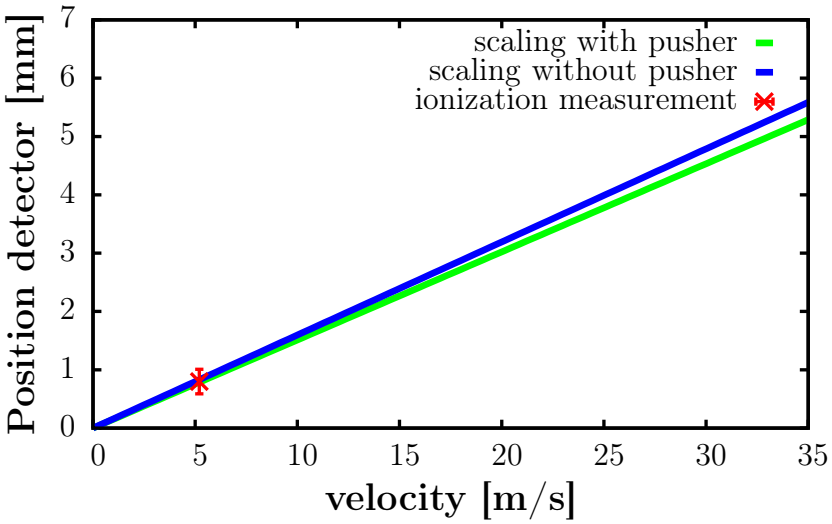

Figure 5.20: Calibration of RIMS using the velocity distribution of the atom beam, corrected for the angle of the atom beam with respect to the y-axis of the spectrometer. The calibration factors are obtained for the atom beam generated with (green) and without the pushing beam (blue). They agree within the errors (see text). The calibration of the detector obtained from the photoionization measurements is indicated by the dot. Both calibration methods agree very well.

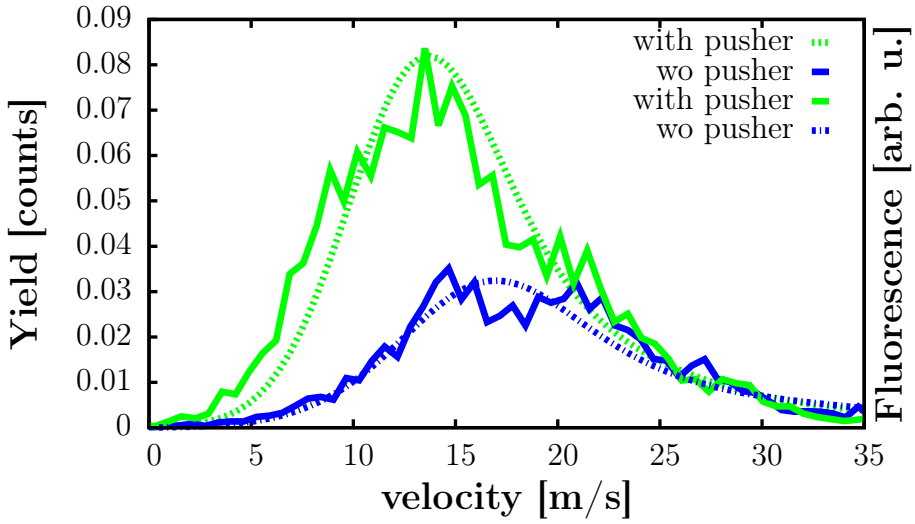

Figure 5.21: Corrected velocity distribution of the atom beam. The solid lines correspond to measurements where the momentum of the ions originating from the atom beam has measured in photoionization measurements, the dashed lines to the fluorescence measurements convoluted with the resolution of the spectrometer and corrected for the angle of the atom beam with respect to the y-axis of the spectrometer. Using a pushing beam leads to higher fluxes and smaller velocity distributions in the atom beam.

error bars for the photoionization measurement were obtained from comparison of three separate measurements. Both calibration methods thus agree well and we can deduce that the spectrometer is linear over a range of 5 mm.

Figure 5.21 shows the velocity distributions obtained from fluorescence measurements (solid lines), convoluted with the resolution of the spectrometer and corrected for the angle of the atom beam with respect to the y-axis of the spectrometer together with the velocity distribution obtained from the photoionization measurements and calibrated as described above. The green line corresponds to the velocity distribution of the atom beam generated from a 2D MOT with a pushing beam, whereas the blue line corresponds to the atom beam generated without an additional pushing beam in the 2D MOT. The corresponding dashed lines are the velocity distributions measured by fluorescence using the time of flight method.

Next to being an independent measurement on the calibration of the detector the measurement also allows an independent measurement on the velocity distribution of the atom beam. This distribution has so far has only been measured using time-resolved fluorescence measurements, where the lack of very slow atoms might have been caused by a systematic error in the measurement. This might be due to pushing the slow atoms out of the detection region due to radiation pressure from the probe beam. The ionization measurement is a great tool to verify that no atoms close to zero velocity are present in the atom beam.

5.5.1 Outlook: atom beam generated in a 2D MOT as a new target?

The possibility to use the atom beam generated by the 2D MOT as a target itself is discussed in this section. So far, RIMS has been used in conjunction with either a supersonic gas jet or magneto-optically trapped atoms. For the first time in this thesis, we have the possibility to use an atom beam generated by a 2D MOT as a target.

Supersonic gas jets are achieved by forcing a gas (which can be a noble gas or any type of molecular gas) at high pressure (1-20 atm) through a small nozzle (10-100 μm) into vacuum, thereby accelerating the gas to supersonic speed at the expense of internal motion, leading to effective cooling. According to [3] the longitudinal temperature spread in these beams is on the order of 0.1 a.u. for helium, scaling with the mass of the gas atom $\Delta P_{jet} \propto \sqrt{m}$, such that a momentum spread of $\Delta P <$ 0.5 a.u. is hard to achieve for heavier elements than argon. The transverse spread is, depending on the element and experimental setup, on the order of 0.07 a.u. Typical particle densities on the order of $10^{11} - 10^{12}\,\mathrm{cm}^{-3}$ are achieved around 10 cm away from the nozzle in gas jets.

In our case we have an atom beam with rubidium, which is far heavier than any element that can be cooled sufficiently in a supersonic gas jet. In the atom beam a momentum spread of 0.25 a.u. in the longitudinal direction and only 0.017 a.u. in the transverse beam direction is achieved. At a distance of 40 cm from the exit hole we measure a density of $1 \times 10^7\,\mathrm{cm}^{-3}$. Reducing the distance between the exit hole and the interaction volume also to 10 cm, which is not a conceptual problem, would lead to densities on the order of $10^9\,\mathrm{cm}^{-3}$, two orders of magnitude smaller than in supersonic gas targets.

Using a 2 dimensional magneto-optical trap to generate a cold atom beam thus allows to extend the possible species used as a target for ion-atom or photon-atom collisions without including the more elaborate setup needed for three-dimensional magneto-optical trapping. Compared to atom beams generated by supersonic gas jets, heavier atomic species are made available at the expense of the targets' densities, while gaining in transversal target temperature. From the experimental side, the vacuum setup for a 2D MOT only requires one ion-getter pump, while supersonic gas jets require several pumping stages due to the large gas load.

5.6 Conclusion

In this section photoionization measurements have been used to characterize the setup. In a first experiment, we have shown that we can characterize density profiles of the targets using photoionization and counting the ions, which is an alternative method as compared to absorption imaging. Furthermore, using the technique of photoionization the spatial information and density profile of the atom beam were measured. Of particular interest for further 2D MOT setup is the position of the atom beam with respect to the 3D MOT. In our case the optimized loading rate is obtained when the atom beam is positioned 4.5 mm aside of the 3D MOT. The velocity distribution of the atom beam can also be characterized in photoionization measurements when including time of flight information of the recoil ions. The results are compared to the results obtained using state of the art techniques, based on time-dependent fluorescence measurements. All results obtained using independent measuring techniques agree very well.

Using the spectrometer as a recoil ion momentum spectrometer, photoionization experiments can be used to characterize the spectrometer. The characterization is done by measuring the momentum of the recoil ion after photoionization as well as, in order to extend the area of the spectrometer, by using the velocity distribution of the atom beam. We obtain the same calibration factor from both methods and the spectrometer behaves linearly over the measured range. With the current configura-

tion of the spectrometer, we find an upper limit on the resolution along the time of flight axis of 0.2 a.u. and 0.37 a.u. in spatial direction. From simulations we expect a resolution of 0.05 a.u. in both directions. Due to the very low recoil momentum of 0.18 a.u. from the photoionization process, the extraction field is only 0.28 V/cm and might limit the resolution due to electrical stray fields from the surrounding chamber. In future experiments on ion-atom collisions the detected momenta and thus the needed extraction fields are much larger, such that stray fields are not expected to limit the resolution.

Chapter 6

Conclusion and outlook

In collaboration with the group of R. Hoekstra at the KVI in Groningen, the Netherlands, we measured the energy dependence on double-charge transfer of charged oxygen O^{6+} colliding with ground state sodium atoms (Na(3s)). The experimental setup allowed to identify electron capture into different states with principle quantum number nn', revealing two different capture channels: One channel led to the formation of asymmetric final states $3ln'l'$ with $n' \geq 4$. A second channel led to the formation of the symmetric final states $3s^2$ and $3l3l'$. By changing the projectiles velocity and thus the collision energy, the effective interaction time of the collision could be tuned and the dynamics during the charge transfer could be investigated. In the range of $v_P = 0.58$ a.u. down to $v_P = 0.39$ a.u. a dramatic effect on the relative population of the symmetric versus the asymmetric states could be observed: at high velocities only about 20 % of the collisions led to the population of the symmetric states, whereas at low velocities 80 % of the collisions populated the symmetric channels. This was a remarkable result since the electrons start from an asymmetric configuration in the target atom. The measured transverse momentum components suggest different transfer mechanisms for the two channels: asymmetric states are populated in a two-step process while symmetric states are populated in a one step process, involving a correlation between the electrons and is thus called correlated double capture (CDC). The results on the energy dependence in ion-alkali collisions were similar to the ones in helium-ion collisions, where, starting from an equivalent electron configuration, the production of nonequivalent electron configurations became dominant at low collision energies due to electron-electron interactions [72].

In this thesis a transportable apparatus for investigation of multiple charge transfer in ion-atom collisions at the HITRAP facility at the GSI *Helmholtzzentrum für Schwerionenforschung* has been designed, assembled and characterized. A first generation experiment, consisting of a magneto-optical trap loaded from background gas equipped with an ion detector, has been upgraded. The upgraded and novel apparatus combines two state of the art techniques in modern atomic physics: recoil ion momentum spectroscopy (RIMS) with trapping of neutral atoms in magneto-optical

traps with high density (dark spontaneous optical trap) and high loading flux. With this apparatus a high-density target with no background ions and high loading flux is made available for kinematically complete experiments involving fragmentation of the target atoms through either photons, ions or electrons.

Atoms are loaded from a cold atom beam generated in a two-dimensional magneto-optical trap (2D MOT) in a separate chamber and are subsequently pushed towards the three-dimensional magneto-optical trap (3D MOT) through a small hole of 800 μm, which also serves as a differential pumping tube. No background ions are thus present in the science chamber. From the 2D MOT we obtain a flux of 3.5 $\times$ 10^9 atoms/s with a mean center of mass velocity in longitudinal direction of 14 m/s and a velocity spread of 3.5 m/s, corresponding to a momentum spread of 0.35 a.u.. In transverse direction the temperature is 200 μK. The atom beam can serve as a target itself, with reduced density as compared to conventional gas jets used in COLTRIMS.

The high density target can be either operated as a bright MOT or, if denser targets are needed, in a dark SPOT configuration. The 3D MOT can be loaded from the 2D MOT with 2.9×10^8 atoms at a loading rate of 3×10^9atoms/s, or, during operation of the target in dark SPOT configuration, with 7.4×10^8 atoms at a reduced loading rate of 1×10^9 atoms/s. This leads to typical densities of 2×10^{10} atoms/cm^{-3} and a temperature of 200 μK in the bright MOT and 2×10^{11} atoms/cm^{-3} at a temperature of 170 μK in the high density target. The corresponding density in the atom beam at the interaction region has been determined to be 1×10^7 atoms/cm^{-3}. The characteristics of the three different targets available in this setup are summarized in table 6.1.

In first experiments, the new recoil ion momentum spectrometer has been characterized using non-resonant two-photon ionization of rubidium ground state atoms. The very small recoil momentum of 0.18 a.u. provided a stringent test of the spectrometer, since it had been designed for detection of much larger recoil momenta of several a.u. as expected in ion-atom collisions. From these measurements an upper limit on the resolution of 0.18 a.u. in time of flight and 0.3 a.u. in y-direction of the spectrometer could be determined. Due to the very low extraction fields of 0.28 V/cm stray fields might have limited the resolution. Furthermore, from the simulations, a better resolution is expected for changing the position of the focusing plate. Experimental tests are currently under investigation.

The Heidelberg MOTRIMS setup is ready for implementation at the HITRAP beamline at GSI. Prior to its implementation further improvements of the target are planned. Magnetic field compensation all along the spectrometer will be provided by including a large cage with magnetic compensation coils around the experiment, compensating for the magnetic stray fields at the beamline of the HITRAP facility.

	cold atom beam	3D MOT	dark SPOT
density [atoms/cm^{-3}]	1×10^{7} [a)]	2.90×10^{10}	2×10^{11}
size (FWHM) [mm]	11.2[a)]	8.6	9.3
flux/loading rate [atoms/s]	3.5×10^{9}	3.0×10^{9}	1×10^{9}
temperature [μK]	38×10^{3} [b)]	200	170
mean velocity [m/s]	10-15	0	0
longitudinal velocity spread [m/s]	3.5	0.25	0.22
transversal velocity spread [m/s]	0.2	0.25	0.22
momentum spread [a.u.]	0.25[c)]	0.017	0.016

Table 6.1: Characteristics of the different targets in this work. The mean velocity corresponds to the center of mass velocity.
[a)] At the interaction volume, 40 cm away from the exit hole.
[b)] Longitudinal temperature.
[c)] Given in longitudinal direction.

Furthermore, the ultracold atoms will be loaded into a crossed optical dipole trap [115] following the setup in the Rydberg experiment in our group with the possibility to cool to quantum degeneracy [116, 117]. A completely new target would thus be made available. In crossed dipole traps trapping volumes down to 15 μm can be achieved. The reduced trapping volume will increase the resolution of the recoil ion momentum spectrometer (the current size of the MOT is 8-9 mm (FWHM)). Another advantage is the strong increase in density, allowing for densities on the order of 10^{13} cm^{-3}, leading to a better signal to noise ratio for the investigation of multiple charge transfer. Finally, expansion of the atomic cloud due to switching times of the magnetic trapping field will be avoided.

Before the ion collision experiments at the HITRAP beamline ion optics will be implemented in the setup such that the ion beam can be focused down onto the target. Furthermore a detector for the projectiles will be implemented, allowing for coincidence detection of the projectiles with recoil ions. True double capture can thus be differentiated from transfer excitation processes. In addition, with our knowledge of the number of trapped atoms, full differential cross sections can be determined.

A schematic of the Heidelberg MOTRIMS setup at GSI is depicted in figure 6.1. The first system which will be investigated in collaboration with the GSI in Darmstadt will be charge transfer in collision between argon Ar^{16+} and ground-state rubidium atoms (Rb(5s)). The argon ions will be provided by an EBIT (SPARC-

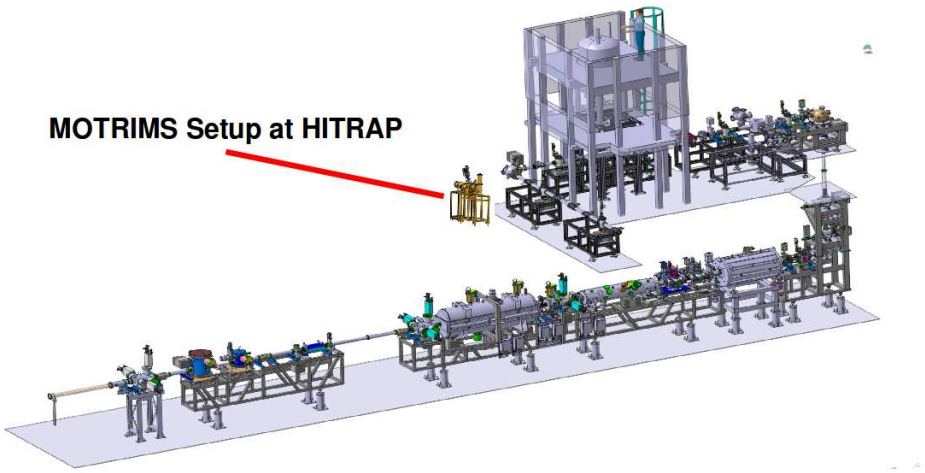

Figure 6.1: MOTRIMS setup at the HITRAP beamline. With courtesy of W. Quint.

EBIT) [118], which is attached to the HITRAP beamline. Using the classical over the barrier model (CBM), estimates concerning the energy transfer, the recoil ion's transverse momentum and the cross sections can be made and are summarized in table 6.2.

Due to the large difference in binding energy of the two outer electrons in rubidium the capture radius for single charge transfer as compared to two or more electron transfer is much larger. The Q-value increases with increasing number of captured electrons up to -108 eV for capture of five electrons. Compared to the O^{6+} + Na(3s) system the expected charge transfer in Ar^{16+} + Rb(5s) happens at larger internuclear distances.

The probability of capture up to four electrons and the corresponding Q-value

Electron #	1	2	3	4	5
nl	$5s$	$4p$	$4p$	$4p$	$4p$
$-E_i$ [eV]	4.18	27.29	39.02	52.20	68.44
Q_i^{OtB} [eV]	-6.96	-34.02	-60.4	-85.34	-108.4
R_i^{in} [a.u.]	58.62	13.2	11.75	10.42	9.1

Table 6.2: Binding energies before and after the transfer, Q-values and the capture radii for the first five electrons in collisions of Ar^{16+} with Rb($5s$) calculated using the OtB model at a projectile energy of $v_P = 9$ keV/amu. The binding energies are taken from [106].

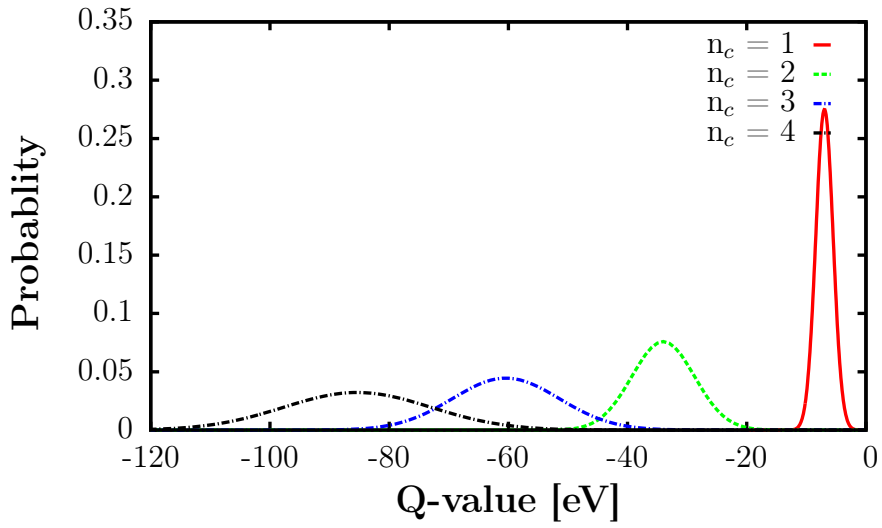

Figure 6.2: CBM estimates for the probability and Q-value distribution of n_C = 1,..,4 electron transfer for Ar^{16+} + Rb(5s) at a projectile velocity of v_P = 0.6 a.u..

spectrum is shown in figure 6.2. With increasing number of electrons transferred the probability decreases, whereas the total Q-value increases and the Q-value distribution widens. The corresponding momenta transferred to the recoil ion during the collisions for transfer of up to four electrons is depicted in figure 6.3.

The classical over the barrier model can also be used to estimate the cross sections for the different channels using equation A.8. Based on the only experimental results on double charge transfer we set f_r = 0.5 [52]. The expected cross sections for multiple charge transfer are two orders of magnitude smaller than for single charge transfer. From the densities of the targets together with the ion flux of J = 0.9 10^6 s^{-1} [119] the expected transfer rate can be estimated. The results are summarized in table 6.3. Compared to the O^{6+} + Na(3s) system the cross section in Ar^{16+} +

	Rb^+	Rb^{2+}	Rb^{3+}	Rb^{4+}	Rb^{5+}
σ [10^{-15}cm^2]	138	1.6	1.3	1.1	0.5
R_{MOT} [Hz]	45	0.5	0.4	0.35	0.15
R_{dark} [Hz]	100	1.2	0.9	0.8	0.35

Table 6.3: Total cross sections and rates for the transfer of one to five electrons in collisions of Ar^{16+} on Rb(5s) calculated using the CBM model.

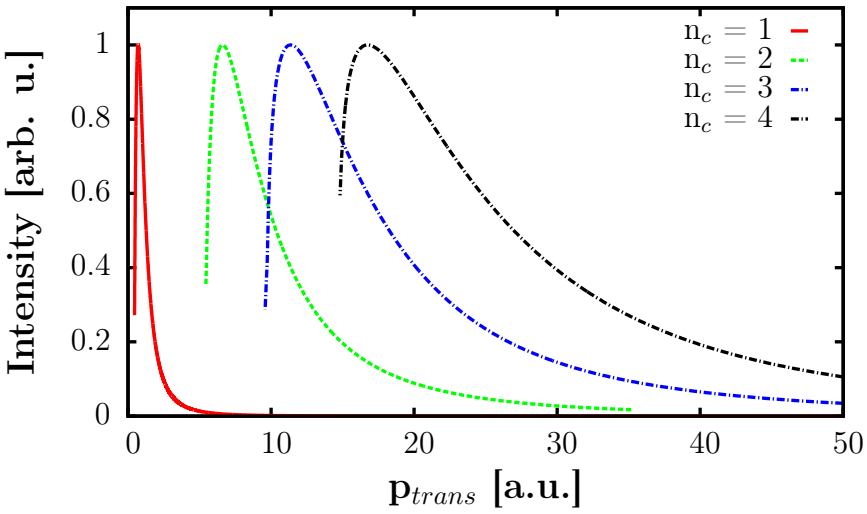

Figure 6.3: CBM calculations estimating transverse momentum distributions in Ar^{16+} + Rb(5s) for up to four electrons (n_C). The more electrons are transferred the higher the expected transverse momentum of the recoil ion.

Rb(5s) are two orders of magnitude larger, reflecting the higher charge state of the projectile and the smaller binding energies of rubidium.

Appendix A

Electron capture within the classical over the barrier model

A short summary of the classical over the barrier model is given. A collision is fully described by the impact parameter b and the energy transferred among the collision partners. The smaller the impact parameter, the larger the scattering angle of the projectile, leading to larger transverse momentum of the target. The transferred energy is expressed by the Q-value, also called the inelasticity of the collision. A large Q-value translates in a large longitudinal momentum of the recoil ion. During the collision of a highly charged ion with a neutral atom, either impact ionization or charge transfer occurs. We want to focus on the process of charge transfer, in particular double charge transfer. This process mainly occurs for projectile velocities smaller than the orbital velocity of the target electrons, such that the interaction time between the ion and the atom is long. During the collision the electron can be shared between the projectile and the atom, forming a so-called quasimolecule. Therefore the interaction cannot be treated quantum mechanically in a perturbative picture. In case of more than one electron transfer, the correlation between the electronic wavepackets also needs to be included. Therefore, a classical model, the so-called classical over the barrier model, will be described in this chapter.

The classical over the barrier model (CBM) is a static model describing multiple charged ion-atom collisions in the low velocity regime. In the eighties, it has been developed to describe multiple electron capture. Up to date, for multiple charge transfer it is still a challenge for theory to describe the collision quantum mechanically.

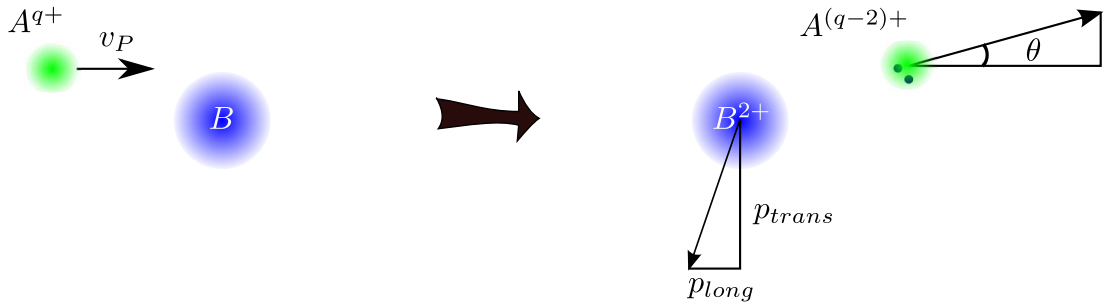

Figure A.1: Double charge transfer in ion-atom collision. The incoming projectile with velocity v_P interacts with the atoms, forming a quasi-molecule. After the interaction, the projectile has a certain probability to capture one or more electrons, scattering with a scattering angle θ, giving the recoil ion some recoil momentum.

A.1 Charge transfer in the classical over the barrier model

In this section we will follow closely the derivation of Niehaus [16]. The CBM is used to derive an expression for the Q-value and the transverse momentum. The underlying mechanism described in this model the transfer of r electrons in a collision between a q-fold projectile and a neutral target:

$$\mathrm{A}^{q+} + \mathrm{B} \rightarrow \mathrm{A}^{(q-r)+} + \mathrm{B}^{(r+)}. \tag{A.1}$$

For the case of two-electron capture the process is sketched in figure A.1.

A.1.1 Q-value in the CBM

In the collision two parts of the trajectory are distinguished: the 'way in' and the 'way out'. The CBM is based on a 'molecular' picture: during the collision the target's and ion's Coulomb field form a molecular state for the electron. Electron transfer can take place at internuclear distances at which the height of the Coulomb barrier is lower than the binding energy of the electrons which is called the capture radius. During interaction, the binding energies of the target electrons experience a Stark shift due to the Coulomb field of the projectile, increasing the binding energy of the $i's$ electron $\mathrm{E}_{b,i}$ to the energy

$$E_i = E_{b,i} - q/R, \tag{A.2}$$

where R is the internuclear distance.

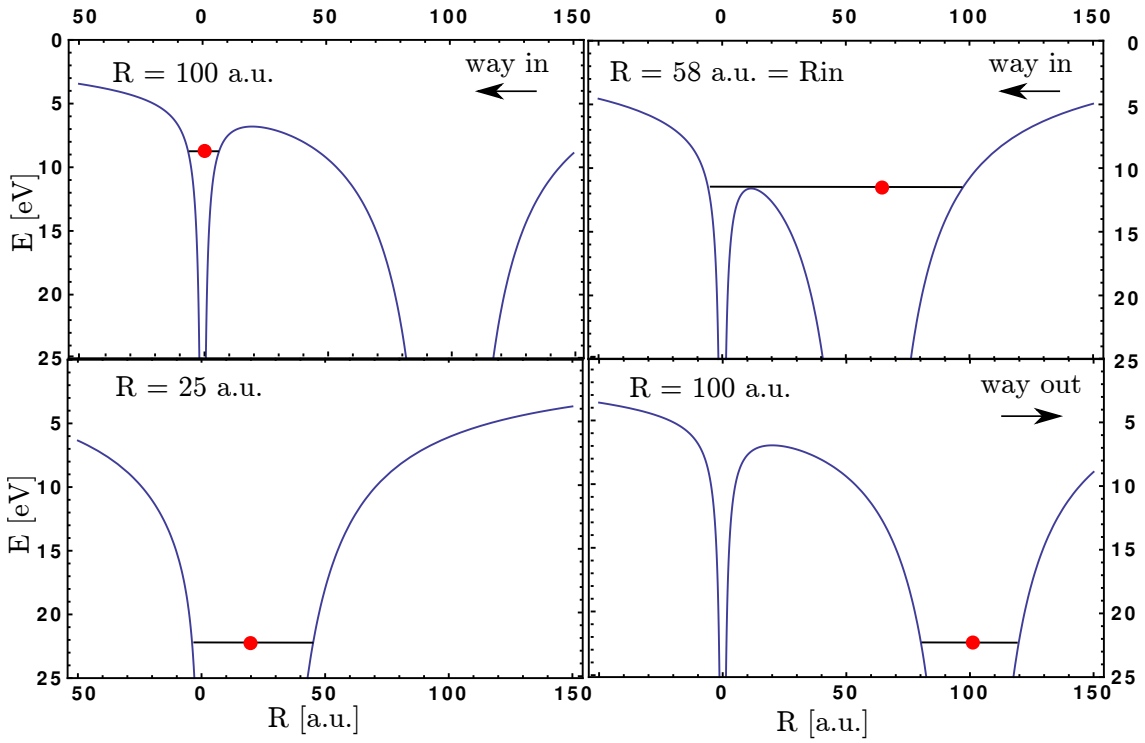

Figure A.2: Single charge transfer in the picture of the CBM for the system Rb(5s)+Ar^{16+}. During way in the electron is bound to the target. At a internuclear distance of R = R_{in}, the electron moves in a quasi-molecule. At the way out, the electron is caught to the projectile with a certain probability.

The $i's$ electron is thus experiencing the potential of the approaching projectile, added to its own potential

$$V_i^{in}(r) = -\frac{q}{|\mathbf{R}-\mathbf{r}|} - \frac{i}{|\mathbf{r}|}, \tag{A.3}$$

for $0 < \mathbf{r} < \mathbf{R}$, and $\mathbf{r}$ is the coordinate of the i'th electron with respect to the parent nucleus (see figure A.2). Thus the height of the Coulomb barrier is a function of the internuclear distance and the capture radius R_i^{in}, i.e. the distance where the i'th electron can be transfered, is given by

$$R_i^{in} = \frac{i + 2\sqrt{iq}}{-E_i}. \tag{A.4}$$

At this distance the electron moves in the joint potential of the projectile and the target, so to say in a quasi-molecule.

The point at which the internuclear distance increases again is called the turning point and is defined by the impact parameter. After this, the internuclear distance increases again and the electrons are bound in this quasi-molecule until the potential barrier is again at the same energy height as the electrons binding energy. At this point, there is a certain probability that the electron is transferred or that it stays with the target. Due to the discrete nature of the binding energies, this process of capture or recapture is sequential. In this case the screening of the ion's charge q depends on the number of electrons already captured on the way out and need to be taken into account, such that the internuclear distance at which (re)capture of the electron takes place, is given by

$$R_i^{out} = R_i^{in}\left(\frac{\sqrt{q-c_i} + \sqrt{i+c_i}}{\sqrt{q}+\sqrt{i}}\right)^2, \tag{A.5}$$

where c_i is the number of already captured electrons during the transfer of the i'th electron. The binding energy at infinite nuclear distance of the i'th electron being captured by the projectile is given by

$$E_{b,i}^{final} = E_b^i - \frac{q}{R_j^{in}} + \frac{i+c_i}{R_j^{out}}. \tag{A.6}$$

The inelasticity of the process, i.e. the difference in biding energy, in the CBM

approximation is thus given by

$$Q^{OtB} = \sum_{i=1}^{r} \left(E_i^{final} - E_i \right) = \sum_{i=1}^{r} \left(-\frac{q}{R_i^{in}} + \frac{i + c_i}{R_i^{out}} \right). \tag{A.7}$$

The cross section for transfer of r electrons is proportional to the geometrical cross sections R_r^{in} and R_{r+1}^{in}:

$$\sigma_r = f_r \pi [(R_r^{in})^2 - (R_{r+1}^{in})^2], \tag{A.8}$$

where f_r is the product of the probabilities for single electron transfer f_i.

The model so far assumes that the electrons are transferred into one final state in the projectile. Due to the quantized nature of electronic states, this assumption is, however, in general not fulfilled. A time-dependence has been added to the static model by Niehaus [16] by including the Heisenberg uncertainty relation $\Delta E \Delta t \simeq 1$, leading to a population of energy levels distributed around $E_{b,i}^{final}$. Following the uncertainty relation, the transfer is now made in a limited time interval, leading to a uncertainty in the energy definition. The change in Coulomb potential height is now given by

$$\Delta V = \frac{dV}{dt} \Delta t = \frac{dV}{dR} v_{rad} \Delta t, \tag{A.9}$$

with v_{rad} being the radial velocity. With the assumption that the classical uncertainty is equal to the minimum quantum-mechanical uncertainty, it follows

$$\Delta V = \sqrt{\left| \frac{dV}{dR} \right| v_{rad}}. \tag{A.10}$$

The final energy width ΔQ is the quadratic sum of the uncertainties of all transferred electrons during the collision. Assuming a Gaussian distribution of Q around the predicted Q^{CMB} with width ΔQ leads to a reaction window of width

$$W(Q) = \frac{1}{\Delta Q \sqrt{\pi}} \exp \left[- \left(\frac{Q - Q^{OtB}}{\Delta Q} \right)^2 \right], \tag{A.11}$$

where $\Delta Q \propto \sqrt{v_p}$, leading to an increasing width of the reaction window for increasing collision energies.

A.1.2 Scattering angle in the CBM

Using CBM also estimates for scattering angles and transverse momenta can be obtained by calculating the Coulomb repulsion along the projectile trajectory. The

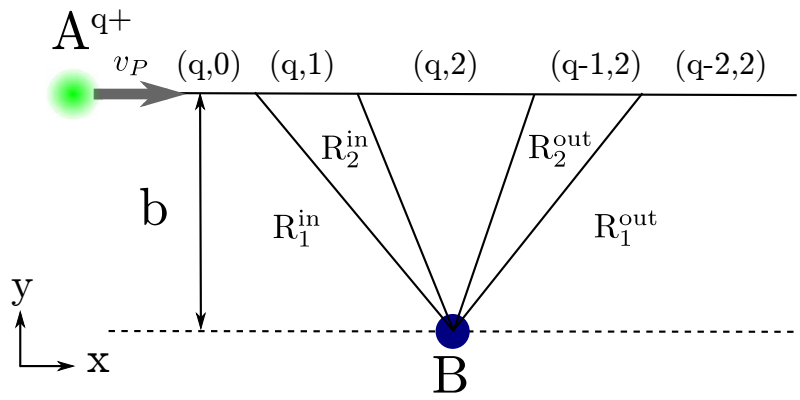

Figure A.3: Scheme of the charge distribution of (projectile, target) along the projectile's trajectory in the case of the transfer of two electrons from the target B to the q-fold charged projectile A^{q+}. $R_i^{in/out}$ indicate the capture radii for the way-in and way-out, respectively.

derivation of it has been done in [37, 17] and the results of these works are summarized in the following. Starting from the Coulomb force between two point charges $q1$ and $q2$ at distance R, the Coulomb force can be written as:

$$\mathbf{F} = \frac{q_1 q_2}{R^2}\mathbf{e}_R \tag{A.12}$$

where $\mathbf{e}_R$ is the radial unit vector. The trajectory of the projectile propagating along the x axis is characterized by its velocity v_P and the impact parameter b (see Fig. A.3). Considering the target at the origin, the force perpendicular to the projectile's trajectory is than given by:

$$F_y = \frac{q_1 q_2 b}{(x^2 + b^2)^{3/2}}. \tag{A.13}$$

Integration over time and assuming a stationary target than gives the transverse momentum

$$p_{trans} = \int_{-\infty}^{\infty} F_y dt = \frac{1}{v_p}\int_{-\infty}^{\infty} F_y dx. \tag{A.14}$$

This integration over time can also be written as an integration along the projectile's trajectory, giving the following expression for the recoil's transverse momentum

after transfer of r electrons, as a function of the impact parameter b:

$$p_{trans}(b) = \frac{1}{v_p b}\left[\sum_{i=1}^{r}\left(q\sqrt{1-\left(\frac{b}{R_i^{in}}\right)^2}+r\sqrt{1-\left(\frac{b}{R_i^{out}}\right)^2}\right)+(q-r)r\right] \quad \text{(A.15)}$$

From $p_{trans} = m_p v_p \theta$ the projectiles scattering dependent cross section can than be obtained. Using this classical model we make approximations for the inelasticity and the transverse momentum distribution of the recoil ions emerging from charge transfer in ion-atom collisions.

Appendix B

Data correction

The data taken at the KVI in Groning cut some data in the time of flight direction due to a finite time window of the TDC of 2.2 μs. This direction is proportional to the transverse momentum distribution and the time window corresponds to a total momentum of 20 a.u. that can be recorded in the current configuration of the spectrometer. Therefore channels which are populated through a mechanism leading to a big transverse momentum are underestimated in the recorded data which needs to be corrected for. The procedure of this correction is discribed in detail in the following.
Due to the total loss of information on the data along the time of flight axis, we need to assume for the following procedure that the spectrometer is cylinrical symmetric in transverse direction. First, the transverse momentum components (time of flight and y-axis) are separated into the two main channels that we have identified, population into the symmetric and assymmetric states, by seperating the data in the x1 direction (proportional to the Q-value). We therefore cut the data in the Q value and only consider the data for the population of the symmetric state, corresponding to the data range from Q = -60 eV to Q = -31.1 eV Q value spectrum (see fig. B.1).
This data is projected onto the y-axis, corresponding to the $p_{trans,y}$ component (see figure B.2 a)). To this data a Gaussian is fitted[1]. Integration over the fittet Gaus gives the total number of counts (assuming that in y-direction no data is cut due to the finite size of the detector). Assuming that the data is cylindrical symmetric, the fittet parameters are used to fit the data obtained by projection onto the time of flight axis shown in figure B.3 a). From the time of flight data the ptrans intervall where data is recorded is determined, all ions arriving outside this time window were lost. In order to estimate how many ions were lost and the Gaussian function is integrated in this intervall (see fig. B.3). This value is compared to the

[1]The proper distribution corresponds to a projection of the three dimensional momentum distribution folded with the resolution of the detector. Since the physical process underlying the charge transfer and thus the distribution of the transverse momentum is not known, a Gaussian fit to the momentum distribution is made. This leads to a large systematic error of .

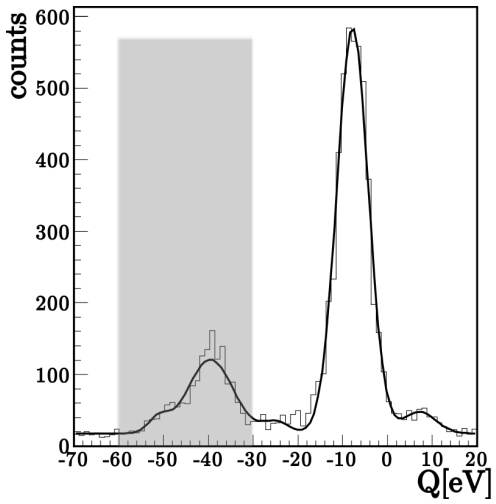

Figure B.1: Data taken for the correction are indicated by the shaded area and correspond to channel populating the final symmetric state.

Gaussian integrated to infinity which than gives the percentage of counts that were not recorded in the experiment due to the finite size of the time window of the TDC. Special care has to be taken of the background, in particular at low projectile energies, where the charge transfer rate is small, and the background is of comparable size of the data. From datasets only measuring background, we estimate that the background in the area of interest is linear when projected on the y-axis. In the actual data an area neighbouring the actual area of interest (50 bins on the x axis), having the same width as the cut for the symmetric states, is taken and the background is determined by fitting a linear slope to this area (see figure B.2 b)). The obtained fit parameters are used to subtract the background from the y-projection prior to fitting the gaussian distribution to the wing of the projected distribution.

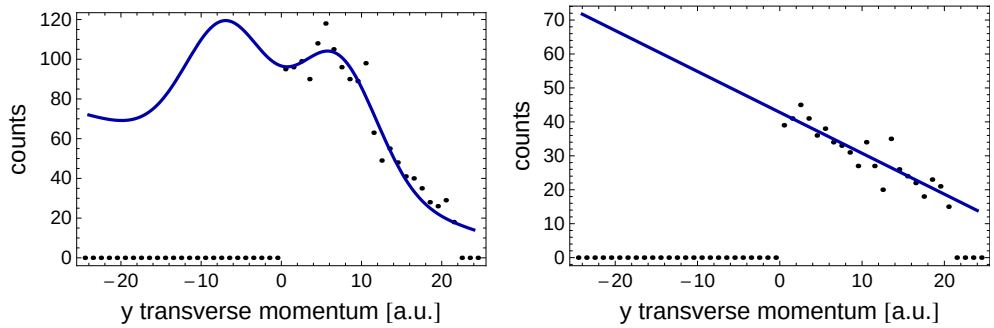

(a) (b)

Figure B.2: Data taken for the data correction. a) shows the projection of the y component of the transverse momenutm and the gaussian fit. b) shows the data and linear fit taken for background subtraction.

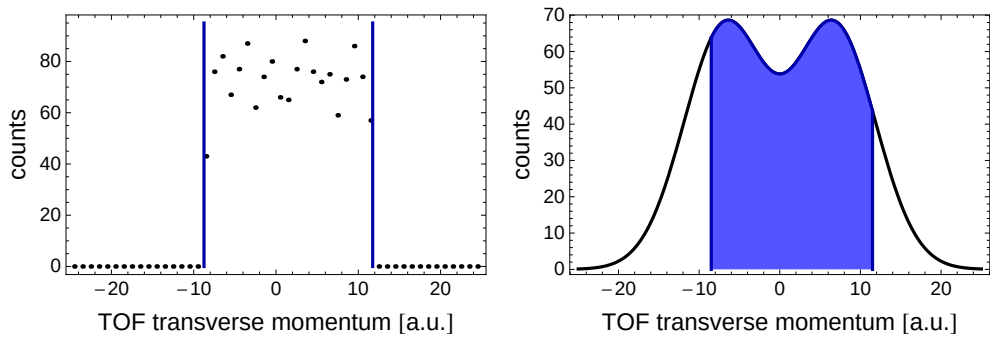

(a) (b)

Figure B.3: Data taken for the correction in the time of flight axis. a) shows the data cut in time of flight at ± 10 a.u. due to the finite time window. The shaded area in b) indicates the momentum recorded in the time window. The gaussian is used to estimate the data which is lost (for further explanation see text).

Appendix C

Photoionization with a high-power LED

Prior to rebuilding the experiment as described in this thesis, photoionization measurements using a high-power LED have been performed to show the potential of using high-LEDs for calibration of detectors as an alternative to high-power lasers.

C.1 Introduction

The increasing availability of high power LEDs for many different wavelengths allows for a large number of applications in atomic and molecular physics. One application of LEDs in combination with ultracold atoms is the fast and efficient loading of magneto-optical traps by means of light-induced atom desorption (LIAD) from surfaces using ultraviolet light [120]. Cetina *et al.* have used an LED at 370 nm to photoionize a large number of Yt atoms from a magneto-optical trap in order to transfer the cold ions efficiently into surface electron traps [121]. In this article we report on the use of a high-power LED in a pulsed mode of operation. Short light pulses are used to photoionize atoms trapped in a magneto-optical trap, leading to short ion pulses of very well-defined momentum. These short ion pulses can be used to calibrate time-of-flight assemblies with high accuracy. Polarizing the light emitted from the LED could be used for the calibration of position sensitive ion detectors, since the electrons are preferably emitted along the polarization axis, giving a momentum to the recoil ion in the opposite direction. Compared to high-power pulsed lasers otherwise required for this purpose, the LED technique is a very cheap and simple solution, still allowing for high-precision measurements.

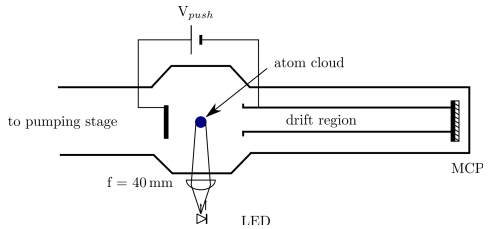

Figure C.1: Experimental setup for the ion detection.

C.2 Setup

The vacuum setup used for the demonstration of the pulsed LED ion source is designed to detect recoil ions from collisions in a magneto-optical trap on a micro-channel plate (MCP) followed by a position sensitive detector. The trap is therefore placed inside a recoil-ion momentum spectrometer (Fig. C.1). In the experiment ^{85}Rb atoms are confined in a magneto-optical trap serving as a target for the light pulses. The atoms are loaded from a background gas and are trapped in a retro-reflected magneto-optical trap. The trapping beams have a diameter of 21.2 mm and a total power of 68.1 mW.

The light pulses are produced by a blue high-power LED from CREE[1] with model number XREBLU-B5, where B5 indicates the chromaticity group of the diode, in our case the wavelength range from 475 nm to 480 nm. The spectrum of the emitted light, measured with a fiber spectrometer (Ocean Optics, model USB2000) is shown in Fig. C.2. The LED can be operated either in cw mode using a regulated current source, or in pulsed mode with short current pulses produced by the driver circuit depicted in Fig. C.3. At the input of the pulse driver a low TTL pulse must be applied. The inverting MOSFET driver SN75372 provides the gate voltage for the switching power MOSFET IRFU3910. The additional Schottky diode D1 is needed for damping voltage overshoots and ringing. The capacitor C1 provides the energy for the light pulse. The resistor R1 is used to limit the current and to allow for a measurement of the current with a differential probe. In this configuration, about 2 A of current flow through the LED during the pulse. As the specified maximum continuous operating current for this LED is 700 mA, the pulse width and duty cycle must be chosen carefully in order not to destroy the LED. The light emitted by the diode is extremely divergent ($\theta = 120\ °$) and is therefore focused onto the atom cloud using an aspheric lens with a diameter of 50 mm and a focal length of 40 mm. Atoms which are in the $5P_{3/2}$ state can either be ionized by the LED or excited to Rydberg states. The ions are first accelerated towards the ion detector by an electric

[1] http://www.cree.com

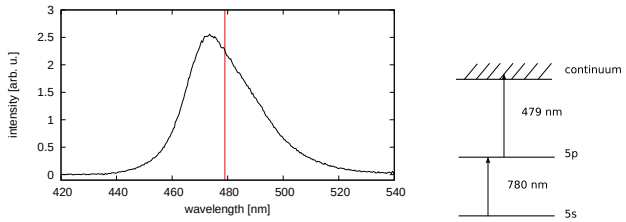

Figure C.2: left: spectrum of the LED, the red line indicates the ionization threshold of Rb. right: level scheme of ^{85}Rb.

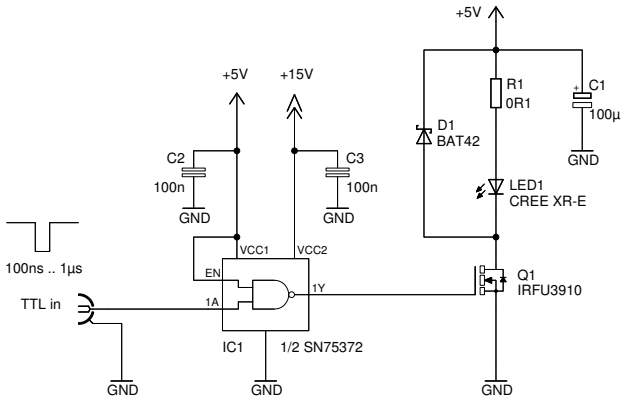

Figure C.3: Circuit diagram for the pulsed LED.

field of $3.3\,V/cm$ ($V_{push} = 50\,V$), followed by a field-free drift region, and are then detected by the micro-channel plate after a time of flight of about $72.3\,\mu$s. The ion detector is gated for $3\,\mu$s with a delay of 70.8 μs after the LED.

C.3 Results

C.3.1 Ionization rate

We monitor the fluorescence signal of the magneto-optical trap with and without the ionization light (Fig. C.4). The typical loading times without the LED are on the order of 50 s. Once the MOT reaches a steady-state (losses due to collisions with background ions and losses due to two-body losses between trapped excited state atoms compensate the loading rate), we switch on the ionization light. Since the ionization of the excited atoms due to the LED is of the same order of magnitude as all other loss sources from the trap we see a clear decrease in the MOT fluorescence. We verified that only the excited atoms are ionized by measuring the ion rate on the MCP, with and without the trapping lasers.

Following the reasoning in [114] we estimate that 25% of the trapped atoms are in the excited state. Neglecting ionization of the background gas, we can estimate the ionization rate for the spectrum of our LED from the rate equations for the MOT. With a fit of the rate equations (with and without LED) to the fluorescence in the steady-states we can deduce an ionization rate of $\Gamma_{ion} = 0.5\,$atoms/s, leading to an averaged photoionization cross section of $\sigma = 2.4 \cdot 10^{-18}\,\mathrm{cm}^{-3}$. Measurements of ionization of the background show that we also ionize atoms which are in the trapping volume, so that the dependence of the loading rate of the MOT as well as collisions with background ions should be accounted for in the rate equations. Second order differential equations could be fitted to the fluorescence curves taking into account the time dependence of the background atoms on the LED power. Loading the trap from e.g. a 2 dimensional magneto-optical trap, this rate could be determined from the fluorescence with our rate equations more accurately because no background gas would be present.

C.3.2 Pulsed measurements

Assuming a constant photoionization cross section over the spectral width of the ionizing light, the photoionization rate (per atom) can be expressed as

$$R_{at} = \frac{I\sigma_{PI}}{E_{ph}}\,, \tag{C.1}$$

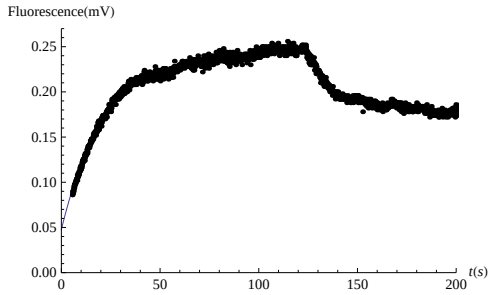

Figure C.4: Loading curve of the trap without LED, after t = 120 s the ionization light is switched on P_{cw}=120 mW, leading to a clear decrease in the fluorescence signal.

where I is the intensity of the light (power per area), σ_{PI} is the photoionization cross section for Rb 5p, and E_{ph} is the energy of the incoming photons. The total ion production rate from a magneto-optical trap of radius r and density ρ is then given by

$$R_{\mathrm{MOT}} = \frac{4}{3}\pi r^3 \, \rho R_{\mathrm{at}} f \ . \tag{C.2}$$

For a typical magneto-optical trap with radius $r = 400\,\mu$m and density $\rho = 10^9\,\mathrm{cm}^{-3}$, we expect a rate of about 177 Hz. The factor f includes the detector efficiency ($\approx 34\%$), the excited state fraction ($\approx 25\%$) and the fraction of the LED above the ionization threshold ($\approx 50\%$). Here we used the photoionization cross section $\sigma_{\mathrm{PI}} = 1.48 \times 10^{-17}\,\mathrm{cm}^{-2}$ for Rb 5p as measured in [122]. In pulsed operation with a repetition rate of 1 kHz and a pulse length of 1 μs we observe a rate of about 145 Hz, which is in good agreement with our estimation.

Reducing the pulse length to 100 ns while increasing the repetition rate to 10 kHz the ion rate decreases by about 20%. This is due to the finite rise and fall times of the LED pulse (see Fig. C.5), effectively decreasing the relative pulse area. If the total number of atoms is calibrated using absorption imaging, one could use the LED in pulsed mode operation to calibrate the ion detector efficiency.

C.4 Conclusion

We have demonstrated a low-cost source of ultracold ions using a high-power LED. High-power LEDs are nowadays available in many different wavelengths. The length of the pulses is mainly limited by the capacitance of the LED. Without optimization of the circuit for short pulses we have demonstrated a pulsed source of ions of 100 ns length in time. This source can be used for calibrating time-of-flight spectrometers, where otherwise pulsed lasers are required. Polarizing the light from the LED, one

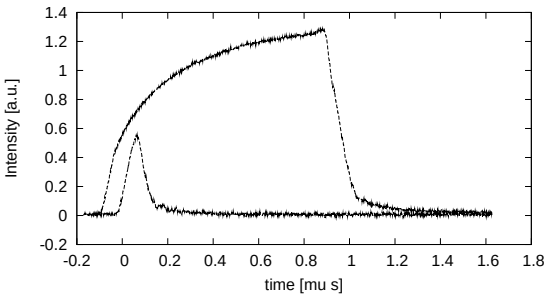

Figure C.5: Measurement of LED in pulsed mode. For short pulses the flank plays an important role, full power is only reached after 80 ns: Therefore, we detect less ions than expected.

could also use this light for calibration of position sensitive detectors as used for e.g. recoil-ion momentum spectrometers. Furthermore, we proposed the operation of the LED in pulsed mode for the precise determination of the efficiency of ion detectors.

Appendix D

Atomic units

The atomic units system is based on

$$\hbar = m_e = e = 4\pi\epsilon_0 = 1, \tag{D.1}$$

$\hbar$ being the Plancks constant devided by 2π, m_e and e are the electron mass and the electron charge and ϵ_0 is the permitting of free space.
In atomic physics it gives a system of neutral units, where all quantities are related to the ones of an hydrogen atom.

quantity	SI units	non-SI units
length	5.2918×10^{-11} m	0.529 Å
mass	9.1094×10^{-31} kg	511keV/c^2
charge	1.6022×10^{-16} C	
time	2.4189×10^{-17} s	
speed	2.1877×10^{6} m/s	
momentum	1.9929×10^{-24} kgm/s	
energy	4.3593×10^{-18} J	27.2114 eV
angular momentum	$1.0545887 \times 10^{-34}$ Js	

Table D.1: Overview of the most important physical quantities relating SI-values to atomic units.

Throughout this work temperatures of atoms are related to center-of-mass velocities and momentum spreads in different units. In table D.2 We want to give an overview of the most important temperatures and the related velocities in m/s and the momentum spreads in a.u..

temperature	momentum spread [a.u.]	velocities
300 K	21	296
200 μK	0.017	0.25
170 μK	0.016	0.22
493 mK	0.85	12
38 mK	0.25	3.5
23 mK	0.18	2.6

Table D.2: Most important temperatures and the corresponding center-of-mass velocities and momentum spreads.

List of Figures

Bibliography

[1] T. Rescigno, M. Baertschy, W. Isaacs, and C. McCurdy, "Collisional breakup in a quantum system of three charged particles," *Science*, vol. 286, no. 5449, p. 2474, 1999.

[2] R. Ali, V. Frohne, C. L. Cocke, M. Stockli, S. Cheng, and M. L. A. Raphaelian, "Q -value measurements in charge-transfer collisions of highly charged ions with atoms by recoil longitudinal momentum spectroscopy," *Phys. Rev. Lett.*, vol. 69, pp. 2491–2494, Oct 1992.

[3] J. Ullrich, R. Dörner, V. Mergel, O. Jagutzki, L. Spielberger, and H. Schmidt-Böcking, "Cold-target recoil-ion momentum spectroscopy: First results and future perspectives of a novel high-resolution technique for the investigation of collision induced many- particle reactions," *Comments At. Mol. Phys.*, vol. 30, p. 415, 1994.

[4] R. Dörner, V. Mergel, L. Spielberger, O. Jagutzki, M. Unverzagta, W. Schmitt, J. Ullrich, R. Moshammer, H. Khemliche, M. Prior, R. Olson, L. Zhaoyuan, W. Wu, C. Cocke, , and H. Schmidt-Böcking, "Cold Target Recoil Ion Momentum Spectroscopy," *Proc. The Physics of Electronic and Atomic Collisions*, p. 495, 1996.

[5] R. Dörner, V. Mergel, O. Jagutzki, L. Spielberger, J. Ullrich, R. Moshammer, and H. Schmidt-Böcking, "Cold target recoil ion momentum spectroscopy: a 'momentum microscope' to view atomic collision dynamics," *Phys. Report*, vol. 330, p. 95, 2000.

[6] J. Ullrich and V. Shevelko, *Many-particle quantum dynamics in atomic and molecular fragmentation*. Berlin: Springer, 2003.

[7] W. D. Phillips and H. Metcalf, "Laser deceleration of an atomic beam," *Phys. Rev. Lett.*, vol. 48, pp. 596–599, Mar 1982.

[8] W. Ertmer, R. Blatt, J. L. Hall, and M. Zhu, "Laser manipulation of atomic beam velocities: Demonstration of stopped atoms and velocity reversal," *Phys. Rev. Lett.*, vol. 54, pp. 996–999, Mar 1985.

[9] S. Chu, J. E. Bjorkholm, A. Ashkin, and A. Cable, "Experimental observation of optically trapped atoms," *Phys. Rev. Lett.*, vol. 57, pp. 314–317, Jul 1986.

[10] E. L. Raab, M. Prentiss, A. Cable, S. Chu, and D. E. Pritchard, "Trapping of neutral sodium atoms with radiation pressure," *Phys. Rev. Lett.*, vol. 59, p. 2631, 1987.

[11] B. D. DePaola, R. Morgenstern, and N. Andersen, "MOTRIMS: Magneto Optical Trap Recoil Ion Momentum Spectroscopy," *Advances in atomic, molecular and optical physics*, vol. 55, p. 139, 2008.

[12] R. Moshammer, J. Ullrich, M. Unverzagt, W. Schmidt, P. Jardin, R. E. Olson, R. Mann, R. Dörner, V. Mergel, U. Buck, and H. Schmidt-Böcking, "Low-energy electrons and their dynamical correlation with recoil ions for single ionization of helium by fast, heavy-ion impact," *Phys. Rev. Lett.*, vol. 73, pp. 3371–3374, Dec 1994.

[13] S. D. Kravis, M. Abdallah, C. L. Cocke, C. D. Lin, M. Stockli, B. Walch, Y. D. Wang, R. E. Olson, V. D. Rodriguez, W. Wu, M. Pieksma, and N. Watanabe, "Single ionization of he by low-velocity protons and c^{6+}: Ejected electron momentum distributions," *Phys. Rev. A*, vol. 54, pp. 1394–1403, Aug 1996.

[14] R. Moshammer, M. Unverzagt, W. Schmitt, J. Ullrich, and H. Schmidt-Böcking, "A 4 π recoil-ion electron momentum analyzer: a high-resolution "microscope" for the investigation of the dynamics of atomic, molecular and nuclear reactions," *Nuclear Instruments and Methods in Physics Research Section B: Beam Interactions with Materials and Atoms*, vol. 108, no. 4, pp. 425 – 445, 1996.

[15] J. Ullrich, R. Moshammer, A. Dorn, R. Dörner, L. Schmidt, and H. Schmidt-Böcking, "Recoil-ion and electron momentum spectroscopy: reaction-microscopes," *Reports on Progress in Physics*, vol. 66, p. 1463, 2003.

[16] A. Niehaus, "A classical model for multiple-electron capture in slow collisions of highly charged ions with atoms," *Journal of Physics B: Atomic and Molecular Physics*, vol. 19, p. 2925, 1986.

[17] I. Blank, "Double electron transfer in collisions of highly charged ions and ultracold atoms," Master's thesis, Universität Freiburg, 2008.

[18] W. Ketterle, K. B. Davis, M. A. Joffe, A. Martin, and D. E. Pritchard, "High densities of cold atoms in a dark spontaneous-force optical trap," *Phys. Rev. Lett.*, vol. 70, p. 2253, 1993.

[19] K. Dieckmann, R. Spreeuw, M. Weidemüller, and J. Walraven, "Two-dimensional magneto-optical trap as a source of slow atoms," *Physical Review A*, vol. 58, no. 5, pp. 3891–3895, 1998.

[20] J. Schoser, A. Batär, R. Löw, V. Schweikhard, A. Grabowski, Y. Ovchinnikov, and T. Pfau, "Intense source of cold Rb atoms from a pure two-dimensional magneto-optical trap," *Physical Review A*, vol. 66, no. 2, p. 23410, 2002.

[21] M. Barat and P. Roncin, "Multiple electron capture by highly charged ions at keV energies," *Journal of Physics B: Atomic, Molecular and Optical Physics*, vol. 25, p. 2205, 1992.

[22] R. Janev and H. Winter, "State-selective electron capture in atom-highly charged ion collisions," *Physics Reports*, vol. 117, no. 5–6, pp. 265 – 387, 1985.

[23] R. Hoekstra, F. Heer, and R. Morgenstern, "State-selective electron capture in collisions of He^{2+} with H," *Journal of Physics B: Atomic, Molecular and Optical Physics*, vol. 24, p. 4025, 1991.

[24] G. Lubinski, Z. Juhász, R. Morgenstern, and R. Hoekstra, "Low-energy state-selective charge transfer by multiply charged ions," *Physical Review Letters*, vol. 86, no. 4, pp. 616–619, 2001.

[25] N. Stolterfoht, C. C. Havener, R. A. Phaneuf, J. K. Swenson, S. M. Shafroth, and F. W. Meyer, "Evidence for correlated double-electron capture in low-energy collisions of O^{6+} with He," *Phys. Rev. Lett.*, vol. 57, p. 74, 1986.

[26] J. Ullrich and H. Schmidt-Bocking, "Time-of-flight spectrometer for the determination of microradian projectile scattering angles in atomic collisions," *Physics Letters A*, vol. 125, no. 4, pp. 193–196, 1987.

[27] J. Ullrich, R. Olson, R. Dorner, V. Dangendorf, S. Kelbch, H. Berg, and H. Schmidt-Bocking, "Influence of ionised electrons on heavy nuclei angular differential scattering cross sections," *Journal of Physics B: Atomic, Molecular and Optical Physics*, vol. 22, p. 627, 1989.

[28] V. Frohne, S. Cheng, R. Ali, M. Raphaelian, C. L. Cocke, and R. E. Olson, "Measurements of recoil ion longitudinal momentum transfer in multiply ionizing collisions of fast heavy ions with multielectron targets," *Phys. Rev. Lett.*, vol. 71, pp. 696–699, Aug 1993.

[29] V. Mergel, R. Dörner, J. Ullrich, O. Jagutzki, S. Lencinas, S. Nüttgens, L. Spielberger, M. Unverzagt, C. L. Cocke, R. E. Olson, M. Schulz, U. Buck, E. Zanger, W. Theisinger, M. Isser, S. Geis, and H. Schmidt-Böcking, "State-selective scattering angle dependent capture cross sections measured by cold target recoil ion momentum spectroscopy," *Phys. Rev. Lett.*, vol. 74, p. 2200, 1995.

[30] V. Mergel, R. Dörner, J. Ullrich, O. Jagutzki, S. Lencinas, S. Nüttgens, L. Spielberger, M. Unverzagt, C. Cocke, R. Olson, M. Schulz, U. Buck, and H. Schmidt-Böcking, "He^{2+} on He: State-selective, scattering-angle-dependent capture cross sections measured by cold target recoil ion momentum spectroscopy (COLTRIMS)," *Nuclear Instruments and Methods in Physics Research Section B: Beam Interactions with Materials and Atoms*, vol. 98, no. 1–4, pp. 593 – 596, 1995.

[31] R. Moshammer, B. Feuerstein, W. Schmitt, A. Dorn, C. D. Schröter, J. Ullrich, H. Rottke, C. Trump, M. Wittmann, G. Korn, K. Hoffmann, and W. Sandner, "Momentum distributions of ne^{n+} ions created by an intense ultrashort laser pulse," *Phys. Rev. Lett.*, vol. 84, p. 447, 2000.

[32] B. Feuerstein, R. Moshammer, D. Fischer, A. Dorn, C. D. Schröter, J. Deipenwisch, J. R. C. Lopez-Urrutia, C. Höhr, P. Neumayer, J. Ullrich, H. Rottke, C. Trump, M. Wittmann, G. Korn, and W. Sandner, "Separation of recollision mechanisms in nonsequential strong field double ionization of Ar: The role of excitation tunneling," *Phys. Rev. Lett.*, vol. 87, p. 043003, 2001.

[33] G. Zhu, M. Schuricke, J. Steinmann, J. Albrecht, J. Ullrich, I. Ben-Itzhak, T. J. M. Zouros, J. Colgan, M. S. Pindzola, and A. Dorn, "Controlling two-electron threshold dynamics in double photoionization of lithium by initial-state preparation," *Phys. Rev. Lett.*, vol. 10, p. 103008, 2009.

[34] J. Blieck, *Couplage entre un piege magneto-optique et un spectrometre d'impulsion d'ion de reculs; application aux collision ion-atomes.* PhD thesis, Laboratoire de physique corpusculaire de Caen, 2009.

[35] J. Steinmann, *Multiphoton Ionization of Laser Cooled Lithium.* PhD thesis, Universität Heidelberg, 2007.

[36] J. W. Turkstra, *Hot recoils from cold atoms.* PhD thesis, Rijksuniversiteit Groningen, 2001.

[37] S. Knoop, *Electron dynamics in Ion-Atom Interactions*. PhD thesis, Rijksuniversiteit Groningen, 2006.

[38] L. H. Coutinho, R. L. Cavasso-Filho, T. C. R. Rocha, M. G. P. Homem, D. S. L. Figueira, P. T. Fonseca, F. C. Cruz, and A. N. de Brito, "Relativistic and interchannel coupling effects in photoionization angular distributions by synchrotron spectrocopy of laser cooled atoms," *Phys. Rev. Lett.*, vol. 93, p. 183001, Oct 2004.

[39] M.-T. Huang, L. Zhang, S. Hasegawa, S. H. Southworth, and L. Young, "Measurements of the electron-impact double-to-single ionization ratio using trapped lithium," *Phys. Rev. A*, vol. 66, p. 012715, Jul 2002.

[40] M.-T. Huang, W. W. Wong, M. Inokuti, S. H. Southworth, and L. Young, "Triple ionization of lithium by electron impact," *Phys. Rev. Lett.*, vol. 90, p. 163201, Apr 2003.

[41] H. Nguyen, X. Flechard, R. Bredy, H. A. Camp, and B. D. DePaola, "Recoil ion momentum spectroscopy using magneto-optically trapped atoms," *Rev. Sci. Inst.*, vol. 75, p. 2683, 2004.

[42] X. Flechard, H. Nguyen, R. Bredy, S. R. Lundeen, M. Stauffer, H. A. Camp, C. Fehrenbach, and B. D. DePaola, "State selective charge transfer cross sections for Na^+ with excited rubidium: A unique diagnostic of the population dynamics of a magneto-optical trap," *Phys. Rev. Lett.*, vol. 91, p. 243005, 2003.

[43] R. Moshammer, D. Fischer, and H. Kollmus, "Recoil-ion momentum spectroscopy and "reaction microscopes" in," *Many-particle quantum dynamics in atomic and molecular fragmentation*, 2003.

[44] K. Lee, J. Kim, H. Noh, and W. Jhe, "Single-beam atom trap in a pyramidal and conical hollow mirror," *Optics letters*, vol. 21, no. 15, pp. 1177–1179, 1996.

[45] Q. Bodart, S. Merlet, N. Malossi, F. Dos Santos, P. Bouyer, and A. Landragin, "A cold atom pyramidal gravimeter with a single laser beam," *Applied Physics Letters*, vol. 96, no. 13, pp. 134101–134101, 2010.

[46] J. Reichel, W. Hänsel, and T. W. Hänsch, "Atomic micromanipulation with magnetic surface traps," *Phys. Rev. Lett.*, vol. 83, pp. 3398–3401, Oct 1999.

[47] C. G. Townsend, N. H. Edwards, K.P.Zetie, C. J. Cooper, J.Rink, and C.J.Foot, "High-density trapping of cesium atoms in a dark magneto-optical trap," *Phys. Rev. A*, vol. 53, p. 1702, 1996.

[48] W. Petrich, M. H. Anderson, J. R. Ensher, and E. A. Cornell, "Behavior of atoms in a compressed magneto-optical trap," *J. Opt. Soc. Am. B*, vol. 11, p. 1332, 1994.

[49] A. M. Steane, M. Chowdhurry, and C. J. Foot, "Radiation force in the magneto-optical trap," *J. Opt. Soc. Am. B*, vol. 9, p. 2142, 1992.

[50] K. Lindquist, M. Stephens, and C. Wieman, "Experimental and theoretical study of the vapor-cell zeeman optical trap," *Phys. Rev. A*, vol. 46, pp. 4082–4090, Oct 1992.

[51] W. Salzmann, *Photoassociation and coherent control of ultracold molecules by femtosecond pulses*. PhD thesis, Universität Freiburg, 2007.

[52] S. Knoop, V. G. Hasan, R. Morgenstern, and R. Hoekstra, "Identification of distinct two-electron transfer processes in O^{6+} + Na collisions," *Eur. Phys. J. D*, vol. 74, p. 992, 2006.

[53] R. E. Olson and A. Salop, "Electron transfer between multicharged ions and neutral species," *Phys. Rev. A*, vol. 14, p. 579, 1976.

[54] N. Stolterfoht, "Dynamic aspect of electron correltation in atomic collisions: The role of dielectronic processes," *Physica Scripta*, vol. T46, p. 22, 1993.

[55] F. Fremont, H. Merabet, J. Y. Chesnel, X. Husson, A. Lepoutre, D. Lecler, G. Rieger, and N. Stolterfoht, "Auger electron emission following double electron capture in 150-keV Ne^{10+}+He collisions," *Phys. Rev. A*, vol. 50, p. 3117, 1994.

[56] M. A. Abdallah, W. Wolff, H. E. Wolf, E. Y. Kamber, M. Stöckli, and C. L. Cocke, "Single and double electron capture from He by Ar^{16+} studied using cold-target recoil-ion momentum spectroscopy," *Phys. Rev. A*, vol. 58, p. 2911, 1998.

[57] R. Dörner, H. Bräuning, J. M. Feagin, V. Mergel, O. Jagutzki, L. Spielberger, T. Vogt, H. Khemliche, M. H. Prior, J. Ullrich, C. L. Cocke, and H. Schmidt-Böcking, "Photo-double-ionization of he: Fully differential and absolute electronic and ionic momentum distributions," *Phys. Rev. A*, vol. 57, pp. 1074–1090, 1998.

[58] X. Flechard, S. Duponchel, L. Adoui, A. Cassimi, P. Roncin, and D. Hennecart, "State-selective double-electron capture in Ne^{10+}+He low-velocity collisions

studied by recoil-ion momentum spectroscopy," *J. Phys. B*, vol. 30, p. 3697, 1997.

[59] F. Frémont, C. Bedouet, X. Husson, and J.-Y. Chesnel, "Scaling laws for single and double electron capture in $A^{q+} + He$ collisions ($q > z_A - 2$) at low impact velocities," *Phys. Rev. A*, vol. 57, pp. 4379–4386, 1998.

[60] X. Flechard, C. Harel, H. Jouin, B. Pons, L. Adoui, F. Fremont, A. Cassimi, and D. Hennecart, "Single- and double-electron capture in low-energy Ne^{10+}-He collisions," *J. Phys. B*, vol. 34, p. 2759, 2001.

[61] N. Bohr and J. Lindhard, "Electron capture and loss by heavy ions penetrating through matter," *Kgl. Danske Videnskab. Selsk. Mat.-fys. Medd.*, vol. 28, 1954.

[62] H. Cederquist, C. Biedermann, N. Selberg, and P. Hvelplund, "Measurements of translational energy gain for one- and two-electron transfer in slow Ar^{q+}-He (q=15–18) collisions," *Phys. Rev. A*, vol. 51, pp. 2169–2178, 1995.

[63] D. H. Crandall, R. E. Olson, E. J. Shipsey, and J. C. Browne, "Single and double charge transfer in C^{4+}-He collisions," *Phys. Rev. Lett.*, vol. 36, pp. 858–860, Apr 1976.

[64] N. Stolterfoht, K. Sommer, J. K. Swenson, C. C. Havener, and F. W. Meyer, "Electron-correlation effects in double-electron-capture collisions of 60 kevc^{6+} with he," *Phys. Rev. A*, vol. 43, p. 5396, 1990.

[65] J.-Y. Chesnel, H. Merabet, X. Husson, F. Frémont, D. Lecler, H. Jouin, C. Harel, and N. Stolterfoht, "Energy dependence of cross sections for double-electron capture in 48–132-keV C^{6+}+He collisions," *Phys. Rev. A*, vol. 53, pp. 2337–2344, Apr 1996.

[66] W. G. Divens and S. M. Jarrett, "Design and performance of a frequency-stabilized ring dye laser," *Rev. Sci. Instr.*, vol. 53, p. 1363, 1982.

[67] A. G. Drentje, H. R. Kremers, J. Mulder, and J. Sijbring, "Ion sources at the KVI (abstract)," *Rev. Sci. Instr.*, vol. 69, p. 728, 1998.

[68] "RoentDek GmbH, http://www.roentdek.com/,."

[69] P. D. Lett, K. Helmerson, W. D. Phillips, L. P. Ratliff, S. L. Rolston, and M. E. Wagshul, "Spectroscopy of Na_2 by photoassociation of laser-cooled Na," *Phys. Rev. Lett.*, vol. 71, pp. 2200–2203, Oct 1993.

[70] S. Bashkin and J. Stoner, *Atomic Energy Levels and Grotrian Diagrams*. North-Holland, Amsterdam, 1975.

[71] H. Winter, M. Mack, R. Hoekstra, A. Niehaus, and F. J. de Heer, "Comment on "evidence for correlated double-electron capture in low-energy collisions of O^{6+} with He"," *Phys. Rev. Lett.*, vol. 58, pp. 957–957, Mar 1987.

[72] J.-Y. Chesnel, B. Sulik, H. Merabet, C. Bedouet, F. Frémont, X. Husson, M. Grether, A. Spieler, and N. Stolterfoht, "Enhancement of dielectronic processes in Ne^{10+}+He collisions at low kev energies," *Phys. Rev. A*, vol. 57, pp. 3546–3553, May 1998.

[73] K. Dieckmann, R. J. C. Spreeuw, M. Weidemüller, and J. T. M. Walraven, "Two-dimensional magneto-optical trap as a source of slow atoms," *Phys. Rev. A*, vol. 58, p. 3891, 1998.

[74] J. Schoser, A. Batär, R. Löw, V. Schweikhard, A. Grabowski, Y. B. Ovchinnikov, and T. Pfau, "Intense source of cold Rb atoms from a pure two-dimensional magneto-optical trap," *Phys. Rev. A*, vol. 66, p. 023410, 2002.

[75] F. Lison, P. Schuh, D. Haubrich, and D. Meschede, "High-brilliance zeeman-slowed cesium atomic beam," *Phys. Rev. A*, vol. 61, p. 013405, Dec 1999.

[76] I. Courtillot, A. Quessada, R. Kovacich, J. Zondy, A. Landragin, A. Clairon, and P. Lemonde, "Efficient cooling and trapping of strontium atoms," *Optics letters*, vol. 28, no. 6, pp. 468–470, 2003.

[77] T. B. Swanson, D. Asgeirsson, J. A. Behr, A. Gorelov, and D. Melconian, "Efficient transfer in a double magneto-optical trap system," *J. Opt. Soc. Am. B*, vol. 15, pp. 2641–2645, Nov 1998.

[78] W. Wohlleben, F. Chevy, K. Madison, and J. Dalibard, "An atom faucet," *The European Physical Journal D - Atomic, Molecular, Optical and Plasma Physics*, vol. 15, pp. 237–244, 2001.

[79] Z. T. Lu, K. L. Corwin, M. J. Renn, M. H. Anderson, E. A. Cornell, and C. E. Wieman, "Low-velocity intense source of atoms from a magneto-optical trap," *Phys. Rev. Lett.*, vol. 77, pp. 3331–3334, Oct 1996.

[80] J. Ullrich, R. Moshammer, R. Dörner, O. Jagutzki, V. Mergel, H. Schmidt-Böcking, and L. Spielberger, "Recoil-ion momentum spectroscopy," *J. Phys. B*, vol. 30, p. 2917, 1997.

[81] "Schäfter und Kirchhoff, http://www.sukhamburg.com/."

[82] L. Ricci, M. Weidemüller, T. Esslinger, A. Hemmerich, C. Zimmermann, V. Vuletic, W. König, and T. W. Hänsch, "A compact grating-stabilized diode laser system for atomic physics," *Opt. Comm.*, vol. 117, pp. 541–549, 1995.

[83] G. C. Bjorklund, M. D. Levenson, W. Lenth, and C. Ortiz, "Frequency modulation (fm) spectroscopy," *Applied Physics B*, vol. 32, p. 145, 1983.

[84] E. A. Donley, T. P. Heavner, F. Levi, M. O. Tataw, and S. R. Jefferts, "Double-pass acousto-optic modulator system," *Rev. Sci. Inst.*, vol. 76, p. 063112, 2005.

[85] "Moglabs, http://www.moglabs.com//."

[86] B. Höltkemeier, "2D MOT as a source of a cold atom target," *Diploma Thesis, Universität Heidelberg*, 2011.

[87] T. G. Tiecke, S. D. Gensemer, A. Ludewig, and J. T. M. Walraven, "High-flux two-dimensional magneto-optical-trap source for cold lithium atoms," *Phys. Rev. A*, vol. 80, p. 013409, 2009.

[88] J. R. L. Maleki, "Multistage two-dimensional magneto-optical trap as a compact cold atom source," *Opt. Lett.*, vol. 31, p. 682, 2006.

[89] S. Chaudhuri, S. Roy, and C. S. Unnikrishnan, "Realization of an intense cold Rb atomic beam based on a two-dimensional magneto-optical trap: Experiments and comparison with simulations," *Phys. Rev. A*, vol. 74, p. 023406, 2006.

[90] G. Zürn, "Realization of an Optical Microtrap for a highly degenerate Fermi gas," *Diploma Thesis, Universität Heidelberg*, 2009.

[91] D. Gerbert, "Absorptionsabbildung ultrakalter Atome in einem Target für Schwerionenstrahlen," *Bachelor Thesis, Universität Heidelberg*, 2011.

[92] H. Metcalf and P. Straten, "Laser cooling and trapping of neutral atoms,"

[93] C. Glück, "Quenching of light-assisted collisions in an optical two-species atom trap," *Diploma Thesis, Universität Freiburg*, 2008.

[94] W. C. WILEY and . H. McLAREN, "Time-of-flight mass spectrometer with improved resolution," *Rev. Sci. Inst.*, vol. 26, p. 1150, 1955.

[95] "SIMION Version 8.0, http://simion.com/."

[96] A. I. Chichinin, K.-H. Gericke, S. Kauczok, and C. Maul, "Imaging chemical reactions - 3d velocity map imaging," *Int. rev. in physical chemistry*, vol. 28, p. 607, 2009.

[97] H. B. Bebb and A. Gold, "Multiphoton ionization of hydrogen and rare-gas atoms," *Phys. Rev.*, vol. 143, pp. 1–24, Mar 1966.

[98] H. Friedrich, *Theoretical Atomic Physics*. Berlin: Springer, 1990.

[99] H. B. Bebb, "Quantitative theory of the two-photon ionization of the alkali atoms," *Phys. Rev.*, vol. 149, pp. 25–32, Sep 1966.

[100] P. Agostini, F. Fabre, G. Mainfray, G. Petite, and N. K. Rahman, "Free-free transitions following six-photon ionization of xenon atoms," *Phys. Rev. Lett.*, vol. 42, pp. 1127–1130, Apr 1979.

[101] P. B. Corkum, N. H. Burnett, and F. Brunel, "Above-threshold ionization in the long-wavelength limit," *Phys. Rev. Lett.*, vol. 62, pp. 1259–1262, Mar 1989.

[102] M. Protopapas, C. H. Keitel, and P. L. Knight, "Atomic physics with super-high intensity lasers," *Reports on Progress in Physics*, vol. 60, no. 4, p. 389, 1997.

[103] G. G. Paulus, W. Nicklich, H. Xu, P. Lambropoulos, and H. Walther, "Plateau in above threshold ionization spectra," *Phys. Rev. Lett.*, vol. 72, pp. 2851–2854, May 1994.

[104] G. Wentzel, "Über die Richtungsverteilung der Photoelektronen," *Z. Physik*, vol. 41, p. 828, 1927.

[105] G. Leuchs and H. Walther, *Angular distribution of photoelectrons and light polarization effects in multiphoton ionization of atoms. In S.L. Chin and P. Lambropulos.* Academic Press, 1984.

[106] "NIST database,http://physics.nist.gov."

[107] T. Takekoshi, G. M. Brooke, B. M. Patterson, and R. J. Knize, "Absolute Rb one-color two-photon ionization cross-section measurement near a quantum interference," *Phys. Rev. A*, vol. 69, p. 053411, May 2004.

[108] Z.-M. Wang and D. S. Elliott, "Complete measurements of two-photon ionization of atomic rubidium using elliptically polarized light," *Phys. Rev. A*, vol. 62, p. 053404, Oct 2000.

[109] Z.-M. Wang and D. S. Elliott, "Determination of cross sections and continuum phases of rubidium through complete measurements of atomic multiphoton ionization," *Phys. Rev. Lett.*, vol. 84, pp. 3795–3798, Apr 2000.

[110] T. Dinneen, C. Wallace, K. Tan, and P. Gould, "Use of trapped atoms to measure absolute photoionization cross sections," *Optics letters*, vol. 17, no. 23, pp. 1706–1708, 1992.

[111] "Ion-recoil energy measurement in photoionization of laser-cooled rubidium," *Phys. Rev. A*, vol. 56, p. R4385, 1997.

[112] S. Wolf and H. Helm, "Ion-recoil momentum spectroscopy in a laser-cooled atomic sample," *Phys. Rev. A*, vol. 62, p. 043408, 2000.

[113] W. Ketterle, D. Durfee, and D. Stamper-Kurn, "Making, probing and understanding bose-einstein condensates," *Arxiv preprint cond-mat/9904034*, vol. 5, 1999.

[114] C. G. Townsend, N. H. Edwards, C. J. Cooper, K. P. Zetie, C. J. Foot, A. M. Steane, P. Szriftgiser, H. Perrin, and J. Dalibard, "Phase-space density in the magneto-optical trap," *Phys. Rev. A*, vol. 52, pp. 1423–1440, 1995.

[115] R. Grimm, M. Weidemüller, and Y. B. Ovchinnikov, "Optical dipole traps for neutral atoms," *arXiv:physics/9902072*, 1999.

[116] M. Anderson, J. Ensher, M. Matthews, C. Wieman, and E. Cornell, "Observation of bose-einstein condensation in a dilute atomic vapor," *science*, vol. 269, no. 5221, p. 198, 1995.

[117] K. Davis, M. Mewes, M. Andrews, N. Van Druten, D. Durfee, D. Kurn, and W. Ketterle, "Bose-einstein condensation in a gas of sodium atoms," *Physical Review Letters*, vol. 75, no. 22, pp. 3969–3973, 1995.

[118] S. Geyer, A. Sokolov, A. Thorn, G. Vorobyev, T. Stöhlker, and O. Kester, "Characterization of the SPARC-EBIT at GSI," *Journal of Instrumentation*, vol. 5, no. 10, p. C10003, 2010.

[119] A. Sokolov, *Charge breeding investigation in EBIS/T and collision study of ions with cold atoms for HITRAP*. PhD thesis, Universität Heidelberg, 2010.

[120] C. Klempt, T. van Zoest, T. Henninger, O. Topic, E. Rasel, W. Ertmer, and J. Arlt, "Ultraviolet light-induced atom desorption for large rubidium and potassium magneto-optical traps," *Phys. Rev. A*, vol. 73, p. 013410, 2006.

[121] M. Cetina, A. Grier, J. Campbell, I. Chuang, and V. Vuletić, "Bright source of cold ions for surface-electrode traps," *Phys. Rev. A*, vol. 76, p. 041401, 2007.

[122] C. Gabbanini, S. Gozzini, and A. Lucchesini, "Photoionization cross section measurement in a Rb vapor cell trap," *Opt. Comm.*, vol. 141, p. 25, 1997.

Acknowledgements

Mein besonderer Dank gilt meinem Betreuer Prof. Dr. **Matthias Weidemüller**, der mir neben der Arbeit in diesem spannenden Themengebiet viele Türen öffnete, um Einblicke in die internationale Forschungswelt zu bekommen. Matthias, ich möchte Dir für das Vertrauen während meiner Arbeit und die große Unterstützung danken!

A huge thanks to Prof. Dr. **Brett DePaola** for the great support during my whole thesis! Thanks for all your help in designing and assembling the spectrometer and detector and all the support, not only during your visits in Freiburg and Heidelberg, but also during all the skype calls!

Für die tolle Zusammenarbeit möchte ich mich bei **Bastian Höltkemeier** bedanken. Basti, tausend Dank für die gemeinsame Zeit im Labor und natürlich auch im Büro. Sowohl beim Suchen nach den kalten Atomen während Deiner Diplomarbeit als auch bei der Suche nach Wackelkontakten im Vakuum hat Deine Gelassenheit immer sehr zur Ruhe beigetragen. Das Arbeiten mit Dir hat besonders viel Spass gemacht. Weiterhin viel Erfolg mit dem MOTRIMS Experiment!

Ein weiteres großes Dankeschön an **Dominic Litsch**. Es hat riesig Spaß gemacht, Dir sowohl unsere Arbeit näher zu bringen als auch mit Dir im Labor zusammenzuarbeiten! Insbesondere Deine Liebe zum Detail hat sicherlich das MOTRIMS Experiment stabiler gemacht! Für die Zukunft wünsche ich Dir noch viel Spaß beim justieren!

Vielen Dank an **Thomas Amthor** für die unermüdliche Unterstützung und große Hilfe während Deiner Zeit bei den Rydbergs und natürlich während Deiner Zeit am MOTRIMS Experiment.

Ein großes Dankeschön an das gesamte MOTRIMS Team, welches mich noch zu Freiburg-Zeiten unterstützt hat: **Wenzel Salzmann, Terry Mullins, Magnus Albert** und **Ina Blank** und an **David Gerbert** für seine Unterstützung hier in Heidelberg.

Die Arbeiten zu den Ladungstransferexperimenten wären ohne die Unterstützung

von **Ina Blank** und Prof. Dr. **Ronnie Hoekstra** nicht möglich gewesen! Neben den Experimenten konnte ich bei Euch die Erfahrung von tollen kulinarischen Erlebnissen machen, insbesondere die frittierten Nudeln werde ich nicht vergessen. Ina, Dir natürlich auch vielen Dank für die Hilfe am Heidelberg/Freiburg Experiment während Deiner Diplomarbeit. Für den Abschluss Deiner Arbeit wünsche ich Dir noch viel Erfolg.

Bei der gesamten QD-Gruppe möchte ich mich bedanken für die gute Arbeitsatmosphäre und Anregungen zum Experiment. Insbesondere **Marc Repp**, vielen Dank für Deine Beratertätigkeiten und Deine Hilfe zu jeder Tageszeit im Labor. An Dich, **Chrisptoph Hofmann**, für die super Zusammenarbeit bei der 2D MOT und Deine Ideen und Begeisterungsfähigkeit im Labor. An **Nele Müller** für die vielen Kaffees und Diskussionen um SimION zu verstehen. Ein großes Dankeschön an **Eva Kuhnle** für die Unterstützung in den letzten beiden Monaten. Vielen Dank insbesondere an **Juris Ullmanis** und **Hanna Schempp** für die unersetzliche Hilfe bei der Experimentiersteuerung und natürlich dem Rest der Gruppe: **Shannon Whitlock, Georg Günther, Martin Robert de Saint Vincent, Robert Heck** und **Henning Labuhn**. Ebenfalls vielen Dank an die ehemaligen Freiburger Mitarbeiter: **Roland Wester, Sebastian Trippel, Rico Otto, Jochen Mikosch, Katja Reiser, Ruth Billen, Sebastian Kaiser, Markus Reetz-Lamour, Janne Denskat, Wendelin Sprenger, Christian Glück, Christian Giese, Christian Eichhorn, Anna Grochola, Katrin Mörtelbauer, Petr Hlavenka** und **Johannes Deiglmayer**, sowie den ehemalingen Heidelbergern, die von Anfang an unsere Gruppe unterstützt haben: **Kristina Meyer, Hannes Busche, Aline Faber, Romain Müller, Stefan Schmidt, Stefan Arnold, Thomas Kirchner, Niko Schnellbächer** und besonders bei **Silvania Alves de Carvalho**.

Ein weiterer besonderer Dank geht an **Daniel Fischer**, für die vielen Diskussionen und Anregungen für mein Experiment sowie Prof. Dr. **Selim Jochim** und seiner gesamten Gruppe, von denen einige Ideen in diese Arbeit eingeflossen sind.

Ein sehr großes Dankeschön an die Mitarbeiter der mechanischen und elektrischen Werkstätten und die Konstruktion des Physikalschen Insituts, ohne die das Experiment nicht stehen würde. Stellvertrendend bedanke ich mich den Leitern, **Herrn Windelband**, **Herrn Ziegler** und **Herrn von Walther**. Ohne die große Hilfe der mechanischen Werkstatt bei dem Umzug wäre das Experiment erst gar nicht nach Heidelberg gekommen! Insbesondere Herrn **Jürgen Gerhäuser** und **Kevin Stumpf** für die große Hilfe bei der Konstruktion des neuen Spektrometers und der 2D MOT! Und natürlich der mechanischen Werkstatt für die Umsetzung, insbesondere Herrn **Giesser** für das geduldige Wickeln der Spulen, **Jessica Riedinger** für

das Bohren vieler, vieler kleiner Löcher und **Max von Klot** für die rechtzeitige Fertigstellung der Spektrometerteile. Bei der elektronischen Werkstatt möchte ich mich für die Experimentiersteuerung und für die schnelle Hilfe bei Defekten oder fehlenden Komponenten bedanken.

Die große Unterstützung meiner Familie während der gesamten Zeit meiner Arbeit ist unglaublich! Vielen Dank an meine Eltern! Ebenfalls vielen Dank an **Parisa** und **Tobias** für die große Hilfe und entspannenden Zeiten, wenn hier das Chaos ausbrach! Last but not least I want to thank **Sherif** for the great, great support.